



Chair of Applied Geophysics

Doctoral Thesis



Seismic Investigation of the Prospective
Drilling Site for the DIVE Phase 2 Project

Damian Pasiecznik

June 2024



MONTANUNIVERSITÄT LEOBEN
www.unileoben.ac.at

AFFIDAVIT

I declare on oath that I wrote this thesis independently, did not use any sources and aids other than those specified, have fully and truthfully reported the use of generative methods and models of artificial intelligence, and did not otherwise use any other unauthorized aids.

I declare that I have read, understood and complied with the "Good Scientific Practice" of the Montanuniversität Leoben.

Furthermore, I declare that the electronic and printed versions of the submitted thesis are identical in form and content.

Date 03.06.2024

Signature Author
Damian Pasiecznik

Abstract

The Ivrea Verbano Zone (IVZ) in Italy presents one of the most complete crust-upper mantle geological references globally, featuring lower-crustal rocks and upper mantle fragments exposed adjacent to the Insubric Line. The Drilling the Ivrea-Verbano Zone (DIVE) project aims to deepen the understanding of this complex region by drilling a 4 km deep borehole intended to reach and study the top of the Ivrea Geophysical Body (IGB), which is considered a shallow expression of the crust-mantle transition. This thesis focuses on the geophysical characterization of the prospective drill site, located at the top of an outcropping ultramafic body known as the Balmuccia Peridotite.

A high-resolution seismic survey was conducted across the Balmuccia Peridotite to delineate its structure and relationship with surrounding geological formations. The survey employed a fixed spread of 200 vertical geophones and 160 3C-sensors, spaced approximately 10-11 meters along three sub-parallel lines. Vibroseis source points were positioned at 22-meter intervals along a 2.2 km line, using a 12-140 Hz 10-second linear sweep with a 3-second listening time.

The P-wave traveltimes tomography reveals that the seismic velocities within the peridotite vary between 6 and 8 km/s, with an average velocity of 7 km/s. These differences highlight the heterogeneous nature of the peridotite, which is affected by the presence of fractures and faults. Notably, the higher velocities observed are consistent with laboratory results obtained from small-scale samples of the region. Reflection seismic analysis identified subvertical reflectors that coincide with the peridotite boundaries converging at a depth of around 0.175 km b.s.l. (ca. 875 m from the surface), suggesting a lens-like structure for the peridotite body.

Although the survey's limited aperture impeded detailed imaging below the lens-shaped body, a prominent reflector at approximately 1.3 km depth b.s.l. potentially marks the top of the IGB, consistent with previous geophysical estimates. These findings provide critical insights into the seismic characteristics of the IVZ, laying the groundwork for future in situ geophysical measurements and advancing our understanding on the crust-mantle transition.

Zusammenfassung

Die Ivrea-Verbano-Zone (IVZ) in Italien stellt eines der vollständigsten geologischen Referenzen der Erdkruste und des oberen Mantels weltweit dar, mit Gesteinen der unteren Kruste und Fragmenten des oberen Mantels, die neben der Insubrischen Linie freigelegt sind. Das Projekt „Drilling the Ivrea-Verbano Zone“ (DIVE) zielt darauf ab, das Verständnis dieser komplexen Region durch das Bohren eines 4 km tiefen Bohrlochs zu vertiefen, um die Spitze des Ivrea-Geophysikalischen Körpers (IGB) zu erreichen und zu untersuchen, der als flache Ausdrucksform des Krusten-Mantel-Übergangs gilt. Diese Dissertation konzentriert sich auf die geophysikalische Charakterisierung des geplanten Bohrstandorts, der sich an der Spitze eines ausstreichenden ultramafischen Körpers, bekannt als Balmuccia-Peridotit, befindet.

Eine hochauflösende seismische Erkundung wurde über den Balmuccia-Peridotit durchgeführt, um seine Struktur und Beziehung zu den umgebenden geologischen Formationen zu bestimmen. Die Untersuchung verwendete eine feste Verteilung von 200 vertikalen Geophonen und 160 3C-Sensoren, die im Abstand von etwa 10-11 Meter entlang drei paralleler Linien beabstandet waren. Vibroseis-Quellpunkte wurden in 22-Meter-Abständen entlang einer 2,2 km langen Linie positioniert, wobei ein 12-140 Hz 10-Sekunden-Linear-Sweep mit einer 3-Sekunden-Abhörzeit verwendet wurde.

Die P-Wellen-Laufzeit-Tomographie zeigt, dass die seismischen Geschwindigkeiten innerhalb des Peridotits zwischen 6 und 8 km/s variieren, mit einer durchschnittlichen Geschwindigkeit von 7 km/s. Diese Unterschiede unterstreichen die heterogene Natur des Peridotits, der durch das Vorhandensein von Brüchen und Verwerfungen beeinflusst wird. Bemerkenswerterweise stimmen die beobachteten höheren Geschwindigkeiten mit den Labormessergebnissen von kleineren Proben aus der Region überein. Die Reflexionsseismikanalyse identifizierte subvertikale Reflektoren, die mit den an der Oberfläche kartierten Peridotit-Grenzen übereinstimmen und in einer Tiefe von etwa 0,175 km unter dem Meeresspiegel (ca. 875 m von der Oberfläche) konvergieren, was auf eine linsenartige Struktur des Peridotitkörpers hindeutet.

Obwohl die begrenzte Apertur der Untersuchung eine detaillierte Abbildung unterhalb des linsenförmigen Körpers verhinderte, könnte ein markanter Reflektor in etwa 1,3 km Tiefe unter dem Meeresspiegel die Spitze des IGB markieren, was mit früheren geophysikalischen Schätzungen übereinstimmt. Diese Erkenntnisse liefern entscheidende Einblicke in die seismischen Eigenschaften der IVZ und des darunter liegenden IGB, legen den Grundstein für

zukünftige geophysikalische In-situ-Messungen und erweitern unser Verständnis des Krusten-Mantel-Übergangs.

Contents

1.	Introduction	1
1.1.	The Ivrea Verbano Zone	1
1.2.	The Ivrea Geophysical Body: Geophysical studies.....	3
1.3.	Project DIVE	9
1.4.	Motivation	11
2.	Survey design	13
3.	Data acquisition and quality control.....	18
4.	Data pre-conditioning.....	20
4.1.	Vertical stacking and sweep correlation	20
4.2.	Instrument simulation.....	22
4.3.	Geometry definition	25
4.4.	Horizontal components	29
5.	First arrival travelttime tomography.....	32
5.1.	Two-dimensional inversion	35
5.2.	Velocity constraints	37
5.3.	Three-dimensional inversion.....	38
6.	Reflection seismic processing and imaging	41
6.1.	Seismic Processing	43
6.2.	Seismic imaging	55
7.	Interpretation	68
7.1.	Travelttime tomography	68
7.2.	Reflection seismics.....	69
8.	Discussion	71
9.	Conclusions	74
	Acknowledgements.....	75

References	76
List of figures	82

1. Introduction

The Alpine region has been an object of study for geophysicists and geologists throughout several decades. Most of the efforts have been focused on understanding the complicated crustal structure that characterizes the area. Among the interesting highlights that the Alps provide to study, the Ivrea Verbano Zone (IVZ) and its outcropping rocks appear as one of the most intricate geological features. What is more, the geophysical body that lays below the IVZ (the Ivrea Geophysical Body) is of most importance, since its understanding will allow a better comprehension of the history and dynamics of the Alpine orogen. This chapter brings a brief geological description of the IVZ (Section 1.1), followed by a historical overview of the geophysical studies performed across the region (Section 1.2). An introduction to the DIVE (Drilling the Ivrea-Verbano zonE) project will be made in Subsection 1.3 followed by the motivation of this thesis in Section 1.4.

1.1. The Ivrea Verbano Zone

The IVZ is a geological region located in northwest Italy (Figure 1), delimited on its northwestern side by the Insubric Line (IL) (Schmid et al., 1987). Towards the Southeast, it is separated from the adjacent Strona-Ceneri Zone and Post-Variscan rocks by the Cossato-Mergozzo-Brissago Line (CMBL) and the Pogallo Line (PL) (Boriani & Sacchi, 1973; Zingg, 1983; Handy, 1987). The IVZ has been interpreted as an exposed continental crust-mantle transition (Voshage et al., 1990; Quick et al., 1992; Rutter et al., 1993), providing a rare glimpse into the lithologies of the lower continental crust of the Southern Alpine basement (Zingg et al., 1990). Its emplacement into the upper crust comes after uplifting throughout Mesozoic crustal thinning and posterior lithospheric wedging linked to Alpine collision (Schmid et al., 1987; Nicolas et al., 1990).

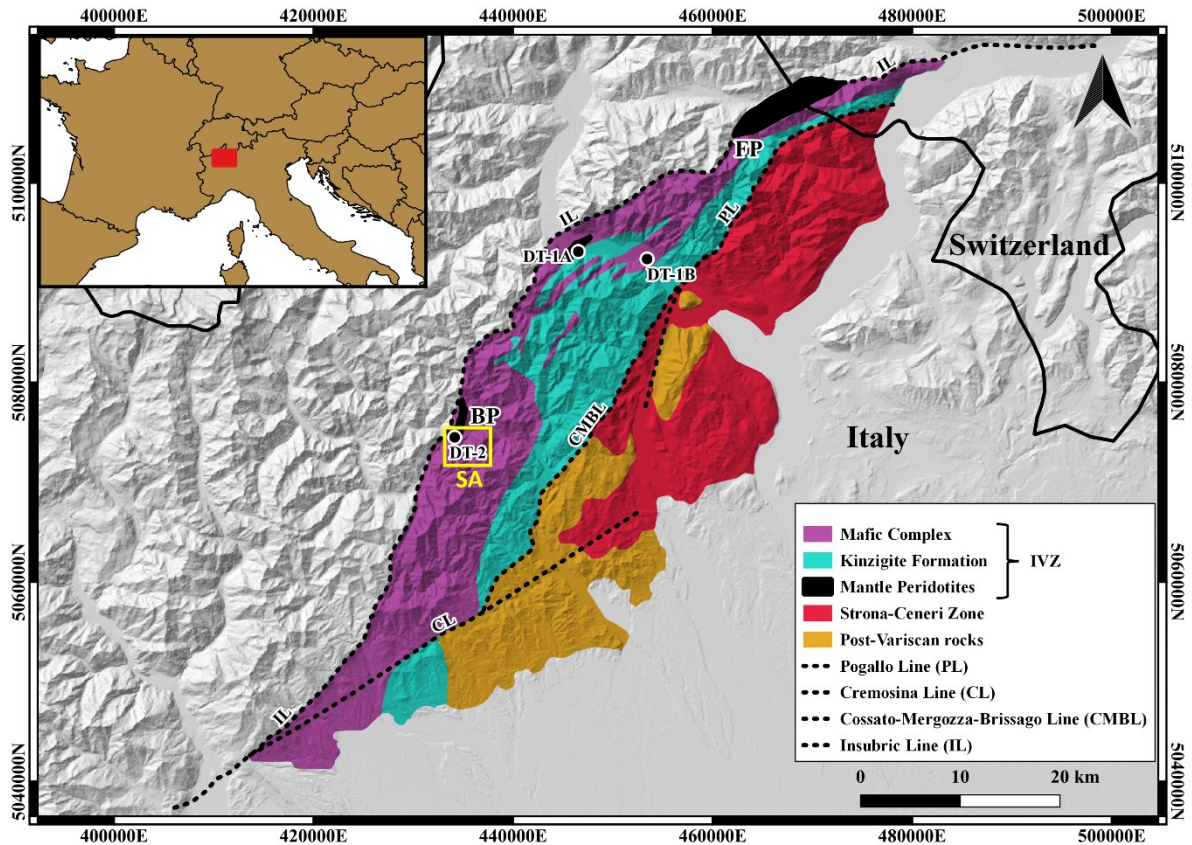


Figure 1: Geologic map of the southern Alps color-coded with the main formations that constitute the IVZ and its surroundings (see legend on map). Main faults are depicted as dashed lines. Proposed drill sites by project DIVE are marked with black circles with their respective names. The study area (SA) is marked with a yellow square. Balmuccia Peridotite (BP). Finero Peridotite (FP). Modified from Zingg (1983).

It contains plutonic and high-pressure, high-temperature metamorphic rocks (Fountain, 1976), which can be classified into two main units: the Kinzigite Formation and the Mafic Complex. Laboratory studies carried out on rock samples collected across the area have shown that it is characterized by high density and high seismic velocities (e.g. Burke & Fountain, 1990; Khazanehdari et al., 2000; Vilhelm et al., 2008) and, therefore, can be considered as a hardrock environment. Detailed information on the emplacement of the IVZ, its structure and lithology can be found in Schmid et al. (1987) and Zingg et al. (1990). A series of peridotite bodies can be found within the IVZ, the largest among them being the Finero, Balmuccia, and Baldissero Peridotites (Lensch, 1969; Rivalenti, 1975; Ernst, 1978; Shervais, 1978, 1979; Rivalenti et al., 1981). The Balmuccia Peridotite (BP), the focus of this study, is located East of the Insubric Line, surrounded by the Mafic Complex. It forms a ca. 4.4 km long, maximum 0.8 km wide

body outcropping over 1000 m elevation change (Figure 1). Its emplacement inside the IVZ has been in discussion for several years, with various end-member models proposed: A peridotite diapir that intruded the pre-existing lower crust (Shervais, 1979; Boudier et al., 1984), the mantle basement over which the Mafic Complex crystalized (Rivalenti et al., 1981; Quick et al., 1992) or a peridotite body incorporated into the Kinzigite Formation as a lensoidal body before the intrusion of the Mafic Complex (Quick et al., 1995). These models lack a foundation in geophysical studies. In fact, no geophysical studies have been conducted across the BP that could validate any of the proposed models, highlighting our limited understanding of this body's subsurface structure. What is more, due to the locally very steep and often inaccessible slopes of the terrain, the entire BP outcrop cannot be studied geologically in detail, resulting in somewhat different geological maps.

1.2. The Ivrea Geophysical Body: Geophysical studies

The Ivrea Geophysical Body (IGB) within the IVZ emerges as a key feature for understanding the continental crust and mantle dynamics. It is considered as a sliver of Adriatic lower lithosphere (e.g. Schmid et al., 2017) that has been emplaced at anomalously shallow depths during the Alpine collision. The IGB stands out due to its anomalous high-density and high-velocity characteristics, which have been the focus of extensive research efforts spanning several decades.

The mission to understand the IGB initiated with the pioneering efforts of geologists and geophysicists in the mid-20th century. These initial incursions into the IGB's investigation were characterized by the application of emerging geophysical techniques, setting the stage for decades of rigorous research. The earliest attempts to delineate the IGB were supported heavily on gravity mapping. This method was important for identifying the anomalous density contrasts that the IGB presented against the surrounding crustal material. The first contribution that correlates the IGB gravity anomaly and the lower-crust rocks of the IVZ is the work of Niggli (1946). He attempted to quantitatively assess whether the outcropping rocks could account for the observed anomaly. However, he concluded that the theoretical gravity anomaly produced by these rocks did not fully explain the quantitative aspects of the observed anomaly and that a higher density material must be present at shallow depths. The studies by Niggli (1946) and Vecchia (1968) laid the groundwork by outlining the gravity anomaly associated with the IGB, suggesting a high-density subterranean body.

The seismic refraction experiments of the late 1960s provided the first image of the IGB (Berckhemer, 1968). Berckhemer combined the interpretation of gravimetric and seismic data, proposing a 2D model where the IGB is a continuous body with a sharp and constant density contrast representing the Crust-Mantle transition (the “Moho”). His model puts the top of the body at a depth of ca. 3km. Its shape is what started the reference towards the IGB as the “Bird’s head” in the literature (Figure 3). Although very simple, Berckhemer’s model was what inspired the following decades of geophysical investigations. Further active seismic experiments were carried out in the framework of the projects ALP 75 and SUDALP 77 (Miller, 1976; Ansorge et al., 1979), which were focused on collecting seismic refraction data. The results showed high P-wave seismic velocities in the IVZ at relative shallow depths (ca. 7 km/s at 5 km depth). Also, the seismic data did not support the thin extension of the IGB across the Insubric Line as proposed by Berckhemer and, in addition, the results showed that there is a remarkable difference between the crustal structure below the IVZ and the regions NW and SE from it.

Kissling (1984) presented the first 3D gravity model for the northern part of the IGB, considering gravity data acquired along three profiles perpendicular to the IVZ local strike. Their main goal was to obtain the simplest 3D model that would fit the observed data, reason why the model is just a homogeneous 3D eastward dipping plate with a density contrast of 350 km/m^3 .

The arrival of active seismic experiments focused on acquiring seismic reflection data improved the understanding of the Alpine subsurface. In the late 1980s, several programs were developed to image the deep structure of the Alps through geophysical surveys. Three of these programs crossed the IVZ: Etude Continentale et Océanique par Réflexion et Réfraction Sismique (ECORS) – CROsta Profonda (CROP), European GeoTraverse (EGT) and Nationales Forschungsprogramm 20 (NFP-20). Initiated in 1982, the EGT project was directed at enhancing the comprehension of the continental lithosphere's structure, state, and composition (Galson & Mueller, 1986). The results from the southern segment that crossed the IVZ (EGT-S) imaged a crust-mantle like interface at a depth of 35 km. This interface was interpreted as the lower limit of the IGB (Galson & Mueller, 1987). In 1985 the ECORS-CROP experiment was carried out. It was an extensive geophysical study that integrated vertical and wide-angle seismic-reflection, gravity, and magnetic studies along a 190 km profile across the Western Alps. Unfortunately, the reflection imaging did not show any evident shallow reflector that could be associated to the top of the IGB (Figure 2). However, the experiment allowed for significant studies that combined gravity and reflection seismic data to produce various 2D

models for the structure of the Alps (e.g. Bayer et al., 1989; Nicolas et al., 1990; Thouvenot et al., 1990). In parallel to the ECORS-CROP experiment and with the same objective, the Swiss National Science Foundation initiated the program NFP 20 (e.g. Pfiffner et al., 1990; Valasek et al., 1991). Kissling (1993) discussed the results of these programs in detail and pointed out that, although they mapped the Moho topography through several parts of the Alps, they were not successful in bringing conclusive results on the structure and physical characteristics of the IGB.

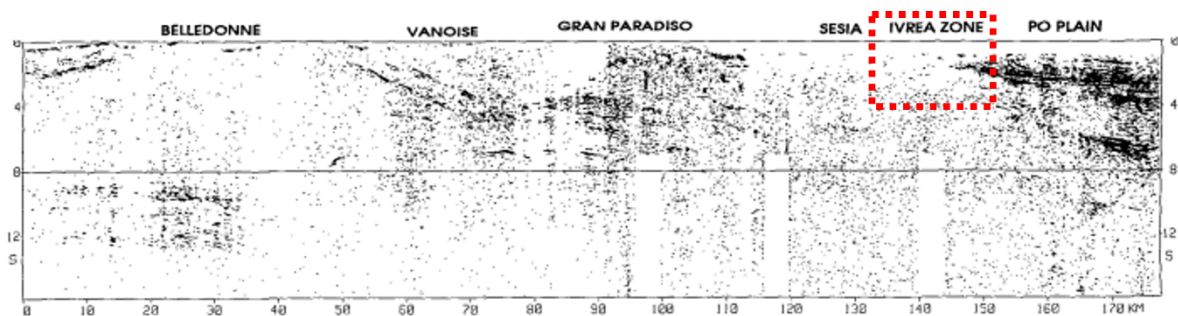


Figure 2: Seismic image from the ECORS-CROP study. The red-dashed square highlights how transparent the seismic image is for the first 4 km in the Ivrea Zone. Modified from Nicolas et al. (1990).

There has been an increase in seismic data in the Alps through various seismic arrays (e.g. Hetényi et al., 2018) which allowed the implementation of modern seismic tomographic techniques utilizing local and teleseismic earthquake events. These studies have proven highly valuable in the understanding of the structure of the Alps, demonstrating the existence of the IGB as a shallow high-velocity body (e.g. Kissling et al., 2006; Diehl et al., 2009). However, their resolution does not provide meaningful details about the local relationship between the shallow parts of the IGB and the rocks exposed at the IVZ. The same difficulty can be seen for the ambient noise tomography techniques, where the results only give a good regional understanding of the IGB's structure (e.g. Lu et al., 2018).

It should be noted that most of the studies presented up to this point were part of programs or works focused on imaging the geological structure of the alps within a regional approach. These studies were based on surveys that did not adjust the parameters or geometries to target the IGB. Therefore, more targeted studies needed to be performed to fill the gaps. Recent

investigations focused entirely on the IVZ have shown promising results towards the understanding of the IGB's structure. Scarponi et al. (2020) focused on explaining the structure of the IGB using novel gravity data and three-dimensional density modeling. They integrated these data with geological observations and analyzed rock properties to refine the understanding of the IGB's composition and structure. The model that they suggested for the IGB is a dense body close to the surface (0–2 km depth b.s.l.) characterized by ultramafic or mantle peridotite-type rocks (Figure 4). These results were later refined by Scarponi et al. (2021), where they combined seismic and gravity data through a joint inversion method. The methodology included seismic receiver functions and comprehensive gravity data analysis, providing better constraints on the shape and the physical properties of the IGB. They concluded that the model geometry that better aligns with the outcrops of the IVZ is a structure with a local peak at 1-3 km depth b.s.l. Finally, a study by Scarponi et al. (2023) analyzed the IGB's shear wave velocity structure using seismic ambient noise tomography (ANT). Analyzing seismic data from both permanent and temporary networks, they created a detailed 3-D shear wave velocity model (Figure 5). Their findings reveal a complex subsurface structure, with high-velocity anomalies corresponding to the IGB.

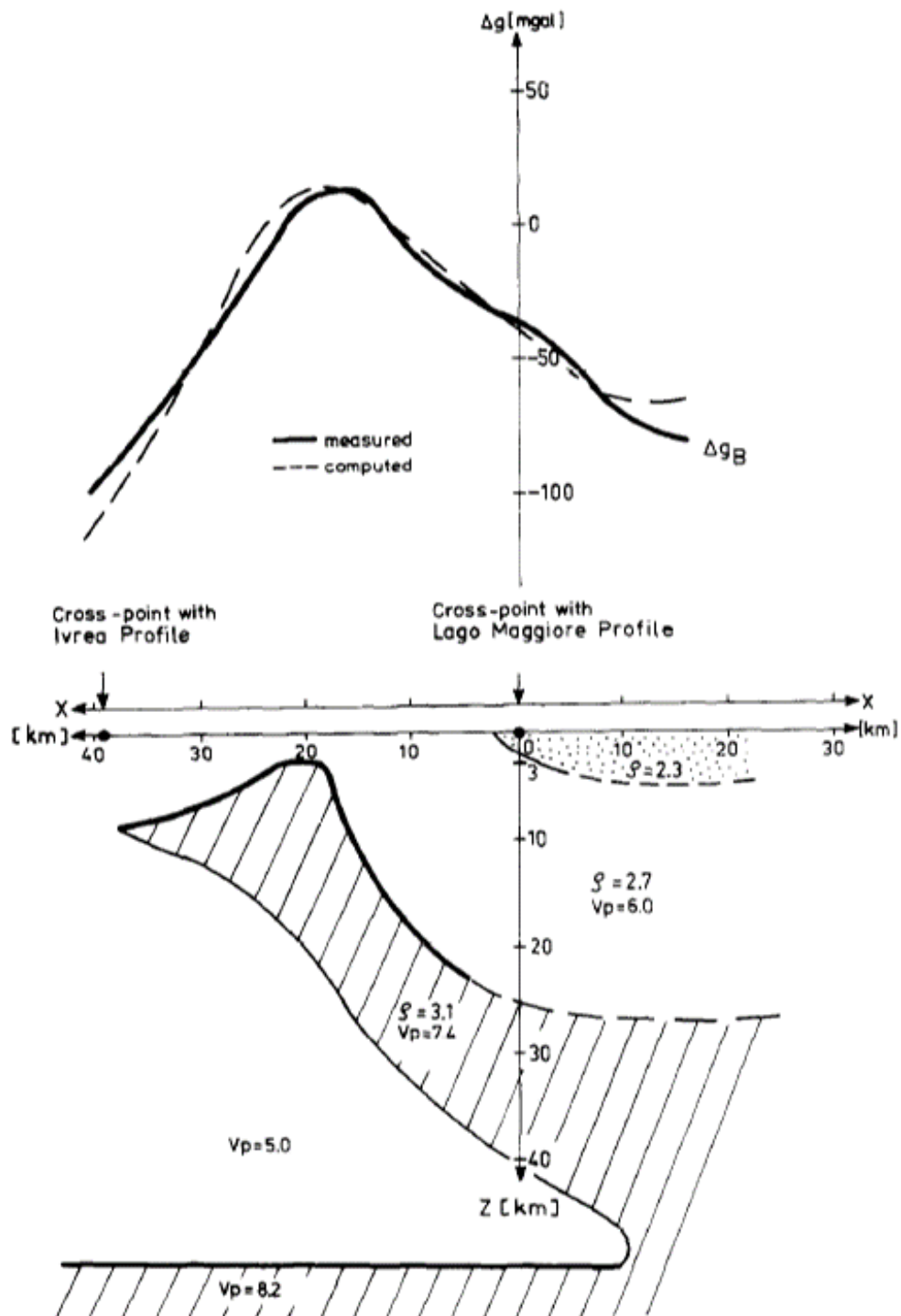


Figure 3: Proposed geophysical model of the IGB by Berckhemer (1968). The top figure shows the fit between the measured and computed gravity anomalies. The bottom figure depicts the model used for the computed anomalies.

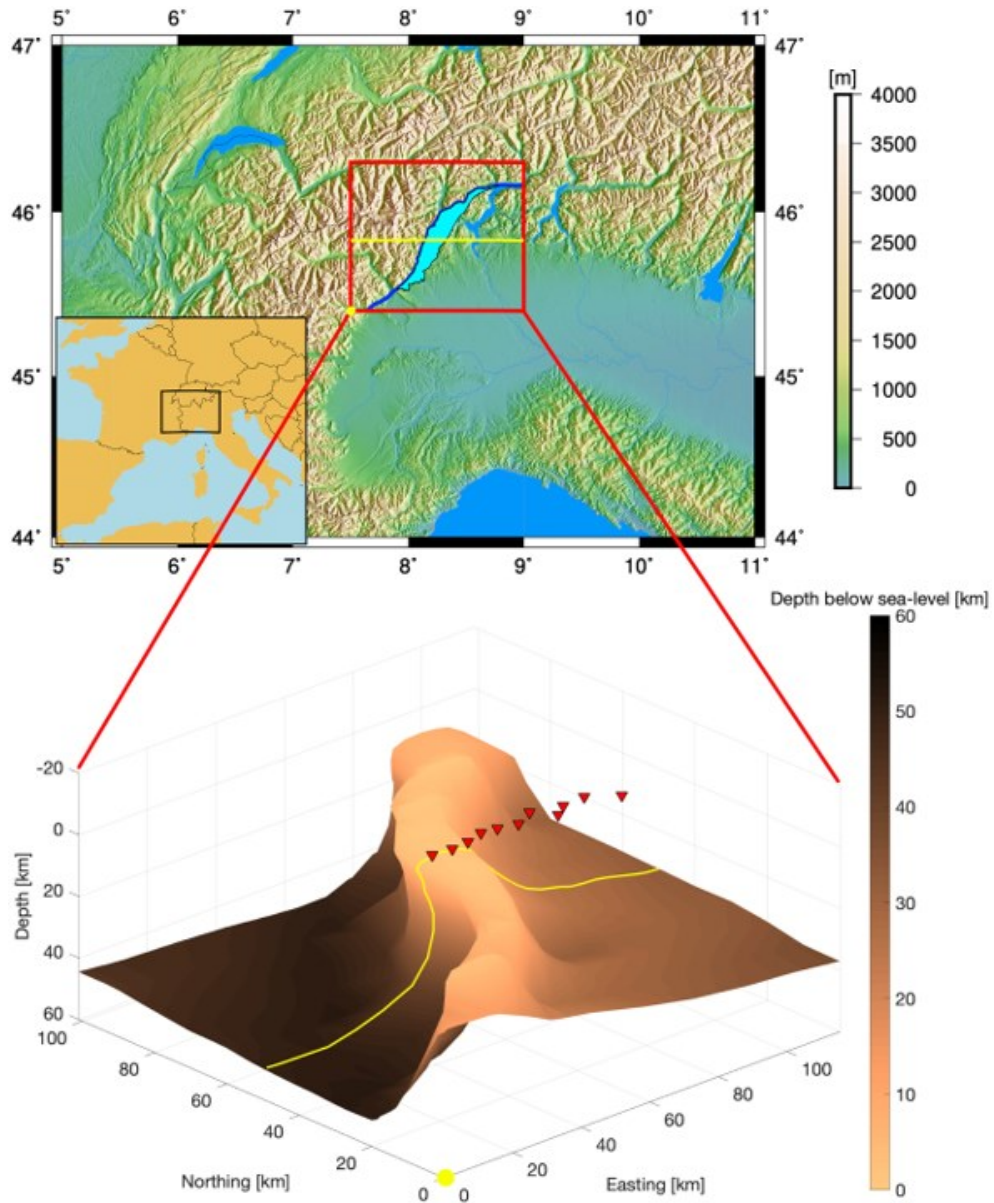


Figure 4: Figure from Scarponi et al. (2021) showing their study area (top figure) and the perspective view of the IGB 3D density model (bottom) obtained by Scarponi et al. (2020). The red triangles represent a temporary seismic array (IvreaArray) installed specifically for their study. Refer to Scarponi et al. (2021) for more details on this figure.

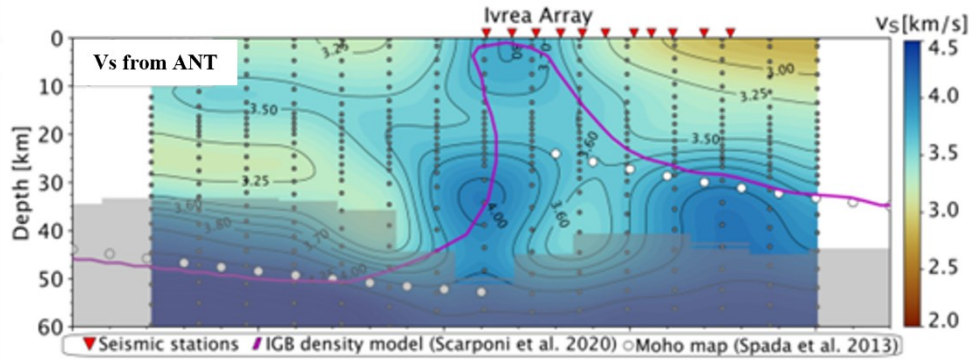


Figure 5: Figure from Scarponi et al. (2023) showing a vertical cross-section of the 3D V_s model obtained in their study through ANT. White dots represent the Moho depth from Spada et al. (2013), red triangles on top indicate the location of the IvreaArray seismic stations. The Magenta contour represents a cross-section through the 3D IGB density model from Scarponi et al. (2020). Refer to Scarponi et al. (2023) for more details on this figure.

1.3. Project DIVE

Project DIVE is an international and multidisciplinary effort aimed at understanding the geological structure, chemistry, physics and microbiology of the continental crust and the crust-mantle transition (Pistone et al., 2017). To achieve these goals, three drilling operations have been planned to be performed at key sites within the IVZ (see Figure 1): Megolo, Val d'Ossola (DT-1A); Ornavasso, Val d'Ossola (DT-1B); and Balmuccia, Val Sessia (DT-2). The DT-2 drill site is proposed to be on top of the BP, which outcrops between the towns of Balmuccia and Isola (see Figure 6). The site requires geophysical characterization of the subsurface for strategic decisions on the drilling location and orientation, and the seismic reflection method was the preferred tool for this task. For that reason, the SEIZE (SEismic Imaging of the Ivrea ZonE) and Hi-SEIZE (High resolution SEismic Imaging of the Ivrea ZonE, this study) seismic surveys were planned near the prospective location of the drill site.

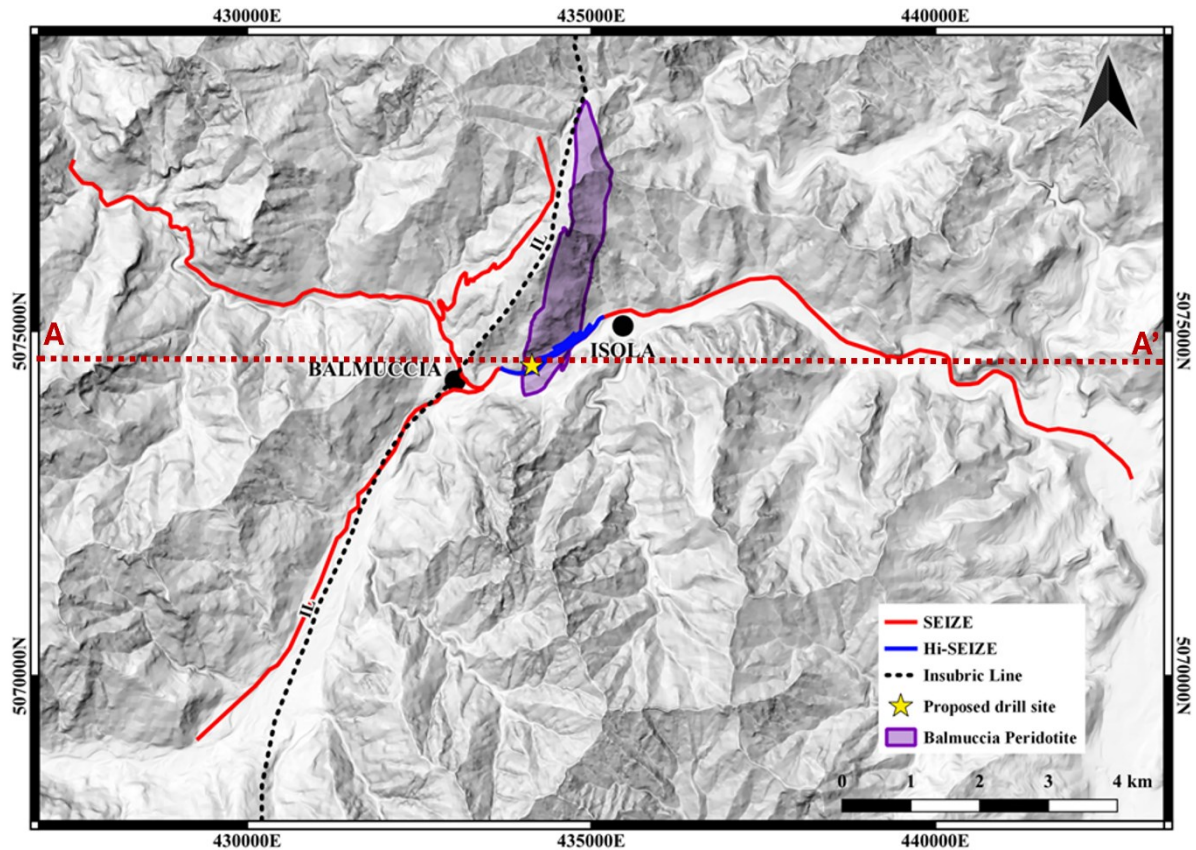


Figure 6: Map illustrating the extent of the SEIZE and Hi-SEIZE seismic surveys as red and blue lines respectively. The proposed drill site by project DIVE is marked as a yellow star on top of the Balmuccia Peridotite drawn in violet. The dark-red-dashed line shows the location of the cross-section depicted in Figure 7. IL: Insubric Line.

The SEIZE seismic survey was carried out in 2020, designed specifically to image the top of the IGB and the subsurface structure of the BP (Ryberg et al., 2023). It was a controlled source seismic survey along two crossing profiles (one ca. 11 km long, NNE-SSW and one ca. 16 km long, E-W trending). Two different receiver spreads were used: a fixed spread of receivers spaced 250 m apart, and a denser rolling spread of receivers with a 20 m interval spacing. Ryberg et al. (2023) used the data from the fixed spread to apply an inversion approach based on Bayesian statistical method using Monte Carlo search with Markov chains to create a 3-D P-wave velocity model (Figure 7). They interpreted that the BP is a high velocity body (6 - 7.5 km/s) that extends from surface down to 3 km depth, therefore suggesting that the BP is not an isolated body, but a downward broadening body connected to the IGB. A discussion will be done in Section 8 comparing the results of their work with what has been obtained in this thesis.

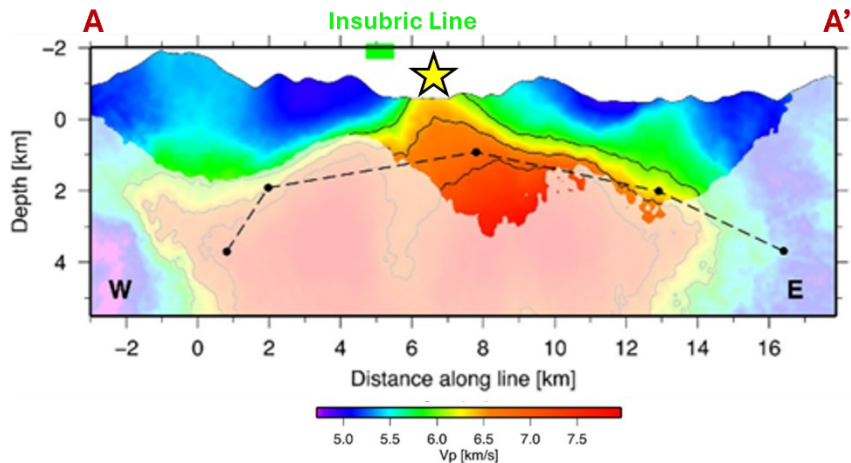


Figure 7: Cross-section through the 3D velocity model of Ryberg et al. (2023) (see Figure 6 for location). The 6 km/s, 6.5 km/s and 7 km/s velocity isolines (black line) are shown for reference. The planned drilling position is marked as a yellow star. The location and extent of the Insubric Line is marked as thick green line at the top of the figure. The dashed–dotted black line shows the top of the IGB proposed by Scarponi et al. (2020). Figure modified from Ryberg et al. (2023).

1.4. Motivation

The Hi-SEIZE survey was designed to get a clearer seismic image than the SEIZE survey near the drill site. Therefore, the goal of this thesis was to characterize the subsurface at the Balmuccia site using Hi-SEIZE seismic data. However, since the prospective drill site is on top of the BP, the objective shifted towards imaging the BP's geological structure. The latter would allow to answer the question: Is the BP attached to the IGB?

The absence of seismic images of the BP presents a unique opportunity to explain not only the general shape of this geological feature but also its internal structure. Such insights are crucial for reinterpreting the geological structure of the IVZ and determining which theory regarding the BP's emplacement aligns most closely with this work's findings. The technical challenge of processing seismic data acquired in a crystalline environment adds another layer of complexity to this research. Reflection seismology in crystalline rocks imposes several challenges that must be addressed by applying processing approaches that differ from classical imaging of sedimentary structures. In addition, lithologic impedance contrasts in crystalline crust are usually weaker, the spatial coherence of reflections from faults and fractures is quite limited, steep dips are predominant, and the strong contrast between the weathering layer and

the crystalline basement decreases the penetration of the wavefield generated by the source. These problems are evident in the results of previous seismic studies across the Alps (see Section 1.2), which highlight how seismically transparent the area is (Figure 2).

This thesis will be organized as follows: Following this introduction, Section 2 will outline the equipment used, the layout of the seismic survey, and the challenges during the deployment of the equipment. Section 3 will focus on the acquisition and quality control of the seismic data, illustrating the use of the seismic array not only for the Hi-SEIZE survey but also during the SEIZE survey. Data pre-conditioning, a crucial stage that follows acquisition, involves organizing and preparing the data for subsequent processing. This stage is important for this project since different acquisition systems and sensors are used. The specifics of this stage will be covered in Section 4. Initial results from this project, derived through first arrival traveltimes tomography, will be discussed in Section 5. Subsequently, Section 6 will describe the processing approaches and imaging technique applied to the data. A comprehensive interpretation of the results from Sections 5 and 6 will be conducted in Section 7. This will be followed by a discussion in Section 8, which will compare the results from this work with other scientific studies. Finally, Section 9 will conclude the thesis, summarizing the key findings and their implications for the understanding of the area.

2. Survey design

The Hi-SEIZE seismic survey was carried out in October 2020. Three sub-parallel receiver lines and a source line were strategically designed to span the mapped extent of the BP in the area. The receiver lines were intended to be as straight and parallel to each other as possible, with the dual goals of maximizing subsurface imaging and positioning possible out-of-plane reflectors. The survey geometry was designed by Dr. Andrew Greenwood, who supervised the deployment of the receivers and the acquisition of the data.

The source line and receiver Line 1 were deployed along a local route between the towns of Balmuccia and Isola, facilitating their placement through the aimed path with minimum deviations. Lines 2 and 3, positioned within an old quarry characterized by significant topography, presented more difficulties for their deployment. The planned geometry for these lines aimed to utilize the quarry's internal roads, but some of them were unfortunately obstructed by uneven terrain, rocks, and vegetation. Therefore, modifications to their planned geometry were needed. While Line 2 largely adhered to its planned route, Line 3 encountered substantial obstacles during its set up; halfway through, a large rockslide area was encountered (Figure 8), leading to the division of Line 3 into two segments, 3a and 3b, with a significant gap between them. These challenges led to an excess of undeployed receivers, prompting the addition of Line 3c along a discovered clear road between Lines 2 and 3b. Despite deviations from the planned geometry, the implemented modifications allowed for the successful acquisition of valuable data, compensating for the unexpected and difficult terrain conditions. The final geometry is a fixed spread of three sub-parallel receiver lines spaced 40 – 80 m apart and a single source line. In general, the survey is oriented NE-SW and is characterized by a strong crookedness, especially towards its SW end (Figure 9).



Figure 8: A picture taken during Line 3 set up. A large rockslide impeded the continuous set up of receivers. A significant gap was introduced to the geometry, dividing Line 3 into two segments (3a and 3b). Segment 3a finishes behind the photographer. Segment 3b starts after the hill that is observed in the distance.

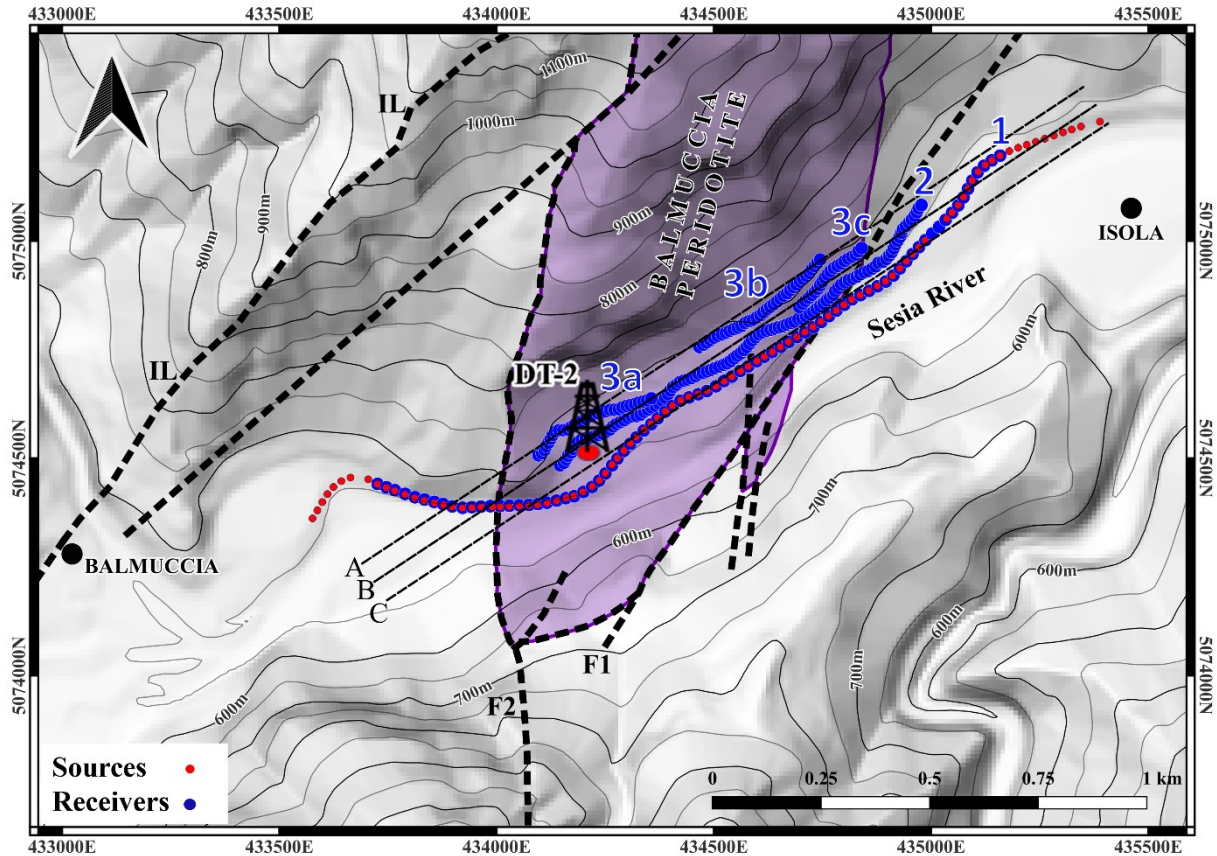


Figure 9: Digital elevation model of the study area showing the final location of 357 receivers (blue points) and 96 sources (red points). Both Line 1 and the source line follow a local road connecting the towns of Balmuccia and Isola. Lines 2 and 3 are deployed along access roads of an old, abandoned quarry. Difficult terrain forced the division of Line 3 into 3 sub lines (3a, 3b and 3c). Dashed lines A, B and C represent the three tomography slices for the 3D tomography (Figure 27). The tentative drill site by project DIVE is represented by a small black rig symbol over a red patch. F1: Main fault cutting the BP representing its NE boundary. F2: Main fault representing the SW boundary of the BP. Insubric Line (IL).

A variety of sensors and acquisition systems were used for the survey (Figure 10): the Sercel Unite nodal system with 80 3C-accelerometers; the CUBE3 nodal system (from GFZ Potsdam) with 80 4.5 Hz-3C-geophones and the Summit X One cabled system with 198 10 Hz-vertical-component-geophones.

The use of 3C receivers was aimed at acquiring possible reflections from steeply dipping geological structures more effectively, as the horizontal components are better suited for detecting the reflected wavefield in such scenarios. Moreover, the ability to observe specific

shear wave behaviors, including variations in Poisson's ratio, shear wave splitting, polarization changes, and differences in velocity between polarized modes, could offer critical insights into geological features.

The nodal systems were combined to build Line 1, whereas Line 2 and 3 used the cabled system. The receiver deployment strategy for the Hi-SEIZE survey was initially planned with a 10 m receiver interval and shot points every 20 m. For Line 1, the goal was to fill the gaps within the sensors from the denser rolling spread from the SEIZE survey. That would be achieved by inserting sensors into the 20 m gaps between its receivers, aiming for a synergistic effect that would provide a clearer subsurface image if both surveys were to be merged in a future study. To save deployment time, distances were measured using as reference the markings already made for SEIZE. This strategy hinged on the assumption that the receiver spacing was consistently 20 m. However, during deployment, it was discovered that it varied between 19 and 22 meters. This was due to a grid-based deployment approach, rather than maintaining exact distances between sensors. Upon further inspection, the receivers from the Hi-SEIZE survey that were already deployed had an interval spacing of 11 m. Then, the plan of closely integrating with SEIZE was abandoned. Under time constraints, the remaining receivers on Line 1 were deployed at an 11 m interval to be consistent with the sensors already deployed. This adjustment also impacted the shot point interval, extending it to 22 meters. Additional shot points to increase the fold on the edges of the seismic survey extended the shot line (~242 m to the NE and ~198 m to the SW). Lines 2 and 3 adhered to the original plan with a 10 m receiver interval. The final receiver line geometry is as follows (Figure 9): Line 1 used 80 3C-accelerometers and 80 4.5 Hz-3C-geophones, interleaved every 11 m, making it ~ 1750 m long. Line 2 was established with 109 10 Hz-vertical-component-geophones deployed every 10 m (~1070 m long). Line 3 was set up with 89 10 Hz-vertical-component-geophones at a 10 m spacing, composed by three sections: 3a (~310 m long), 3b (~350 m long) and 3c (~200 m long).








LINE	RECEIVER	ACQUISITION SYSTEM	SOURCE
1	80 3C-Accelerometers, linear response up to 800 Hz 	SERCEL UNITES 	Prakkla-Seismos vibrator 17.000 Kg 4 shots per shot point
1	80 3C-Geophones, 4,5 Hz 	CUBE3 (GFZ Potsdam) 	Sweep 12-140 Hz linear, 10-second sweep and 3-second listening time
2, 3a, 3b, 3c	200 10 Hz-Vertical-component geophones 	SUMMIT X ONE 	

Figure 10: Images of the sensors and acquisition systems used in each receiver line. Each receiver is shown with its parameters. To the right a photograph taken during acquisition of the vibroseis used. The Vibroseis characteristics and the sweep parameters are described at the top of the photograph.

The source was a 17.000 Kg Vibroseis (Figure 10), emitting a 10 s linear sweep from 12 to 140 Hz with a 3 s listening time. The selection of frequencies for the sweep was guided by two main considerations: First, the aim was to ensure compatibility with the seismic data collected by SEIZE, which utilized a linear sweep from 10 to 120 Hz, necessitating a similar frequency range in our data. This would allow for a seamless combination of the surveys. Second, given that SEIZE employed three 17,000 Kg Vibroseis trucks, which contributed to a different energy input, the sweep used for Hi-SEIZE was adjusted to a higher frequency to compensate for this difference.

3. Data acquisition and quality control

Prior to collecting the Hi-SEIZE data, the seismic array was deployed to listen to the SEIZE survey, aiming to gather extra seismic information beneficial to both research teams. This phase also served as a practical test to ensure all systems were operational. At the start of SEIZE, lines 1, 2, and 3 were ready for acquisition. However, Line 1 was set up without the additional 4.5 Hz-3C-geophones, as these were utilized by the SEIZE crew in their roll-along survey. The nodal system recorded data continuously, relying on Vibroseis time breaks for post-process seismic data extraction. The cabled system was radio-triggered, connected to their Vibroseis, but faced challenges with unstable radio communications, leading to missed triggers for several Vibroseis points (VPs) distant from our array. Unfortunately, over 200 GB of seismic data from the 8-day survey are for now left unusable because the SEIZE team has not provided the necessary GPS positions of their VPs or the time breaks essential for data extraction from the nodal system.

Once the SEIZE survey was finished, the 4.5 Hz sensors were received and Line 1 was completed for the Hi-SEIZE survey. A single CUBE3 recorder was set up in the Vibroseis to record the time breaks necessary for data extraction. The acquisition ran smoothly, although infrastructure along the route reduced the number of VPs from 100 to 96 for safety reasons (gaps along the source line can be seen in Figure 9). Because the route was open to traffic throughout the acquisition, each VP was shot four consecutive times to improve the signal-to-noise ratio. The acquisition lasted 5 hours and around 73 GB of seismic data was acquired.

During the acquisition, field quality control of the seismic data varied significantly between the different acquisition systems used. The SUMMIT system, equipped with real-time communication capabilities, allowed for immediate monitoring and assessment of station status during data acquisition. In contrast, the nodal systems lacked real-time communication, necessitating post-acquisition data retrieval and quality check. The initial quality of the raw data from lines 2 and 3, prior to sweep correlation, was good. The noise levels for these lines were within expected norms. Data recovery was excellent, with 99.9 % of the traces acquiring seismic data with no technical issues. For Line 1, post-analysis revealed a more complex situation regarding the noise levels. The allowance of car traffic near the receiver line introduced significant noise to the data (Figure 11), a disruption not experienced by Lines 2 and 3 since they were positioned further from the route. Although sensors with technical issues were found, data recovery was still excellent, with 98 % of the traces acquiring seismic data.

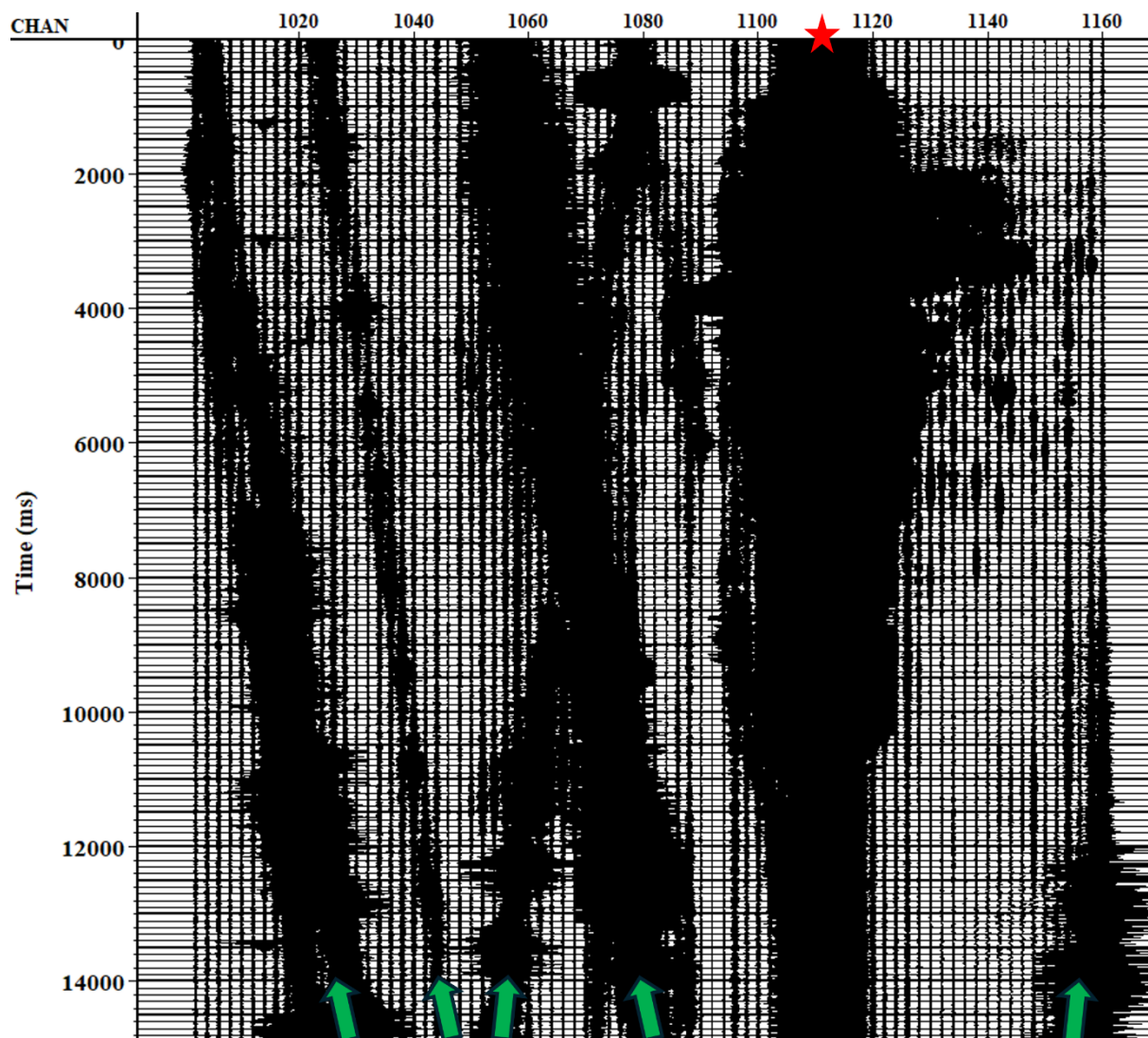


Figure 11: Shot gather N°1112 showing the uncorrelated data from the Unite system at Line 1. This gather is one of four gathers obtained at the same VP position. The traffic noise is marked with green arrows. The vibroseis position is marked with a red star.

4. Data pre-conditioning

Because the time breaks from the Vibroseis were transmitted via radio connection, the seismic data acquired with the SUMMIT system is automatically organized into SEG-D files. Each file stores the seismic traces from the receivers for a single shot point. These are 13-second-long traces that will produce 3 s traces once correlated with the Vibroseis sweep. The traces are organized and stored in 4 separated segy-formatted files representing lines 2, 3a, 3b and 3c.

The seismic data from the Unite and CUBE3 systems require a process of data extraction as a preliminary step. This process uses the time breaks logged by the CUBE3 recorder attached to the Vibroseis. A key user-defined setting for the extraction process is the duration in time of the traces to be extracted. Therefore, 15-second-long traces are extracted to obtain 5 s traces after their correlation with the Vibroseis sweep. Traces with a length of 13 s would have been adequate to match those from the SUMMIT system. However, it is preferred to trim the traces post-extraction. Two separate segy-formatted files are generated to store the data from the Unite and CUBE3 systems separately. The data will be merged once a homogenization process is performed (see Subsection 4.2) since two different sensors were used.

4.1. Vertical stacking and sweep correlation

Vertical stacking is a process typically used in land seismic acquisition to increase the source strength and enhance the signal-to-noise ratio. Several shots are produced successively at each shot point and recorded by the seismic array. Then, these successive shot gathers are added together without any static or dynamic correction applied. Different approaches can be used for the summation of the traces to reduce the effect of various types of noise. As shown in Section 3, the seismic data from Line 1 was affected by strong traffic noise. Therefore, Diversity Stacking (DVS) is the chosen approach, since it has been proved that it is effective on reducing the effect of noise bursts produced by vehicles moving along the seismic line (e.g. Klemperer, 1987). The process divides each trace into time windows. Then, for each window, the average of the energy is calculated, and its inverse value is used as a scaling factor for every sample within the window. Subsequently, the scaled traces are vertically stacked, and the resultant traces are re-normalized dividing them by the sum of all the scaling factors applied to the

original traces. Therefore, the four shot gathers per shot point from Line 1 (see Section 2) are diversity stacked using a time window length of 1000 ms. Different window lengths (e.g 250 ms and 500 ms) do not show any visual improvement. Figure 12 shows the effectiveness of DVS on reducing the traffic noise. DVS is applied similarly to lines 2 and 3. Although they are not affected by traffic noise, their signal-to-noise ratio will be enhanced by this process.

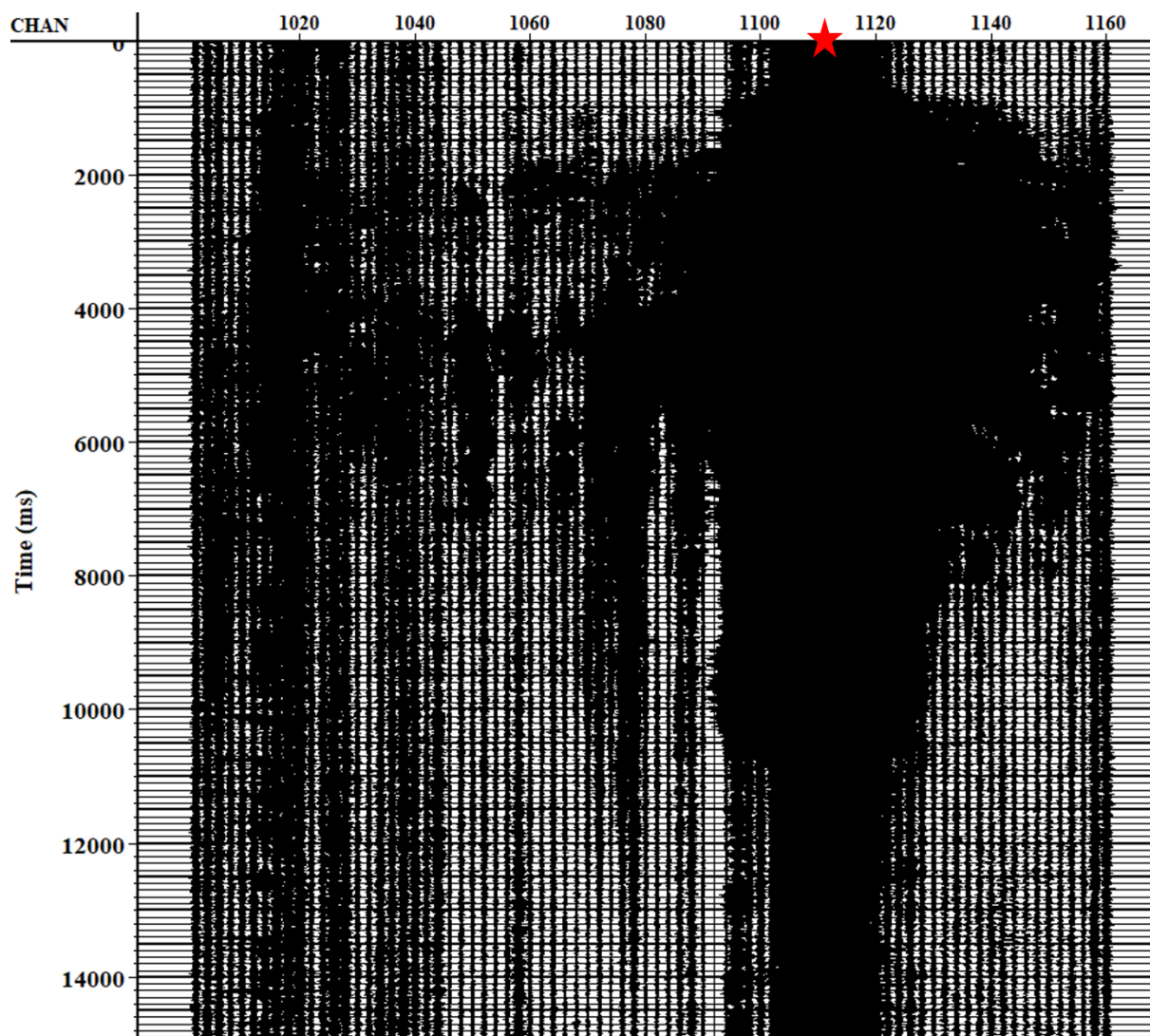


Figure 12: Same uncorrelated shot gather as in Figure 11 after DVS. The vibroseis position is marked with a red star. The strong noise from the traffic is not visible anymore thanks to the DVS process.

After DVS, the traces are correlated with the designed vibroseis sweep (see Section 2) to obtain the final seismic data to be processed. The sweep used for correlation was extracted from

the sweep tests logged by the CUBE3 recorder in the Vibroseis. Figure 13 shows the good quality of the 5-second-long traces for a single shot gather from Line 1 after the sweep correlation.

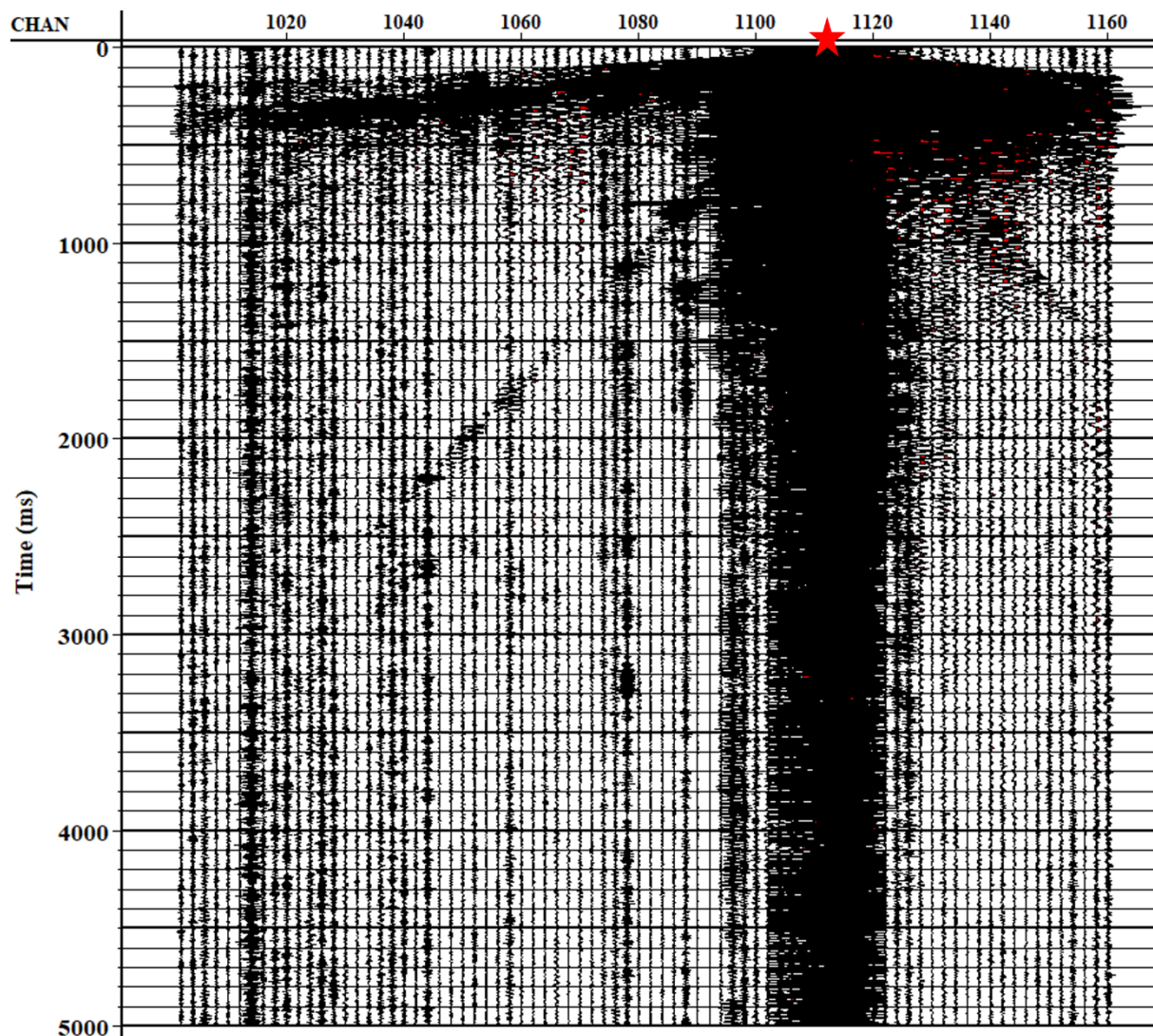


Figure 13: Same shot gather as in Figure 12 after vibroseis sweep correlation. The vibroseis position is marked with a red star.

4.2. Instrument simulation

As shown in Section 2, three different sensors were used. Each sensor is characterized by a different frequency and phase response. Because the seismic data from the three lines are going to be merged, it is necessary to homogenize their frequency content and phase. Therefore,

instrument simulation is applied to the 4.5 Hz geophones and accelerometers. This process will transform the seismic data to the same amplitude and phase response of a 10 Hz geophone.

The complex-valued frequency response of a seismic sensor can be defined as:

$$\frac{Z}{U}(\omega) = \frac{\omega^2}{\omega_0^2 - \omega^2 + i2D\omega\omega_0} = S(\omega) = S_{\omega_0}, \quad \text{Equation(1)}$$

where Z is the measured ground motion, U is the true ground motion, ω_0 is the eigenfrequency of the sensor and D is the damping coefficient. Because the true ground motion must be the same at each sensor, a relationship between them can be found as:

$$Z_a(\omega) = S_a(\omega) U = \frac{S_a(\omega)}{S_b(\omega)} Z_b(\omega), \quad \text{Equation(2)}$$

where $S_a(\omega)$ is the transfer function of the instrument to mimic with eigenfrequency a and $S_b(\omega)$ is the transfer function of the instrument to be transformed. By applying an inverse Fourier transform to the ratio of the transfer functions $\frac{S_a(\omega)}{S_b(\omega)}$, a filter can be defined in the time domain. Then, the convolution of the filter with the traces recorded with the sensor of eigenfrequency b would simulate as if the data was acquired with a sensor of eigenfrequency a .

The simulation from the 4.5 Hz geophones to 10 Hz geophones is straightforward. Damping values for the sensors are obtained from the manufacturer specifications, being 0.56 for the 4.5 Hz and 0.70 for the 10 Hz sensors. The transfer functions are calculated and used to generate the filter through Eq. 2. Figure 14 shows a comparison between the amplitude and phase response of both sensors and the filter applied.

The process for the accelerometers needs an extra step, which is the integration of the acceleration data to the velocity domain. Then, considering that the eigenfrequency of the accelerometer is zero, the corresponding transfer function is equal to 1, which means that the filter is only the inverse Fourier transform of the 10 Hz geophone's transfer function. Figure 15 shows the comparison between the amplitude and phase spectra. The filter in this case acts as a low-cut filter, with a corner frequency of 10 Hz.

Once the seismic data from both sensors are homogenized, a single sgy-formatted file for Line 1 is generated. The seismic data from the other receiver lines are not merged at this point because each line is processed individually (see Section 6.1).

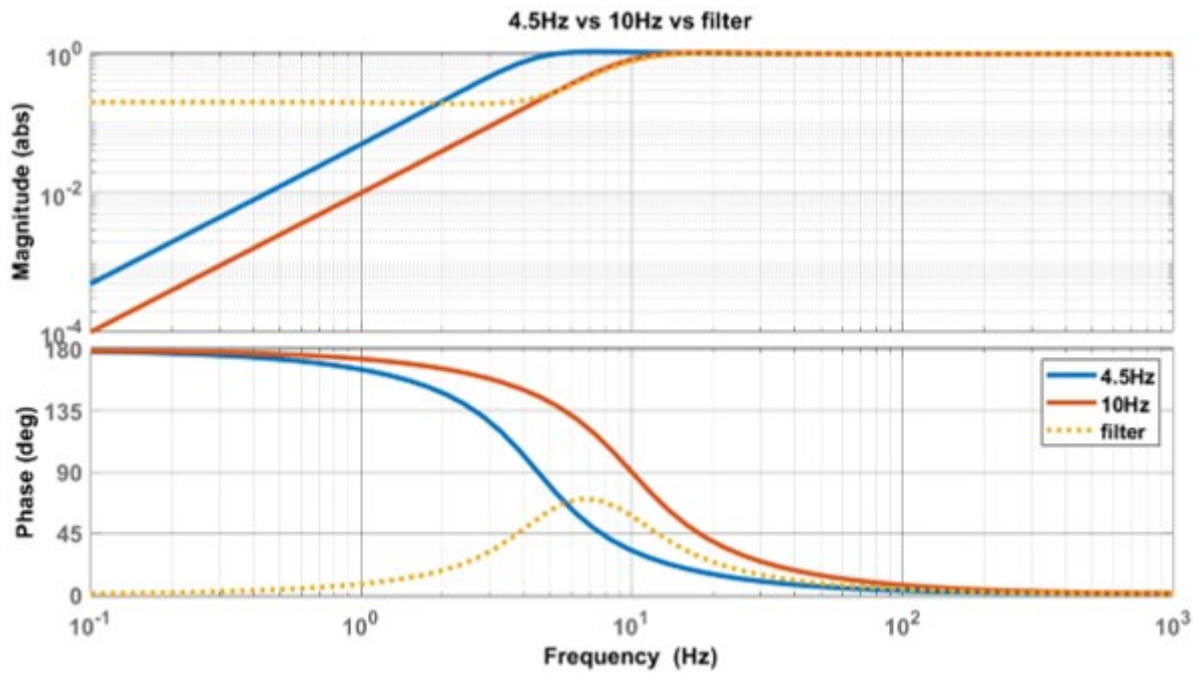


Figure 14: Comparison between amplitude and phase response of the 4.5 Hz and 10 Hz geophone. The yellow-dotted line represents the filter obtained through Equation 2.

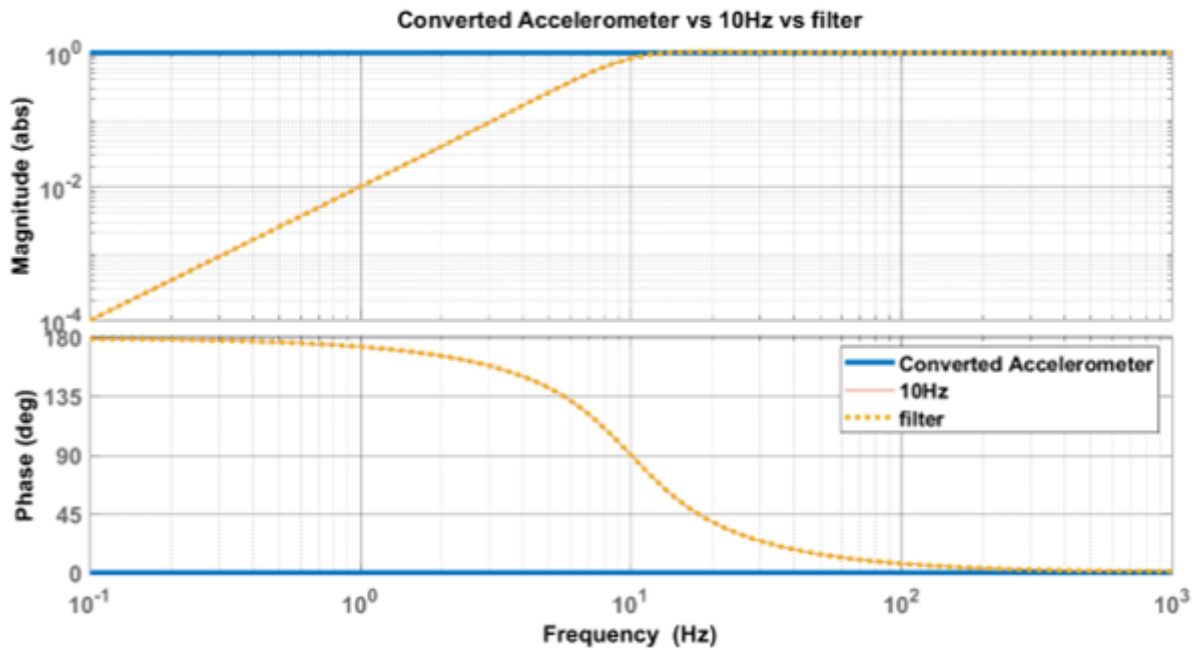


Figure 15: Comparison between amplitude and phase response of the accelerometer (after integration) and 10 Hz geophone. The yellow-dotted line represents the filter obtained through Equation 2.

4.3. Geometry definition

To define the geometry of the seismic data, precise position and elevation of every VP and sensor in the field is necessary. This data was measured with a Real Time Kinematics (RTK) GPS and processed by Ludovic Baron (University of Lausanne). Unfortunately, during the GPS measurements the 4.5 Hz-3C-geophones were not in place, which forced the interpolation of their position from the data acquired. Although VP positions were measured, the GPS data given by the vibroseis company is used to position the VPs, since the built-in GPS in the vibroseis will provide the true shot position. Figure 16 shows the elevation profile and location of each receiver and source. The complicated topography is evident when observing the elevation profile, showing elevation differences up to 50 m between receivers. The station numbering is defined from SW to NE as follows (see Figure 16):

- Stations along the route (shots and receiver Line 1) form N° 984 to N° 1182.
- Line 2 stations from N° 2001 to N° 2109.
- Line 3a stations from N° 3001 to N° 3032.
- Line 3b stations from N° 4001 to N° 4036.

- Line 3c stations from N° 5001 to N° 5021.

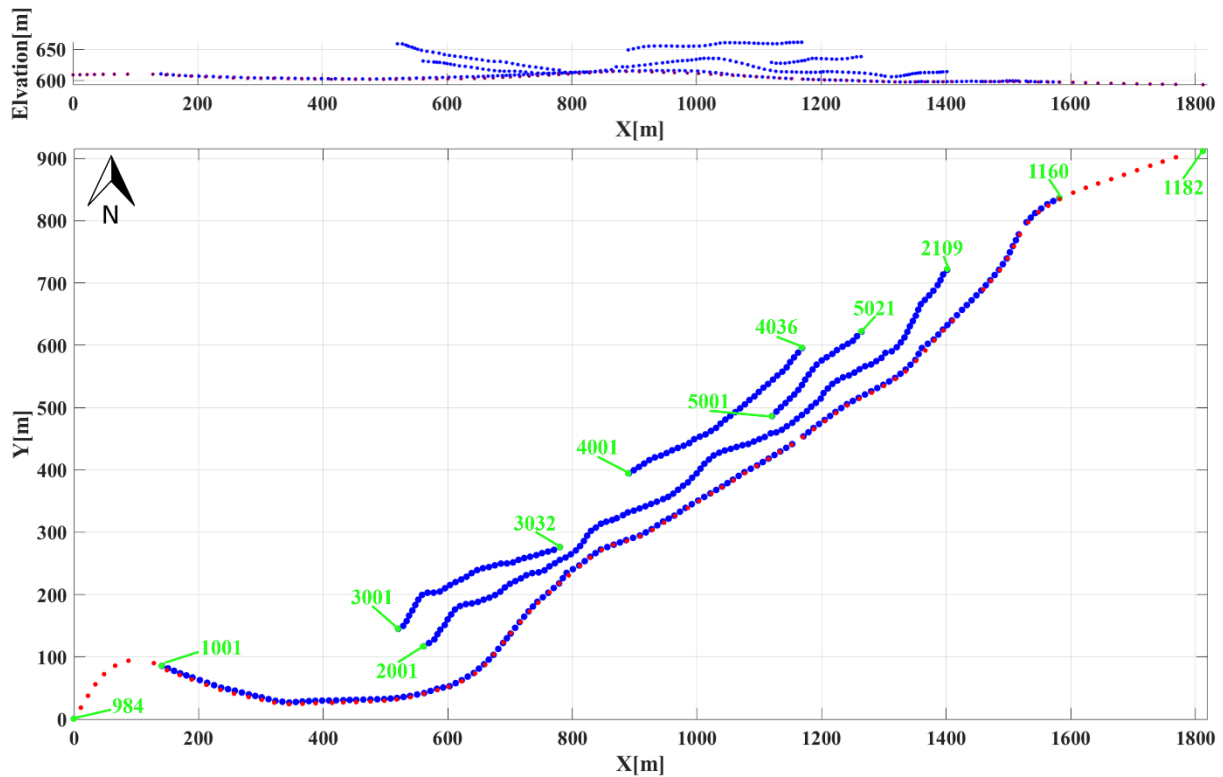


Figure 16: Elevation profile (top) and position (bottom) of receivers and sources. Green circles and numbers mark the start and end of the numbering defined for each line. Red circles: shots. Blue circles: receivers.

After defining the geometry, a second QC is performed to check for possible noise sources or technical problems. Since the base of operations was set up besides Line 2, some of its receivers were affected by the noise produced by an electric generator (Figure 17).

Figure 18 shows a typical shot gather from the survey for Line 1. Even for crystalline rocks, the data appears rather devoid of reflections. Besides the clear P- and S-wave first arrivals, and the air wave (red and blue arrows respectively), only one strong reflection can be identified at approximately 700 ms (Figure 18, black arrow). It can only be identified in eight shot gathers (shot point N° 1030 to N° 1044). The shifted apex with respect to zero offset suggests that it has a strong inline dip. In addition, there are a few reflections with extreme move-outs (Figure 18, yellow arrows) commonly referred to as reflected refractions originated from vertical to sub-

vertical reflectors (e.g. Hole et al., 1996). These reflections are characterized by having the same apparent velocity but opposite moveout to the wavefield that generated them.

There is a strange behavior of the P-wave first arrivals at -217 m offset, which coincides with the West boundary of the BP. This is not caused by topography since the receivers at that position do not have sudden changes in elevation (see the top figure of Figure 16 at $X = 500$ m). Its moveout is reversed to the expected first arrivals, with an apparent velocity of ca. 2000 m/s. Because its velocity is much lower than the expected for a P-wave, it is discarded as a reflected refraction. Therefore, we conclude that this behavior is caused by a thicker low velocity layer in the near-surface.

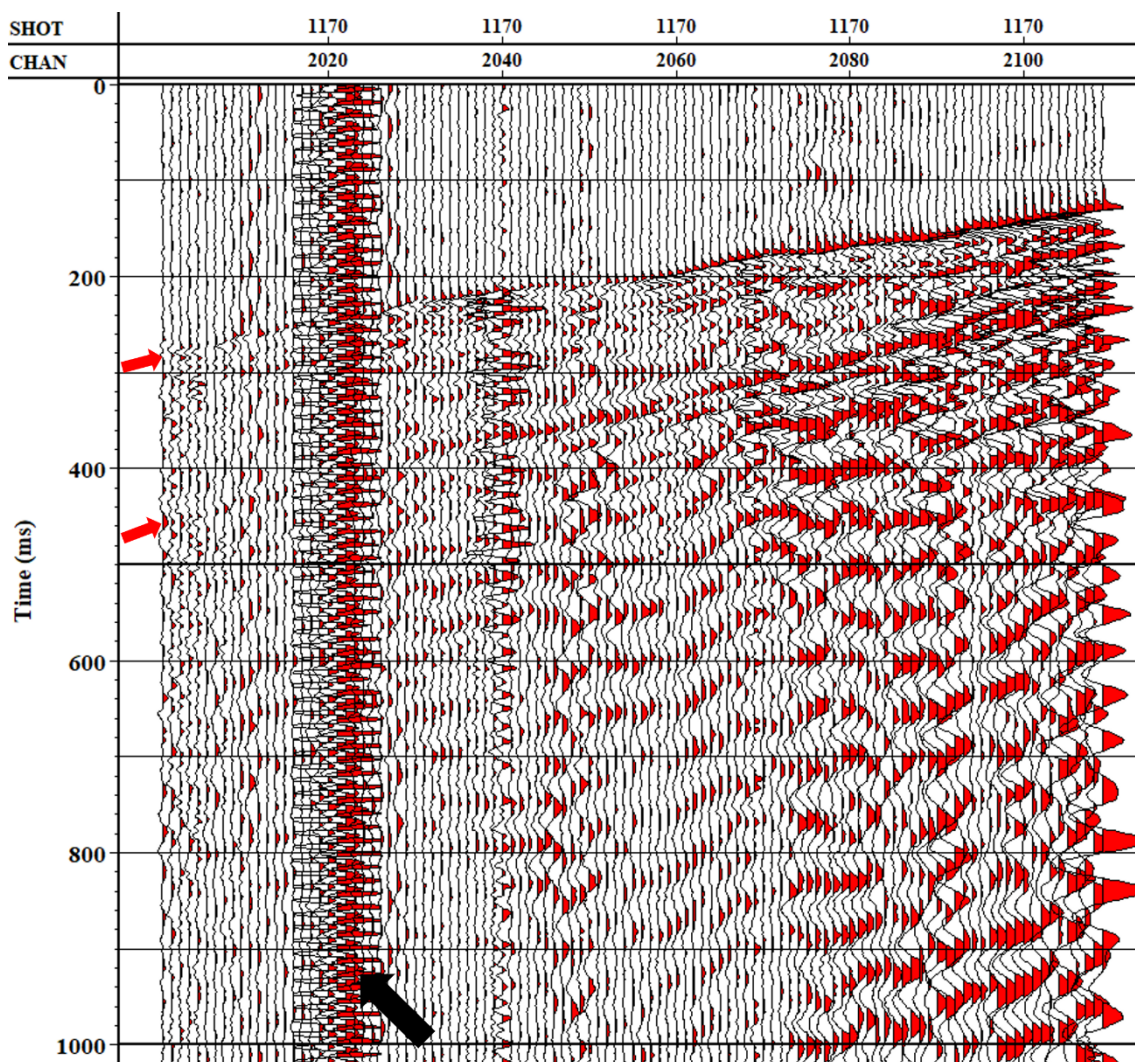


Figure 17: Shot gather N°1170 from Line 2. The black arrow marks the noise produced by the electric generator. Red arrows mark the P and S-wave first arrivals.

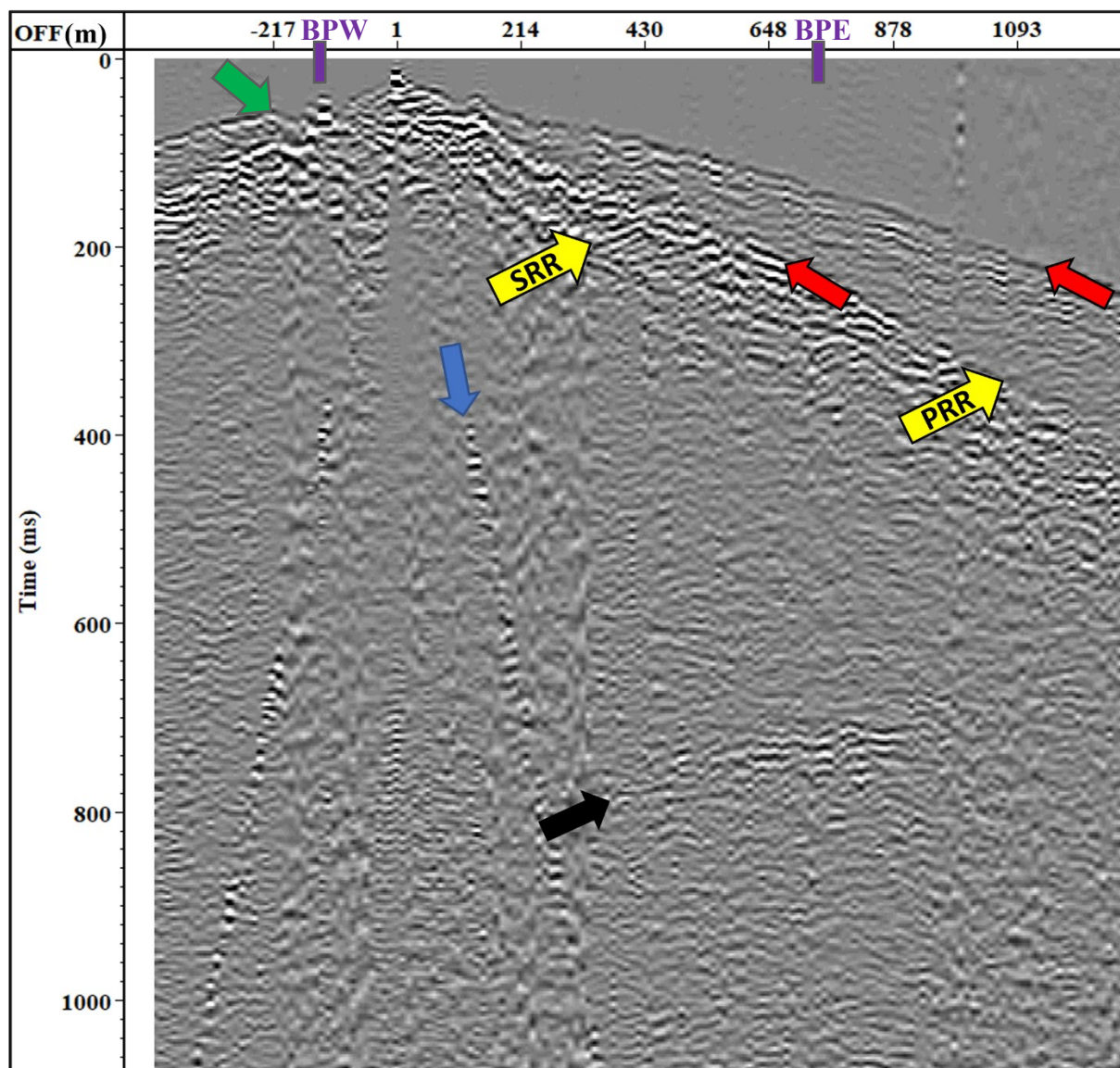


Figure 18: Raw shot gather N° 1040. AGC window of 500 ms applied for better visualization. Colored arrows outline the P- and S-wave first arrivals (red), P and S-wave reflected refractions (yellow), air wave (blue), a reflection at approximately 700 ms (black) and a strange behavior of the first arrivals (green). Thick purple lines mark the approximated position of the West and East boundaries of the BP. SRR: S-wave Reflected Refraction. PRR: P-wave Reflected Refraction. BPW: Balmuccia Peridotite – West boundary. BPE: Balmuccia Peridotite – East boundary.

4.4. Horizontal components

The seismic data from the horizontal components undergoes the same data preparation workflow as the vertical component data (Sections 4.1, 4.2 and 4.3). However, they need an additional pre-processing step.

The 3C geophones were deployed in the field with their horizontal components oriented towards the N-E. Therefore, the North-oriented component describes the horizontal particle motion in the N-S plane and the East-oriented component represents the motion in the East-Weast plane. However, these components need to be rotated into the radial and transverse orientations. A radial orientation will therefore represent the horizontal particle motion in the source-receiver plane and the transverse orientation will represent the particle motion perpendicular to the source-receiver plane. To apply this rotation, a rotation angle is calculated for every pair source-receiver considering their relative position and the receiver's orientation. Then, the rotation angles for each pair source-receiver are input to a rotation matrix to apply the rotation. The traces are rotated following the equation:

$$\begin{pmatrix} R(t) \\ T(t) \end{pmatrix} = \begin{pmatrix} \cos\theta & \sin\theta \\ -\sin\theta & \cos\theta \end{pmatrix} \begin{pmatrix} X(t) \\ Y(t) \end{pmatrix}, \quad \text{Equation(3)}$$

where θ is the rotation angle, $X(t)$ and $Y(t)$ are the East and North components respectively, and $R(t)$ and $T(t)$ are the radial and transverse components respectively.

The horizontal-component data is analyzed to identify if more signals of interest (e.g. reflections or reflected refractions) can be detected when compared to the vertical-component data. Figure 19 shows a comparison between the three components for a single shot gather. Neither in this nor in other shot gathers additional information is brought by the horizontal components. What is more, the single reflector that is identified in the vertical component is less coherent and more difficult to identify. The radial and transverse components do not detect this feature as clearly as in the vertical-component data, which allows to conclude that this signal is polarized in the vertical component and corresponds to a P-wave reflection from a deep reflector.

Because the horizontal components do not show any additional seismic features and because the coherency of the only visible reflector is not enhanced, the focus and efforts of this

research will be towards processing and analyzing the vertical-component data. However, a more complete analysis of the horizontal components should not be discarded for a future work.

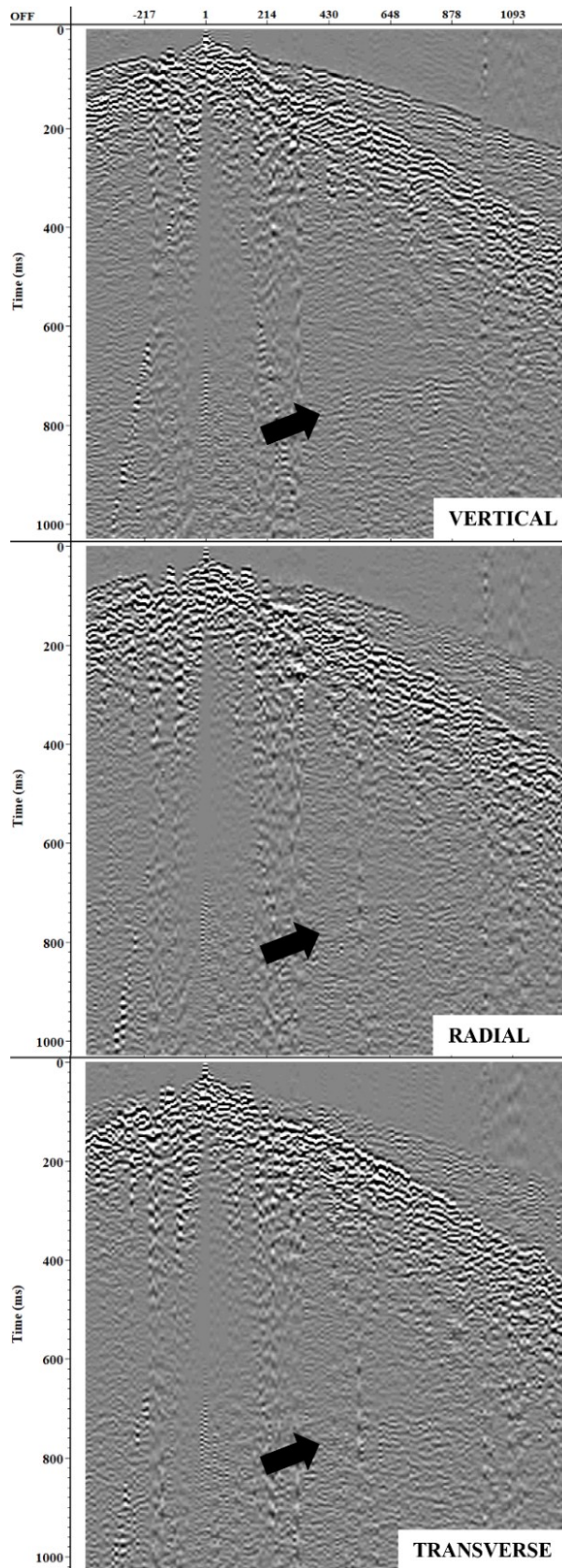


Figure 19: Comparison of the vertical, radial and transverse components from Line 1. The black arrow shows the position of the reflector for each component. An AGC window of 1000 ms was applied for visualization. Offset in meters.

5. First arrival traveltimes tomography

The purpose of conducting first arrival traveltimes tomography is twofold: 1) to construct a velocity model of the near-surface for the application of refraction static corrections; and 2) to obtain an initial understanding of the velocities and potential shallow structures. To extract the first P-wave arrival times, the seismic data is transformed from zero to minimum phase. This conversion is done because the onset of the first arrivals is easier to identify in minimum phase data, allowing for a more precise extraction of the arrival times. The conversion is performed by the convolution in the time domain of the zero-phase data with a phase shift operator created based on the vibroseis sweep (Robinson & Treitel, 2008). Figure 20 shows a shot gather before and after the conversion. To enhance the visualization of the first breaks an Automatic Gain Control (AGC) window of 500 ms is applied. The shot points beyond the receiver spread have no reverse observations and are discarded from the tomography data set. The quality of the first-arrivals is very high, and it is possible to extract traveltimes for all 27,768 traces. Figure 21 shows the traveltimes plots for seven shot positions from Line 1. The strange behavior of the first arrivals described in Subsection 4.3 (see Figure 18) can be observed in every traveltimes curve at $X = 400$ m. Except for the near offsets, apparent velocities range from 6 to 8 km/s.

The data uncertainty of the picked traveltimes is obtained as the Root Mean Square (RMS) of the time differences between the forward and reverse traveltimes. The major constraint for this approach is that the difference must be calculated between receiver-shot pairs with the same offset. Therefore, the use is limited to the travel times picked on the accelerometers from Line 1, since the 4.5 Hz-geophones do not coincide with the VPs. Traveltimes picked on lines 2 and 3 are also discarded for the analysis since there are no reverse observations from their receiver positions. Figure 22 shows a histogram of the time difference between forward and reverse traveltimes. It shows an expected normal distribution, with a mean value of ca. 0 ms and a standard deviation of ca. 4 ms.

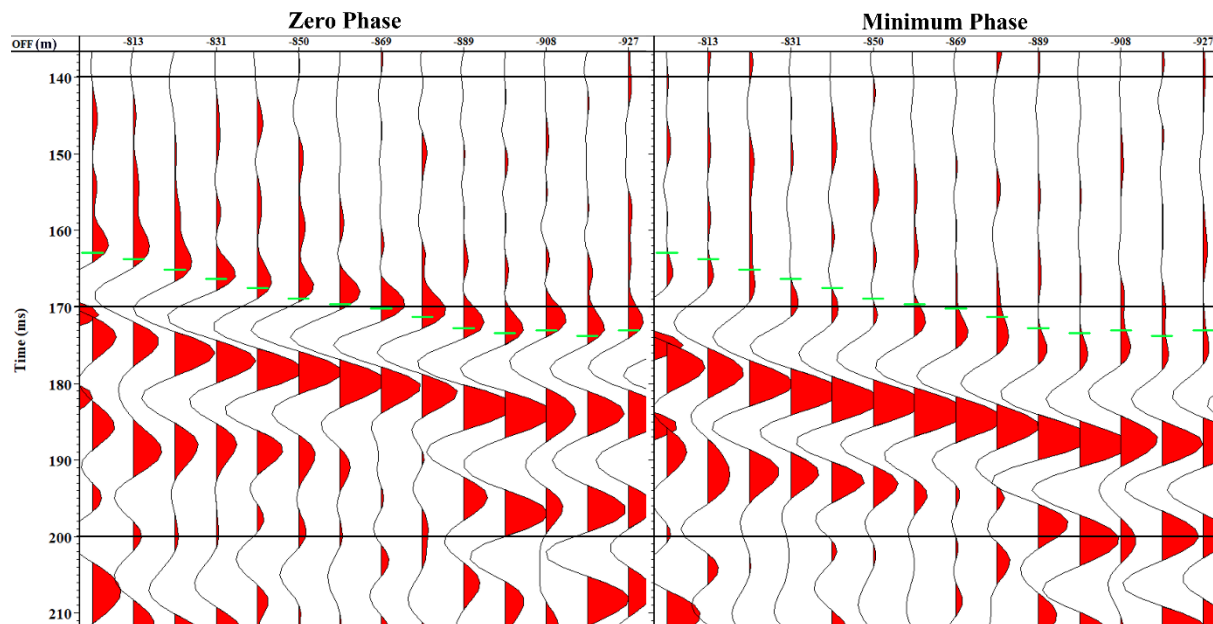


Figure 20: Before (left) and after (right) minimum phase conversion. First breaks picked on the minimum phase data are shown as green lines on both panels for comparison.

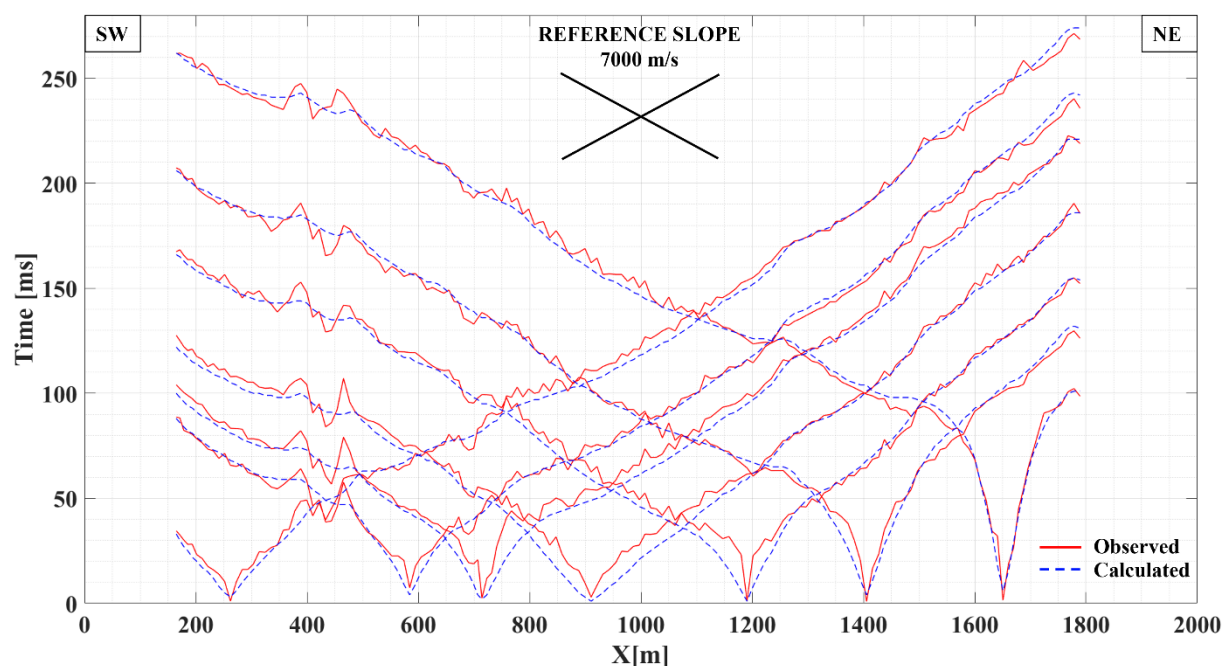


Figure 21: First arrival times from Line 1 for seven selected shots. Observed traveltimes are plotted as continuous red lines. Blue-dashed lines represent the calculated traveltimes obtained for the final velocity model in the two-dimensional inversion (see Subsection 5.1).

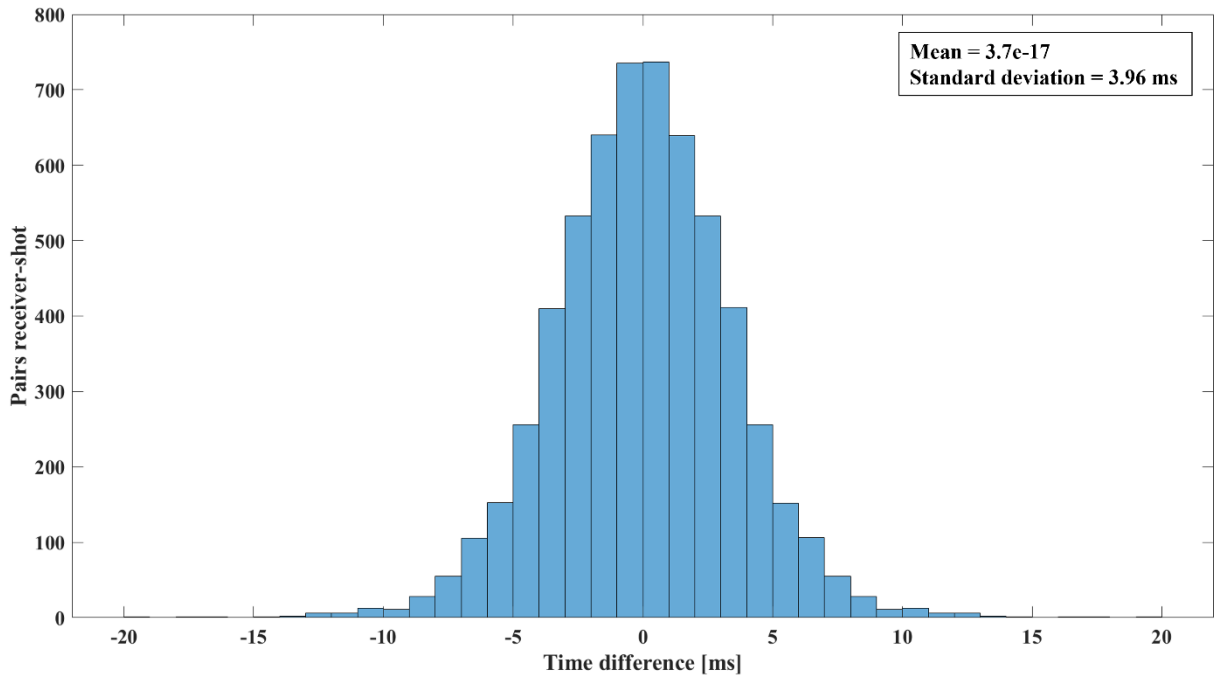


Figure 22: Histogram of the differences between forward and reverse traveltimes. The bin size used is 1 ms, equal to the sampling interval of the receivers. The y axis represents the number of pairs receiver-shot, and the x axis is the time difference between the forward and reverse traveltimes.

The SIMULR16 (Bleibinhaus & Gebrande, 2006) code is used for traveltimes tomography. It is based on the inverse method by Thurber (1983) and the eikonal solver of Hole & Zelt (1995) to compute time fields and rays. It applies a damped least-squares inversion to compute model perturbations applied later to a previously defined initial model. The perturbations are applied iteratively, reducing at each iteration the residual between the observed and calculated traveltimes. Model perturbations are computed according to:

$$\Delta \mathbf{m} = (\mathbf{G}^T \mathbf{G} + \Theta^2 \mathbf{I})^{-1} \mathbf{G}^T \Delta \mathbf{d}, \quad \text{Equation(4)}$$

where \mathbf{G} is the data kernel, Θ is the damping parameter, \mathbf{I} is the identity matrix and $\Delta \mathbf{d}$ is the residual between the current model traveltimes and the observed traveltimes \mathbf{d} .

5.1. Two-dimensional inversion

Because reverse observations are only available for Line 1, these data are inverted separately. To account for the crookedness, the true geometry is respected, but velocity variations perpendicular to the line are not allowed ('2.5D inversion'). The selection of an appropriate initial model is essential for every inversion algorithm. In general, a velocity gradient with increasing velocities in depth is considered as the starting model. In addition, the model can be tailored to consider refractors observed in the traveltimes curves. A constant velocity is chosen as the initial model since it is the simplest velocity model that could be proposed. What is more, there is no information of the subsurface velocities from other geophysical surveys to create a more complex initial velocity model. Since apparent velocities in a range from 6 to 8 km/s (not considering the near offsets) are observed in the traveltimes curves (Figure 21), a constant velocity model of 6 km/s is considered. This constant velocity approach was possible because the near offsets demand lower velocities than 6 km/s. Thus, the algorithm decreases the velocities at the near-surface, creating on its own the necessary velocity gradient for ray penetration.

The velocity models in SIMULR16 are represented by a grid of nodes, with the space between the nodes computed through a tri-linear interpolation. Each node is characterized by its position in three-dimensional space (x,y,z) and a corresponding velocity. Rather than using a fixed grid in the inversion, a grid refinement strategy is adopted which eliminates the dependency on the initial velocity distribution. This implies that the results will not be affected by a pre-defined model with a proposed velocity structure, and the resultant velocity distribution will be fully data-driven. Figure 23 shows the sequence of models obtained for increasingly finer grids. The initial velocity model, to obtain the inverse result (a), is the constant velocity of 6 km/s, defined by a coarse node grid. Each subsequent velocity distribution is used as a starting model for the next refinement step. The refinement process continues until the misfit between the observed and calculated traveltimes reaches the estimated data uncertainty. The final velocity model (Figure 23d) has an RMS misfit of 4 ms which corresponds to the estimated data uncertainty. It shows essentially two layers: A body with high velocities ranging from 6 to 8 km/s, overlain by a shallow and thin low-velocity layer (velocities < 3 km/s). To the NW, at X = 400 m, a low velocity layer appears, which explains the behavior of the first arrivals noticed at that position in Figure 21.

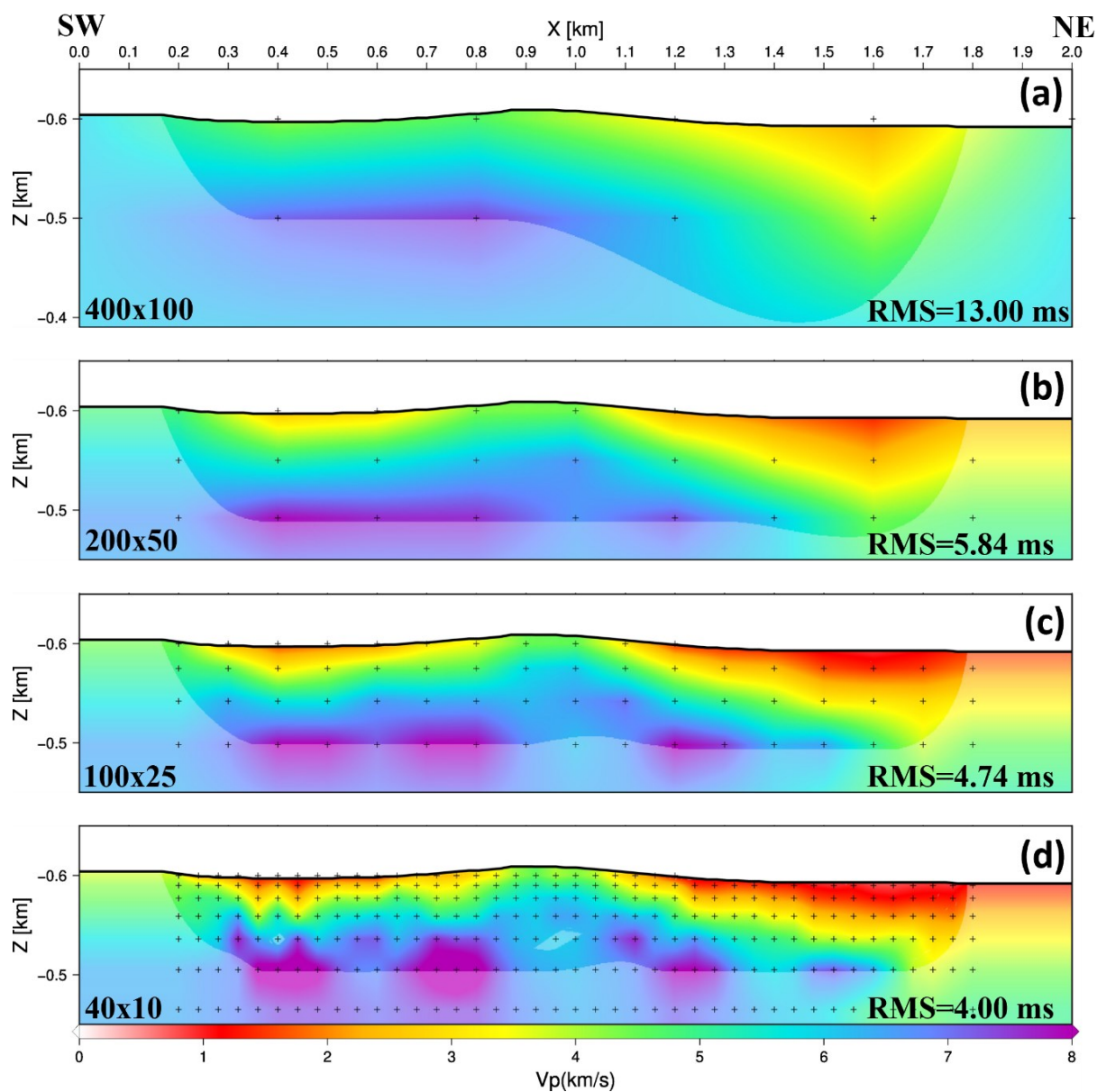


Figure 23: 2.5D tomographic inversion results for increasingly finer grid spacings from (a) to (d). The horizontal and vertical spacings (in meters) are given in the lower left corner of each model. The vertical spacing refers to the uppermost grid layer and increases with depth by 28% in all models. The corresponding RMS misfit is given in the bottom right corner. Areas without ray coverage are semi-transparently whitened. Z axis exaggerated at 2:1.

5.2. Velocity constraints

The sequence of inversions in Figure 23 are obtained imposing a limit on the maximum velocity of 8 km/s. Without that limit, inverted velocities locally reach ca. 9 km/s, while the corresponding model provides the same RMS misfit. To better constrain the maximum velocity the data requires, a series of sequentially refined inversions are computed, each with a different upper velocity limit: Model perturbations that lead to higher velocities than the given limit are cropped. Figure 24 depicts the results from this experiment. It shows that a velocity of at least 7 km/s is required to explain the data within the limits of its uncertainty.

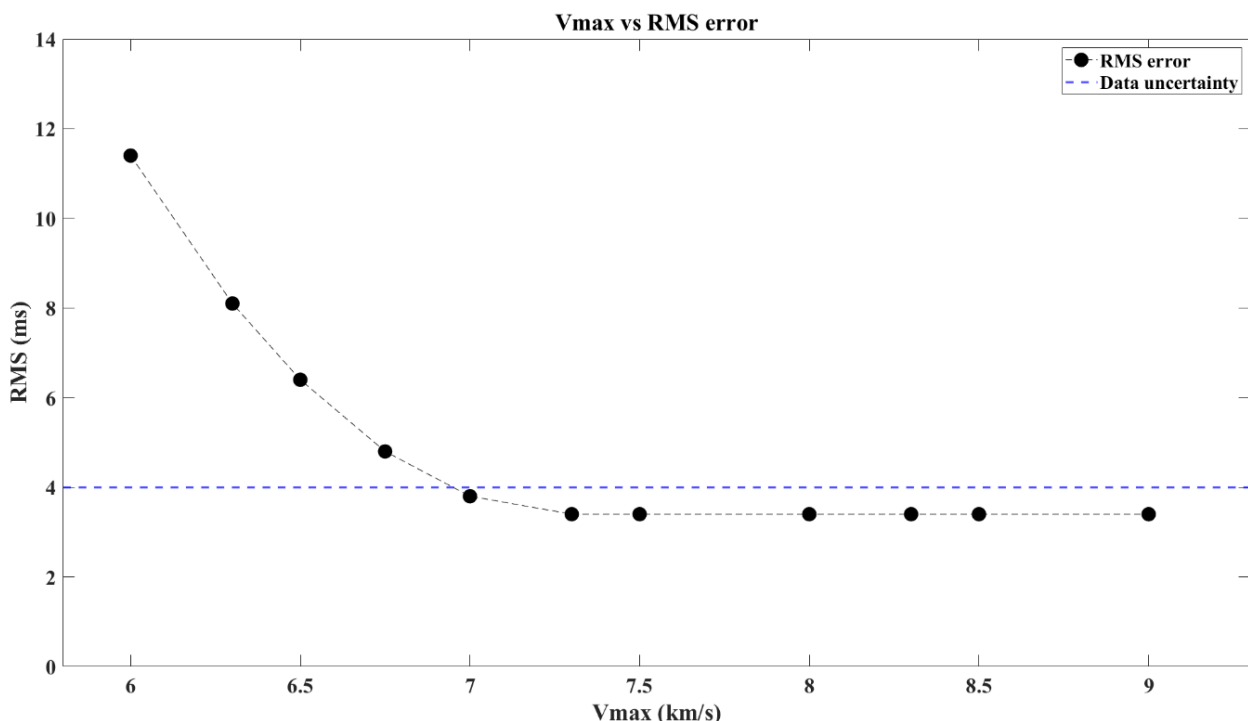


Figure 24: Velocity test for the 2.5D tomography. The X axis represents the maximum velocity allowed in the inversion. The Y axis is the RMS error obtained for each velocity. The mean data uncertainty is shown as a dashed blue line. Only velocities above that threshold can explain the observed traveltimes in the inversion process.

Figure 25 compares the final models obtained imposing a velocity limit of 7, 8, and 9 km/s. The model of Figure 25a with a limit of 7 km/s shows hardly any velocity variation within the lower layer, suggesting that 7 km/s is a good average velocity for this body. Velocities that significantly exceed 8 km/s (Figure 25c) can explain the observed data, but are not consistent

with other constraints (see Section 8). Under the principle of simplicity, it could be argued that the model to be chosen should be the one with a 7 km/s limit. However, the velocities in the area are rather high, with studies showing velocities up to 8 km/s (e.g. Khazanehdari et al., 2000). Therefore, the preferred model is the one with a velocity limit of 8 km/s (Figure 25b). This model allows for some velocity variation within the high-velocity body, which highlights the complex internal structure of the BP.

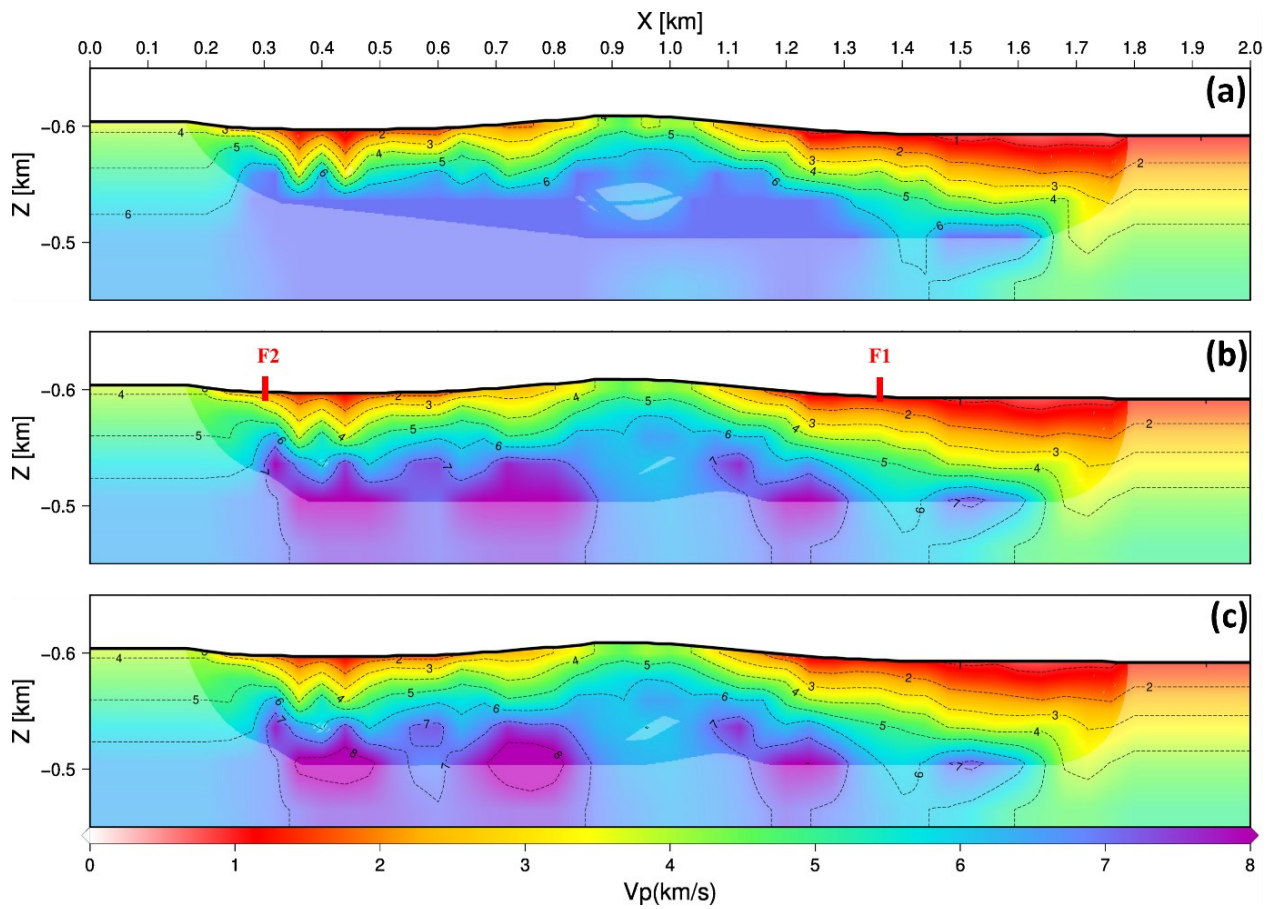


Figure 25: Comparison between velocity models applying a velocity cut-off to the inversion. (a) $V_{max} = 7 \text{ km/s}$. (b) $V_{max} = 8 \text{ km/s}$. (c) $V_{max} = 9 \text{ km/s}$. The chosen model (b) shows the geologically mapped positions of faults F1 and F2 (see Figure 9).

5.3. Three-dimensional inversion

The grid refinement process for the 3D tomography is identical to the two-dimensional inversion but performed across 3 pre-defined slices (see dashed lines A, B and C, Figure 9).

These slices are positioned to obtain a representative velocity model of the subsurface under each receiver line. Figure 26 summarizes the improvement of the RMS misfit for each refinement step and Figure 27 shows the resulting velocity model.

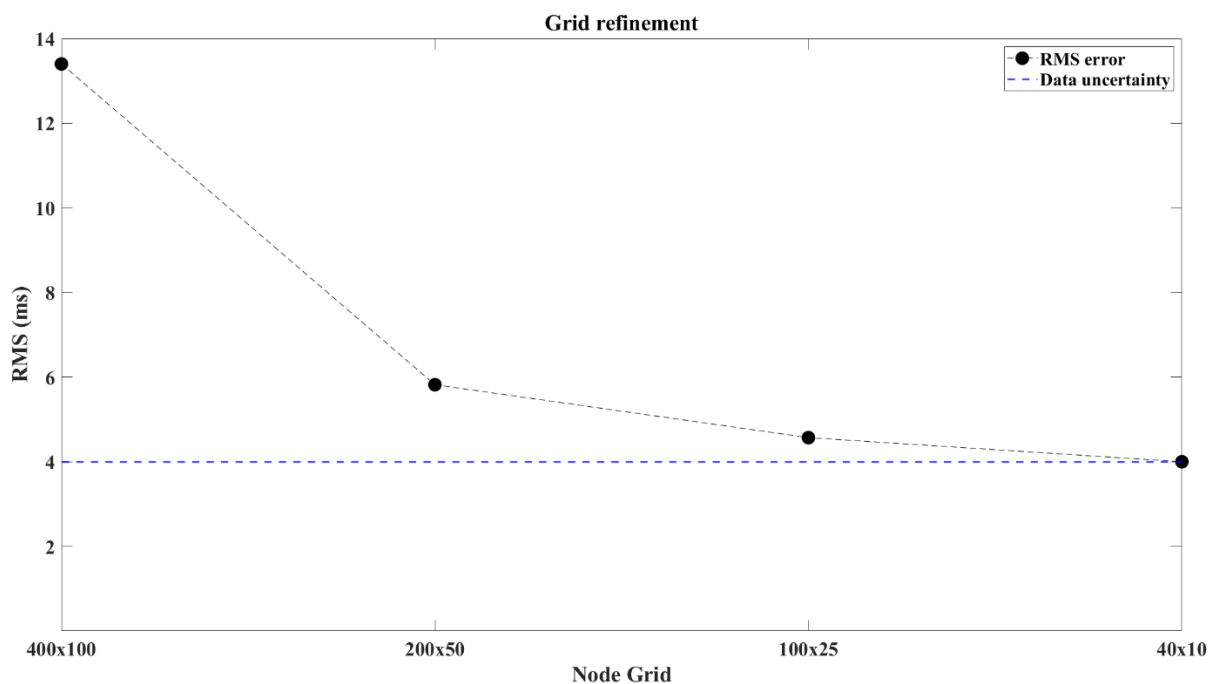


Figure 26: RMS misfit for increasingly finer grid spacings during the grid refinement process for the three-dimensional inversion. The X axis represents the grid configuration (in meters), and the Y axis is the RMS error obtained for each grid. The mean data uncertainty is shown as a dashed blue line.

The velocities obtained for the 3D tomography on Slices A and B are less reliable compared to the 2.5D case. This is caused by the geometry of the survey since lines 2 and 3 are off-line from the sources and there are no reciprocal shots for their position. This limits the amount of crossing ray paths, which translates to less constrained velocities in the results. Therefore, the analysis and interpretation of velocities are based on the 2.5D tomography. Nevertheless, a 3D tomography is necessary to obtain a near-surface velocity model to apply refraction statics.

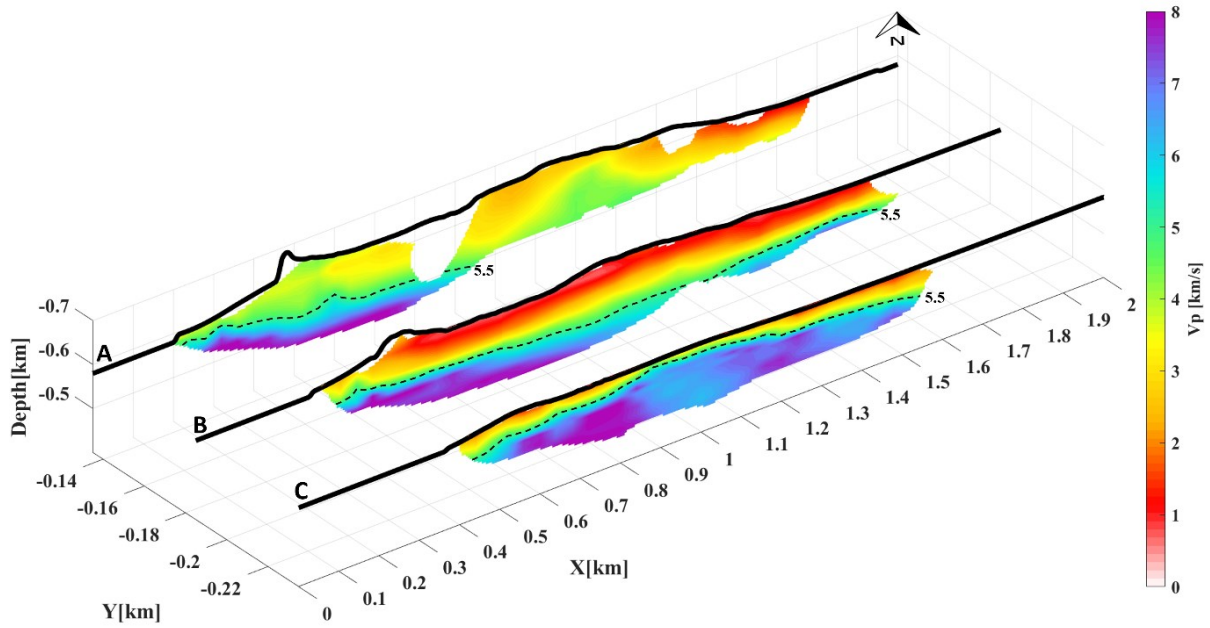


Figure 27: Slices A, B and C from the three-dimensional inversion (see dashed lines in Figure 9). The 5.5 km/s isoline considered as the reference datum is marked with dashed lines. Only areas with hypothetical ray coverage are displayed. Y axis exaggerated 6:1.

6. Reflection seismic processing and imaging

Once the seismic data is acquired, it undergoes seismic processing to eliminate unwanted noise, thereby enhancing the coherency and strength of the seismic reflectors, the primary signal of interest. This typical workflow encompasses processes such as automatic gain control (AGC), bandpass filtering, f-k filtering, and static corrections (elevation, refraction, and residual statics), alongside velocity analysis, trace editing, muting, and deconvolution. Following, the seismic imaging takes place, where seismic traces are sorted into common-midpoint gathers (CMP-sorting), corrected for normal move-out (NMO), and CMP-stacked. The subsequent application of migration geometrically relocates seismic events to their true position, generating a seismic image of the subsurface.

In sedimentary basins, where reflections are typically abundant, the described processing workflow proves effective. This stands in stark contrast to crystalline environments, where impedance contrasts—and consequently, reflectors—are significantly weaker. The minimal reflectivity of the subsurface in hardrock environments poses substantial processing challenges. Without clear seismic reflectors as guides, the effectiveness of various processing steps—such as bandpass filtering, semblance velocity analysis, and the evaluation of residual statics—cannot be assessed. However, significant impedance contrasts are not limited to the boundaries between formations. Features such as open fracture zones and igneous intrusions (e.g., dikes, sills) can create notable impedance contrasts, generating seismic reflections. These reflections offer limited but valuable insights into the effectiveness of the processing techniques. In addition, research in hardrock environments, exemplified by the Scandinavian Caledonides (e.g. Hedin et al., 2016), show that clear reflectors can persist even after metamorphic processes during orogeny. Therefore, the reflectivity in crystalline environments is intricately linked to geological history and lithology.

However, even when the crystalline environments show some reflectivity, seismic processing focused on producing a CMP-stacked image encounters major difficulties. Simon et al. (1996), in their investigation at the DEKORP site, illustrate the CMP-processing limitations. They observe several events in the shot gathers displaying poor coherency, which is not improved upon reorganizing the data into CMP gathers, as depicted in Figure 28. They attribute this behavior to the lack of continuity of the complex steeply-dipping interfaces and velocity heterogeneities that characterize these complex geological environments. Therefore, they bypass CMP-stacking altogether in favor of directly applying Kirchhoff Pre-Stack Depth

Migration (KPSDM), which proves to be an effective strategy for obtaining clearer images of the subsurface in a challenging area. Currently, pre-stack algorithms replaced CMP-stacking as the typical workflow in complex geological settings, especially in crystalline environments.

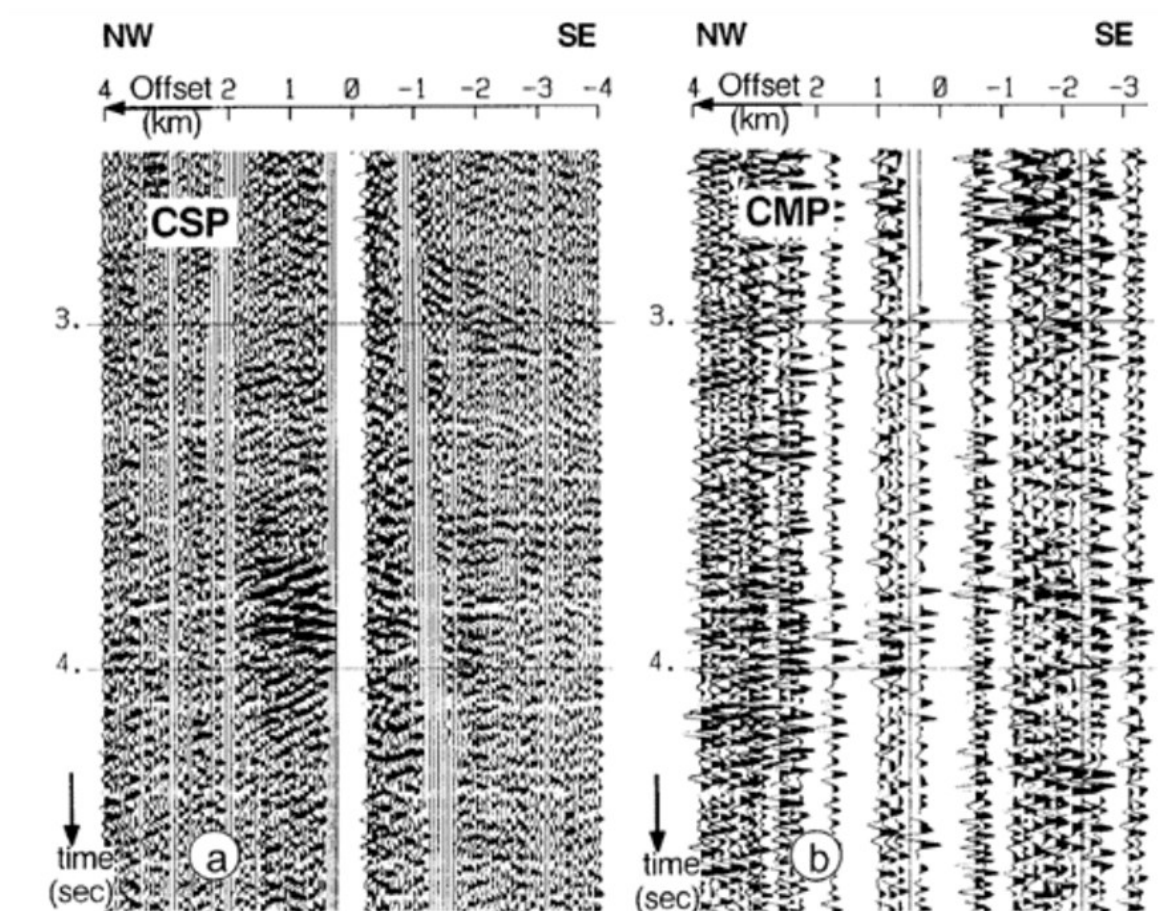


Figure 28: Seismic data examples from the DEKORP pre-site seismic survey. a) Common shot gather with strong events at approximately 3.8 s. b) CMP gather from the same location showing the lack of coherency of the events identified in a). After Simon et al. (1996).

Nevertheless, CMP-stacking cannot be completely discarded. In hardrock seismic exploration, the use of constant velocity stacks (CVS) is common to evaluate the most effective stacking velocity that would significantly enhance the visibility and coherence of seismic events. Crystalline rocks are characterized by a smoothly varying, low-amplitude velocity gradient. Within these high-velocity areas, the move-outs associated with seismic events are typically small (e.g. Eaton et al., 2003). This means that a constant velocity model close to the average velocity expected in the study area will be enough to obtain a relatively good NMO correction,

which will then translate to events stacking coherently. This will give valuable insights into the possible velocities and geological structures that characterize the area.

In this project, a particularly challenging scenario is faced, marked by an almost complete absence of clear seismic reflectors, except for a solitary event described in Subsection 4.3. These circumstances highlight the low reflectivity prevalent in the study area, where discernible events are primarily attributed to the impedance contrasts caused by faults and intrusions, presenting as vertical or near-vertical structures. The forthcoming subchapter will outline the attempts to enhance the signal of these sparse events through a processing workflow that deviates from the typical applied in sedimentary environments. Subsequently, Subsection 6.2 will delve into the imaging method applied to the processed seismic data, aiming to image the subsurface structures despite the challenges presented by the complex geological environment.

6.1. Seismic Processing

The seismic processing is conducted using the VISTA processing software by Schlumberger. Each receiver line is processed individually but applying the same processing workflow.

Initially, a thorough inspection of the shot and receiver gathers is carried out to identify and delete traces adversely affected by incoherent noise. Then, the amplitudes are balanced through spherical divergence correction and subsequent trace normalization. The latter is applied since true-amplitude processing is time-consuming and no amplitude-dependent analysis or process (e.g. Amplitude Variation with Offset (AVO) analysis or seismic inversion) is planned for this study. Subsequently, the air wave is muted. Figure 29 shows examples of four shot gathers after the described processing steps are applied.

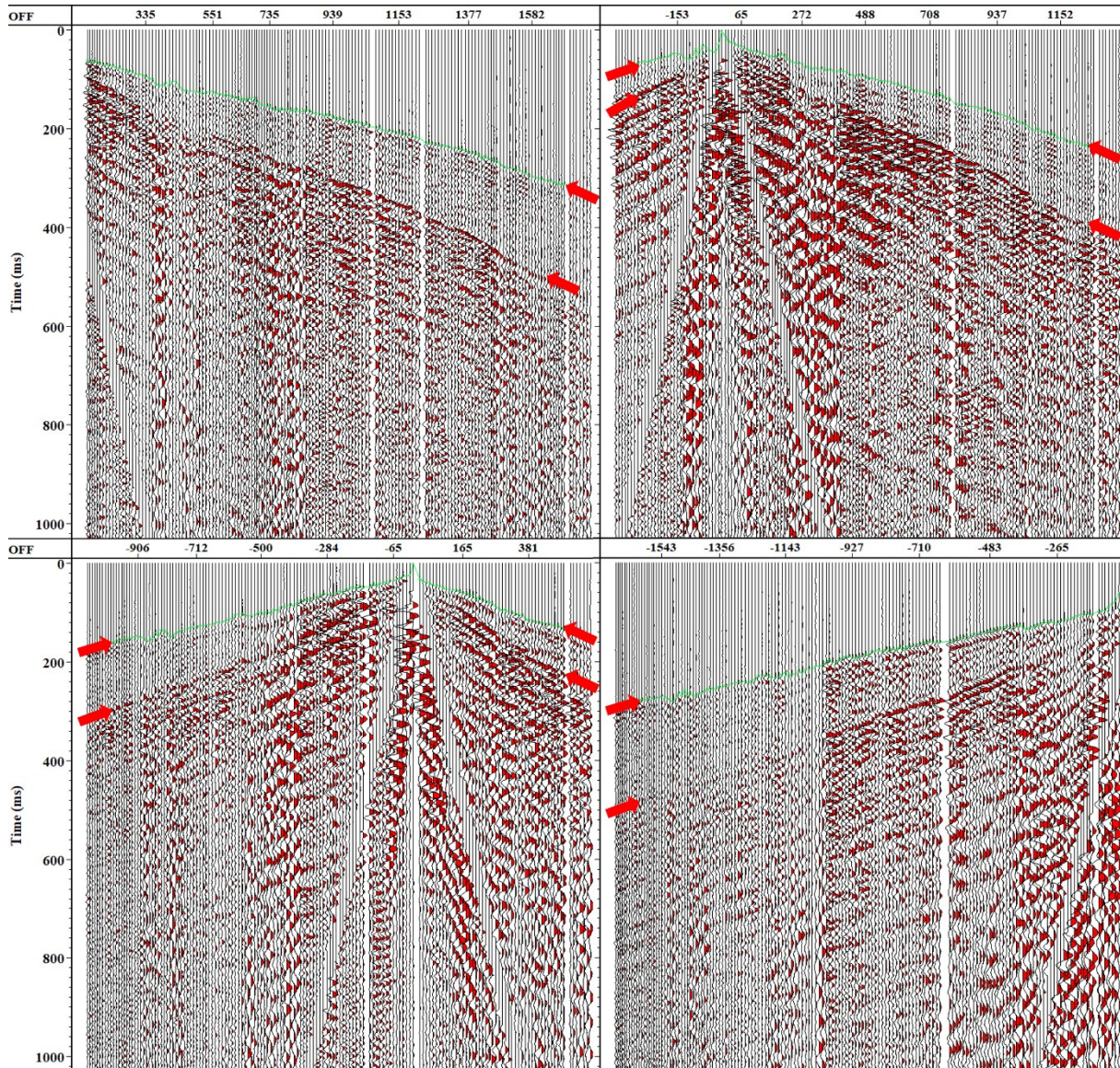


Figure 29: Shot gathers after spherical divergence correction, trace normalization and air wave muting. The green line follows the P-wave first break picks for each shot gather. Red arrows mark the P and S-wave first arrivals. Top row: shot point N° 986(left) and N° 1034 (right). Bottom row: shot point N° 1106 (left) and N° 1166 (right).

The seismic data is characterized by strong amplitudes of P and S-wave first arrivals and their reverberations, necessitating their attenuation to enhance the signal of the reflected refractions and the single reflector (Figure 18). Initially, the application of an f-k filter is contemplated. An f-k filter is mainly used in seismic processing to attenuate coherent linear noise (like ground roll), guided waves and side-scattered energy. After transforming the data from the time-offset domain (t-x) to the frequency-wave number domain (f-k), these events are

separated into different regions depending on their velocities, which separates them from the desired signal and allows for the application of a targeted f-k filter. However, due to the first arrivals not aligning linearly—impacted by significant horizontal velocity variations—the f-k filter applied is not effective in filtering the P and S-wave arrivals (Figure 30). To improve the effectiveness of the f-k filter the P-wave first arrivals are flattened to a datum with a static shift, thus eliminating the effect of the velocity variations. Figure 31 shows how this approach improves the effectiveness of the f-k filter. However, the results are not satisfactory because there are remnants of P and S-wave first arrivals.

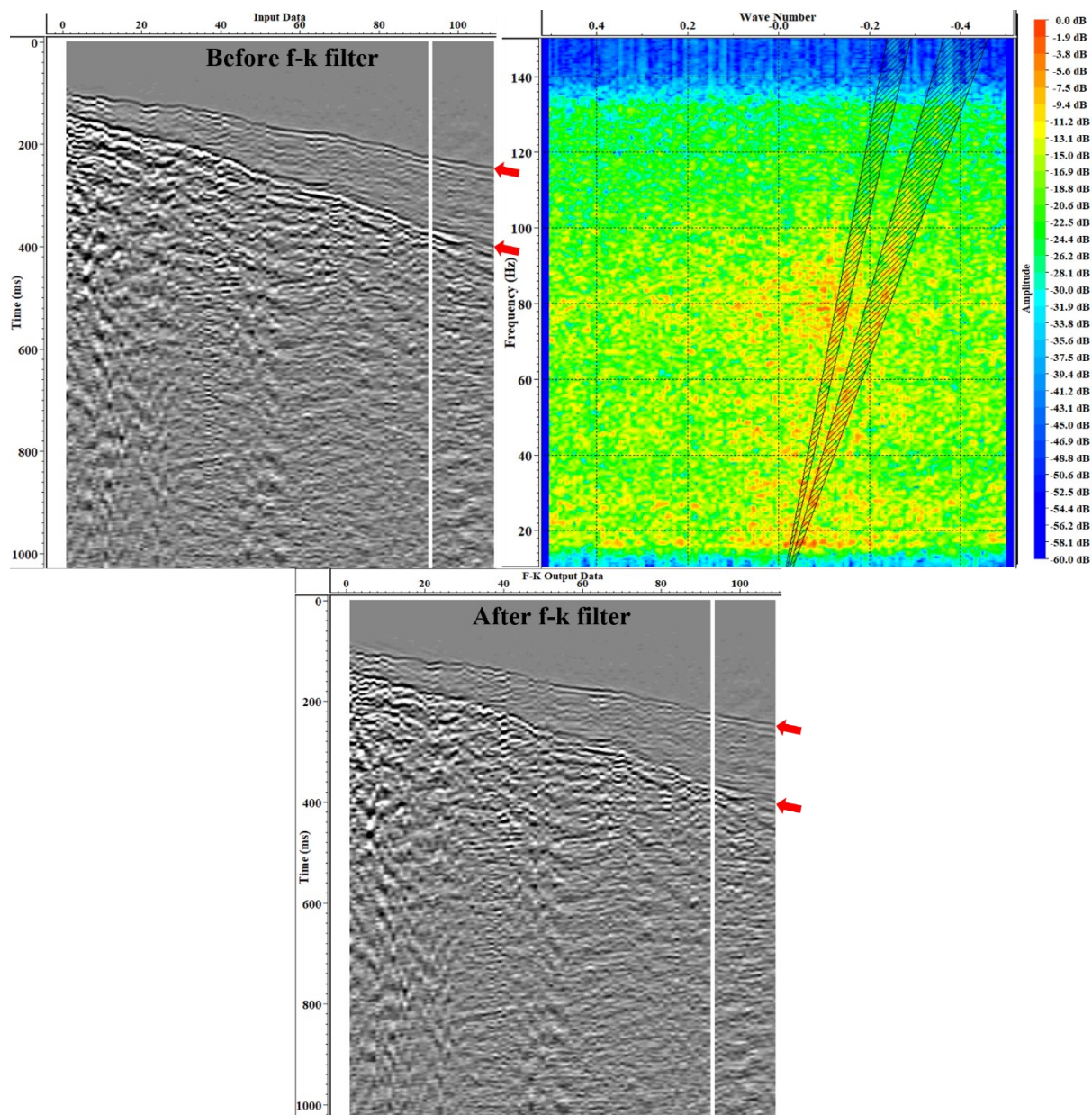


Figure 30: Example of an f - k spectrum analysis for shot gather N° 984 acquired with receiver Line 2 after amplitude balancing and air wave mute. Top-left: Shot gather before the application of the f - k filter. Top-right: f - k spectrum with shaded areas representing the f - k filter to be applied. Bottom: Shot gather after the application of the designed f - k filter. The red arrows mark the P and S-wave first arrivals.

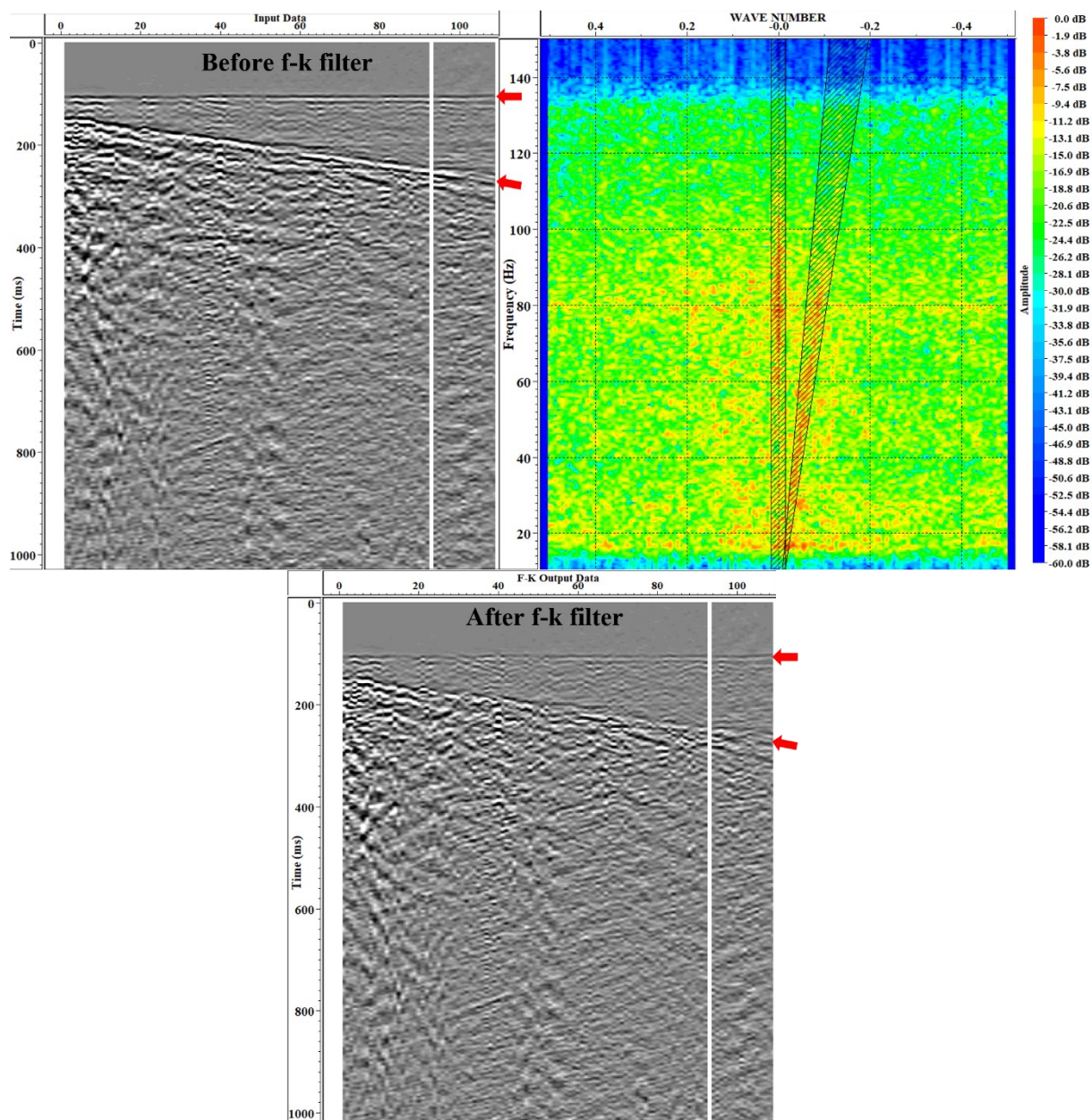


Figure 31: Example of an *f-k* spectrum analysis for shot gather N° 984 acquired with receiver Line 2 after amplitude balancing, air wave mute and P-wave flattening. Top-left: Shot gather before the application of the *f-k* filter. Top-right: *f-k* spectrum with shaded areas representing the *f-k* filter to be applied. Botom: Shot gather after the application of the designed *f-k* filter. The red arrows mark the P and S-wave first arrivals.

An alpha-trimmed median filter is the most effective approach for filtering the first arrivals. Median filters can be used to attenuate coherent wavefields and are typically used during VSP data processing to attenuate the downgoing wavefield. The core principle of a median filter is that for each point of a series of numbers, its value is replaced with the median of the surrounding values. The median value is obtained after sorting the series of numbers into ascending order inside a defined window, which moves along the points of interest across the entire dataset. An alpha-trimmed median filter goes one step further, removing (trimming) a portion of the data from both ends of the window and calculating the mean of the remaining values (Bednar & Watt, 1984). Its application to filter the P-wave first arrivals in the seismic data acquired for this project involves a series of steps:

- 1- The P-wave first arrivals are flattened to a datum, using the first-arrival picks as a guide (Figure 32b).
- 2- An alpha-trimmed median filter is obtained using a window of 13 traces and 33% rejection (Figure 32c).
- 3- The calculated filter is removed from the flattened data to filter the first arrivals (Figure 32d).
- 4- The flattening is removed to restore the seismic traces to their original time (Figure 32e).

The standard approach in seismic processing is to mute the P-wave first arrivals. This is not considered for this data since they are used as a guide for the alpha-trimmed median filter to filter their reverberations.

The first S-wave arrivals are computed from the P-arrival times for a Poisson body ($V_p/V_s = \sqrt{3}$), and manually adjusted. Then, the same steps are applied to remove the first arriving S-wave (Figure 33).

Following the application of the alpha-trimmed median filter, a band-pass filter is applied to subdue unwanted low-frequency signal and possible noise at higher frequencies than the ones excited by the Vibroseis (140 Hz). Various low-cut frequencies are tested from which the configuration 35-40-140-150 Hz give the best results (Figure 34). Frequencies below 35 Hz are excited by the Vibroseis source, but do not provide useful resolution considering the resulting wavelength for velocities of 6 to 8 km/s. Then, a top mute is applied above the P-wave first arrivals.

Figure 35 shows an example of the processed data. It contains remnant S-wave energy that may produce artifacts during the imaging process. Unfortunately, this remnant energy cannot be filtered without affecting the reflected refractions visible on the shot gathers after the signal processing (Figure 36).

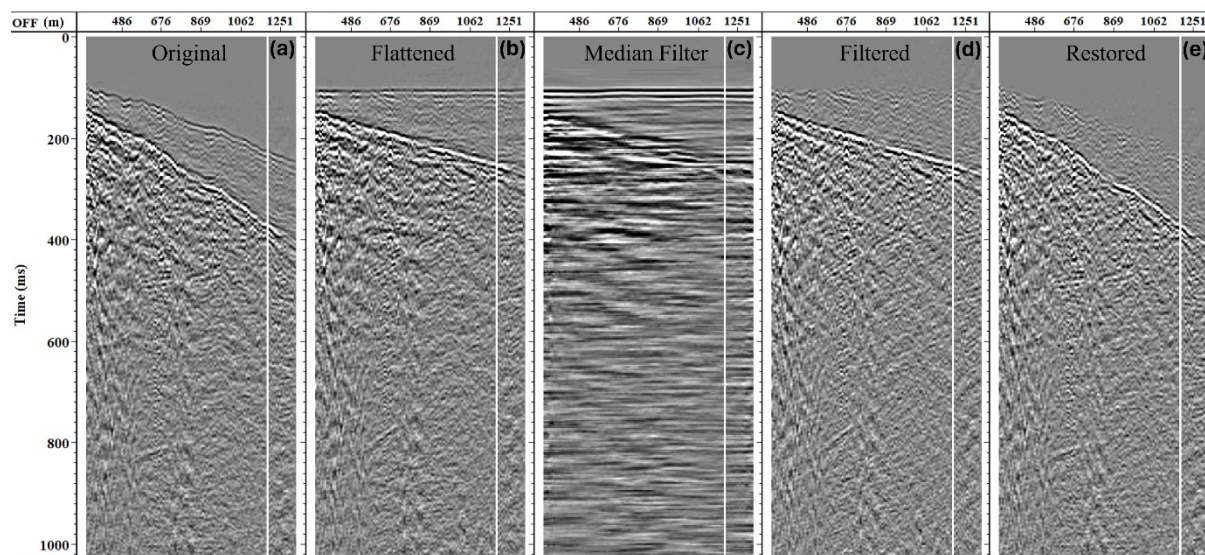


Figure 32: Example of the median filter applied to shot gather N° 984 to reduce the P-wave first arrivals.

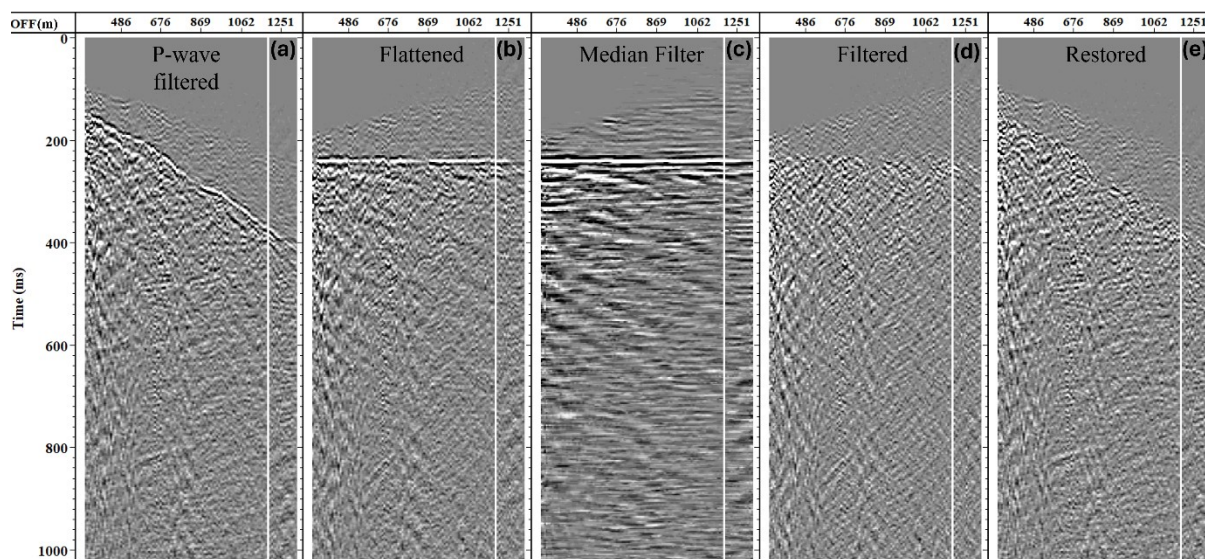


Figure 33: Example of the median filter applied to shot gather N° 984 to reduce the S-wave first arrivals. Panel (a) is the output from the P-wave first arrival filtering depicted in Figure 33e.

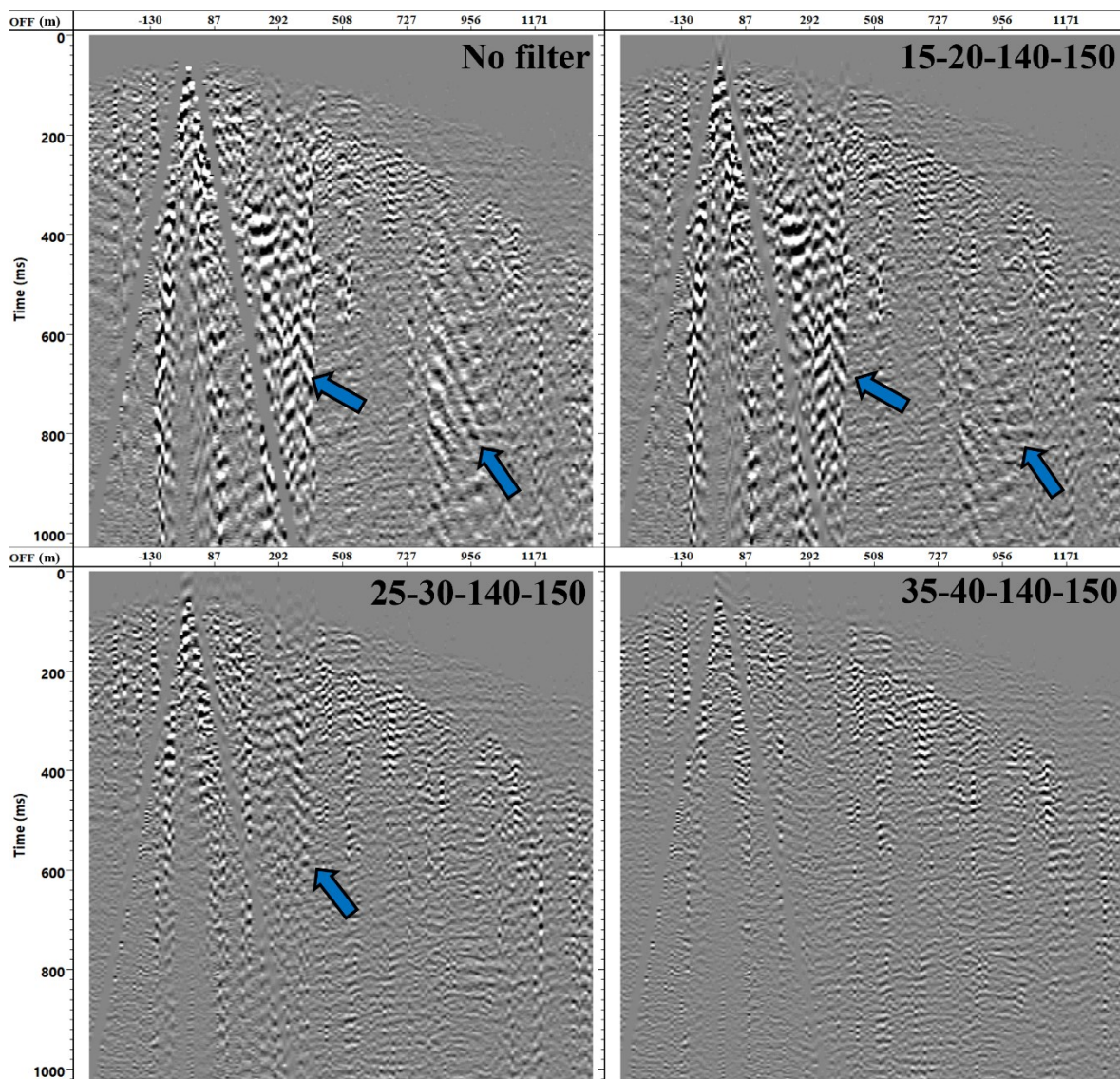


Figure 34: Band-pass filter test. The top-left panel shows the shot gather N°1032 after filtering of the S-wave first arrivals with no band pass filter applied. Blue arrows mark the unwanted low-frequency signal. The remaining panels show the results after applying different band-pass filters. The corner frequencies for every band-pass filter (in Hz) are shown at the top-right corner of each panel.

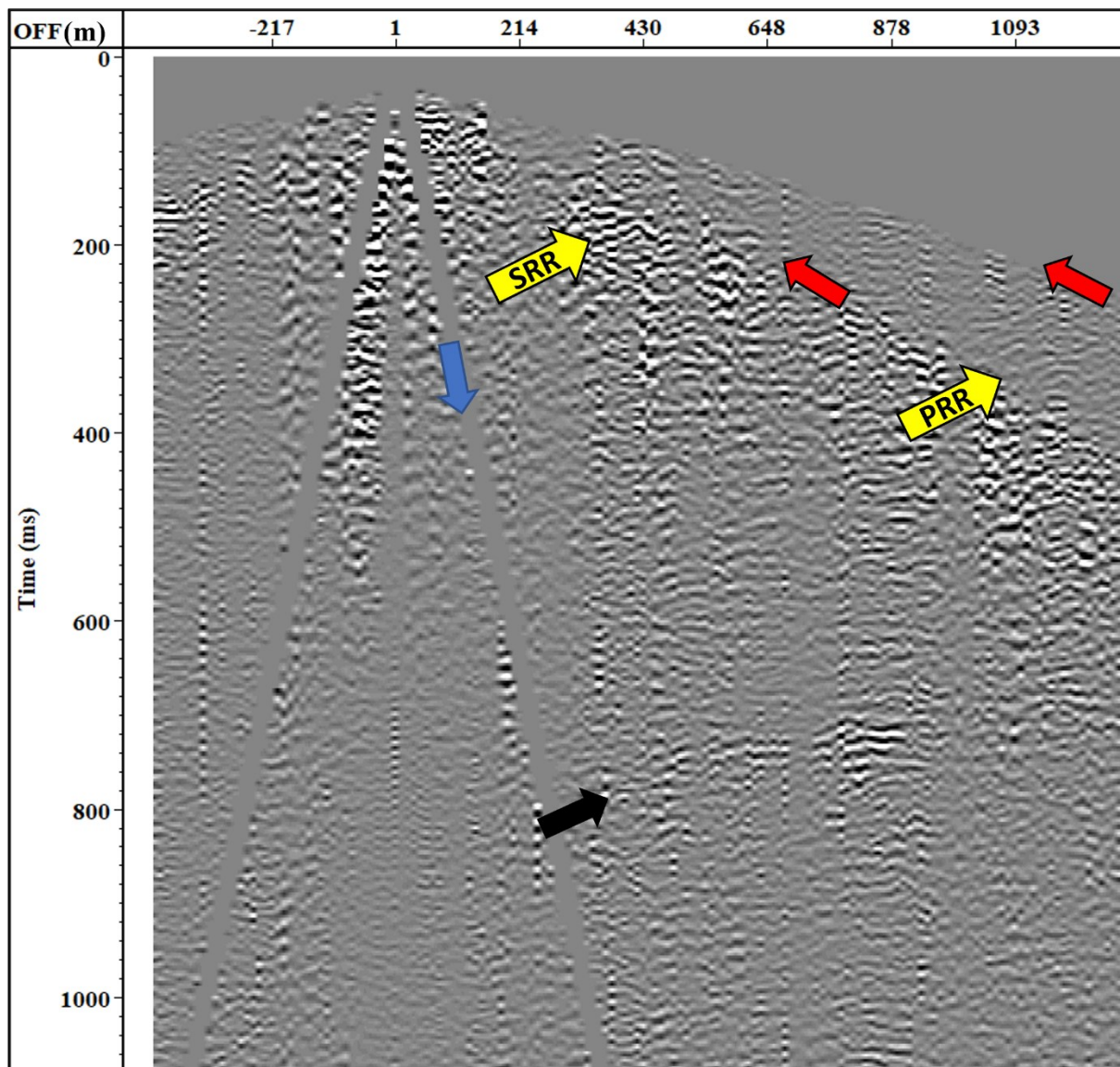


Figure 35: Shot gather N° 1040 after direct P- and S-wave removal and band-pass filter. Red arrows mark the removed direct P- and S-wave arrivals. P and S-wave reflected refractions are marked as yellow arrows. The blue arrow marks the removed air wave. The black arrow shows the reflector at ca. 700 ms. SRR: S-wave Reflected Refraction. PRR: P-wave Reflected Refraction.

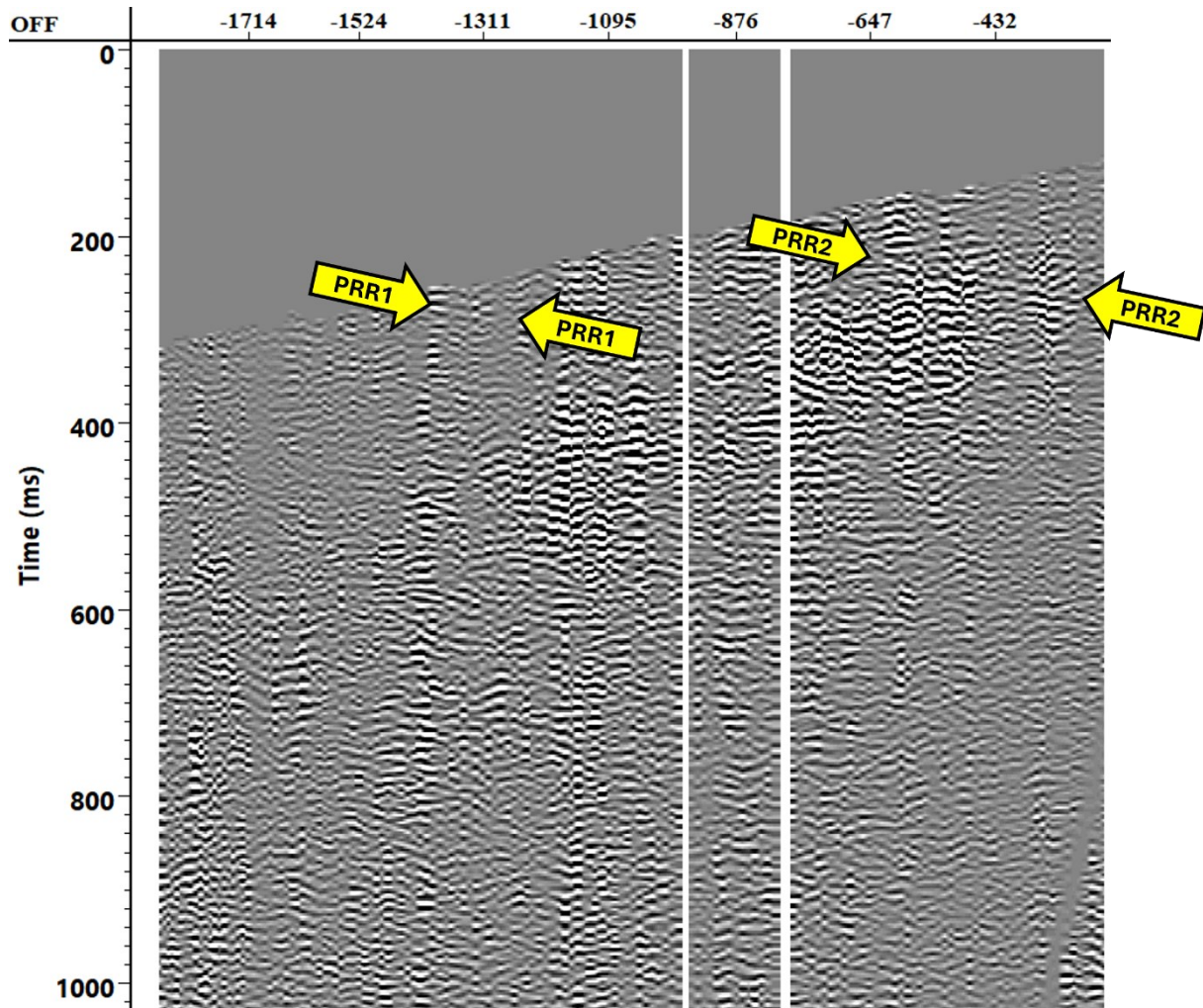


Figure 36: Example of reflected refractions in shot gather N° 1182 after processing. Two P-wave reflected refractors are marked with yellow arrows. PRR1: P-wave Reflected Refraction 1. PRR2: P-wave Reflected Refraction 2. Offset in meters.

Refraction static corrections are derived from the 3D tomography velocity model (Figure 27), using the 5.5 km/s isoline as a floating datum. This isoline is chosen for its distinction as the deepest continuous feature across the image, serving as a good reference for the statics calculations. Static correction times are calculated as the difference in vertical traveltimes between the topography and the selected datum. Subsequently, these correction times are applied to adjust the position of each receiver and source, effectively shifting them from their initial topographic locations to align with the datum.

The final step in the processing workflow is a 3D Kirchhoff Pre-Stack Depth Migration (KPSDM) from topography. For this purpose, a homogeneous layer of 7 km/s is used to replace

the velocities between the topography and the datum. Then, static correction times are recalculated to restore the receivers and sources to their topographic positions. Figure 37 shows an example of the total refraction statics calculated for Slice C in the 3D tomography (see Figure 27). Notably, the replacement velocity of 7 km/s is inconsistent with the chosen isoline of 5.5 km/s. To assess the impact of this inconsistency, the refraction statics to a 7 km/s isoline as a floating datum are calculated for those parts of the model where this isoline is observed. The difference between these consistent refraction statics and the statics with the 5.5 km/s datum is generally below 1 ms and is therefore negligible considering the dominant signal period of 14 ms.

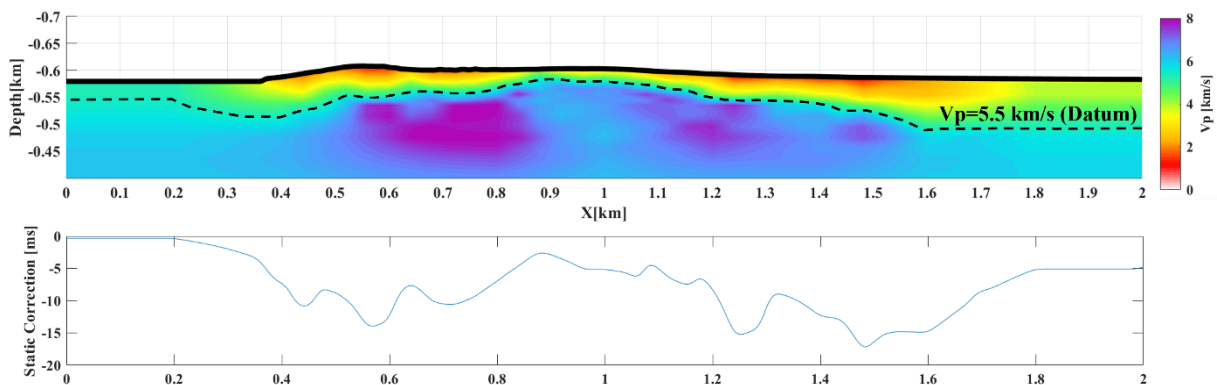


Figure 37: Slice C from the 3D tomography from Figure 27 without ray coverage (top) and calculated total refraction static correction times (bottom).

Once the processing stage is finished, the seismic data from Line 1 is sorted into CMP gathers and an attempt is made to apply a semblance velocity analysis. The objective is to demonstrate that this analysis will not be effective for this seismic data. Figure 38 shows an example for a particular CMP gather where the semblance analysis does not show any coherent event. Spots of high semblance values cannot be correlated to any event in the CMP gather and are usually not higher than 0.1, which shows that just by chance a few traces stacked coherently. This behavior is repeated for every CMP gather analyzed. Therefore, it is confirmed that the generation of a velocity model through the typical semblance velocity analysis workflow is not possible.

The limitations observed in revealing seismic features through the typical CMP processing approach show the necessity of a more sophisticated imaging technique capable of accurately

delineating steeply dipping geological structures within the subsurface. The Kirchhoff Pre-Stack Depth Migration (KPSDM) offers the potential to resolve the complex imaging challenges posed by this crystalline environment.

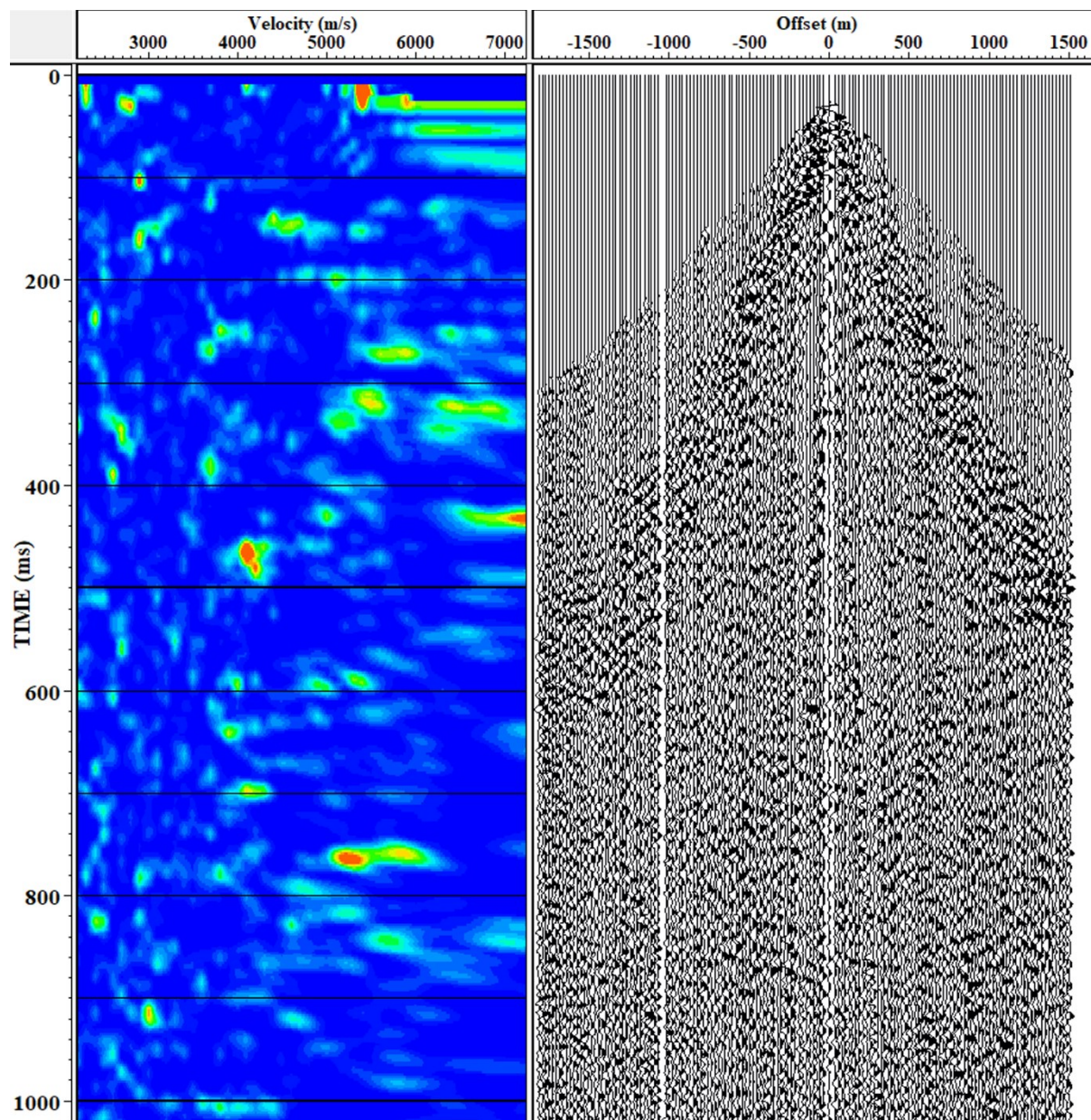


Figure 38: Semblance velocity analysis applied to a CMP gather from Line 1. The left panel shows the semblance values for the CMP gather shown to the right. Semblance values are less than 0.1 and cannot be correlated to any event in the CMP gather.

6.2. Seismic imaging

Once the processing workflow is applied to each receiver line individually, the seismic data from all the lines is merged. Then, considering the complex geological structures expected in the area and to take advantage of the seismic data from all the lines to better position the seismic events, 3D KPSDM is performed. The code used for this process is the code 'kirch_2B' that employs the same eikonal solver as SIMULR16 after Hole & Zelt (1995) to compute the traveltimes.

An essential input for the migration process is a velocity model. However, in the absence of a suitable velocity model obtained through standard processing tools, a different approach is necessary. The following subsections will describe different tests performed to define an appropriate velocity model.

6.2.1. Constant Velocity Stacks

To have an initial idea of the geological structure and velocities that characterize the subsurface, a CVS analysis is attempted. The objective is to determine the optimal stacking velocity that will significantly enhance the visibility and coherence of possible seismic events that are not visible in both shot and CMP gathers. CVS in a range of 6 to 8 km/s with a 0.2 km/s interval are performed since this range of velocities is observed in the tomographic results. The goal is to pinpoint features that will consistently exhibit coherence across varying velocities, thereby indicating true geological features. However, while certain coherent features emerge within the CVS analysis, their presence is intrinsically linked to the specific constant velocity applied. These features disappear upon adjustment to a subsequent velocity setting (Figure 39). Therefore, it is not possible to identify a persistent coherent feature throughout the CVS panels that could represent a significant geological structure.

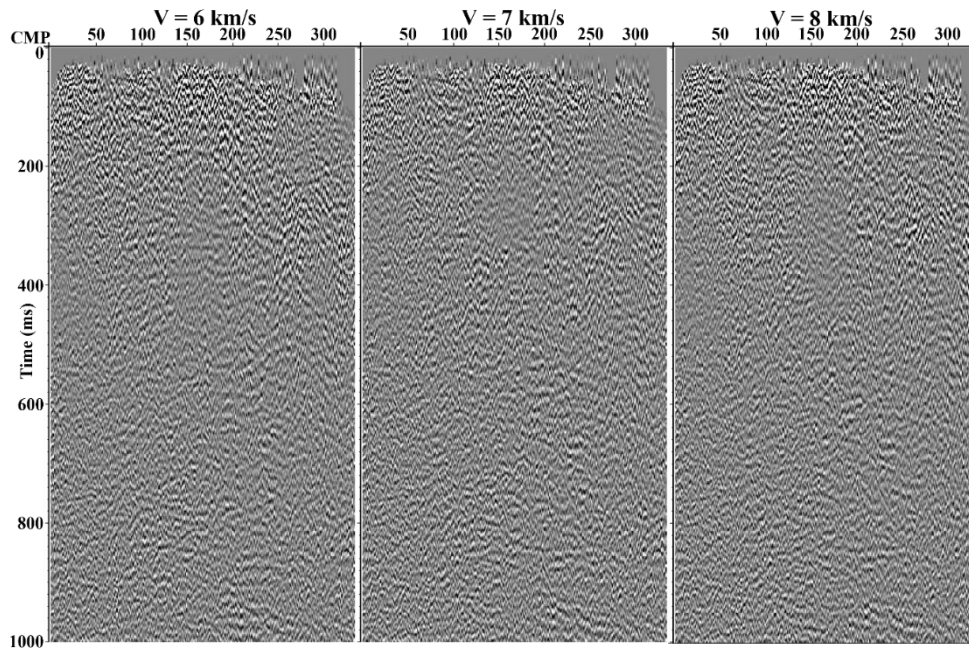


Figure 39: Constant velocity panels for three velocities. Left: 6 km/s; center: 7 km/s; right: 8 km/s.

6.2.2. Constant velocity models

Similar to the CVS approach described in Subsubsection 6.2.1, constant velocity migrations (CVM) are performed considering velocities within the same range. Constant velocity cubes are generated with a 200 m/s interval, comprising a total of 10 constant velocity models. For time purposes, the migration algorithm is applied solely to Line 1. Nevertheless, a 3D migration is performed to account for its crookedness. The primary goal remains to pinpoint seismic features that manifest consistently across multiple constant velocity panels.

For this test, the seismic data are processed without the application of refraction statics. The replacement velocity used for restoring the receivers and sources to their topographic positions would need to change for every new velocity model considered in the test. This would mean the calculation of 10 different refraction static corrections, a time-consuming process. While the application of refraction statics is crucial for mitigating the distortive effects of low-velocity layers, doing so in this context would compromise the comparability of results. Different static corrections would yield varied datasets, meaning that coherent features identified at one velocity might not be discernible at another, but this discrepancy would be attributed to the differences in the datasets rather than to their intrinsic seismic characteristics.

Upon analysis of the CVM results shown in Figure 40 and Figure 41, three distinct features can be distinguished across the panels, suggesting that they are likely generated by true geological features. The position of the event marked with a red arrow can be correlated with the West boundary of the BP identified on surface geological maps. Conversely, the events marked with blue arrows are positioned inside the BP, but there is no evidence of any fault or geological feature mapped at the surface to which they could be correlated.

Notably, the coherence of these events begins to diminish at velocities exceeding 7400 m/s. This observation establishes an effective upper limit for velocity considerations in the analysis. The presence of these features, particularly when contrasted with the outcomes of the CVS tests, are promising. It demonstrates that a CVM analysis can unveil coherent events, potentially indicative of true geological structures beneath the surface.

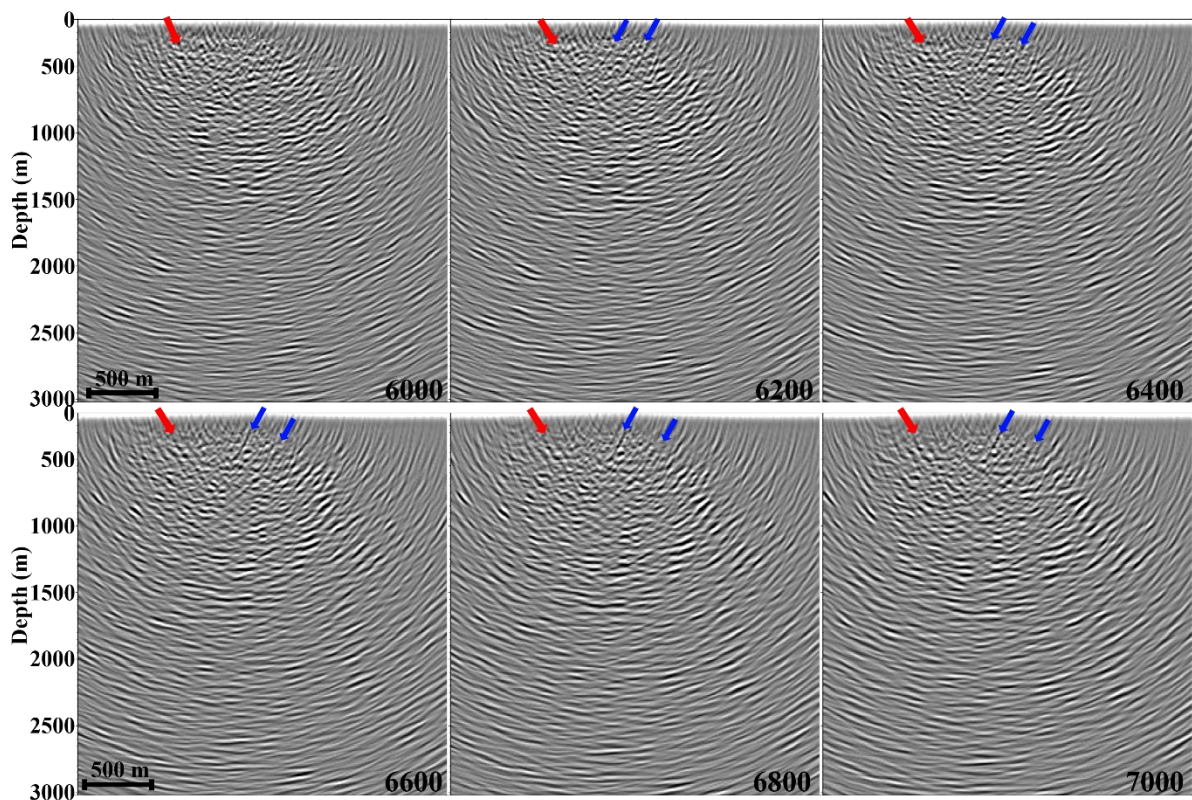


Figure 40: Slices from the 3D KPSDM applied using Line 1 data and various constant velocity models. The velocity (in m/s) used for each panel is shown in the bottom right corner. Arrows depict consistent features that can be interpreted throughout the panels. The depth represents the depth of the velocity model used. The zero reference is 700 m above sea level.

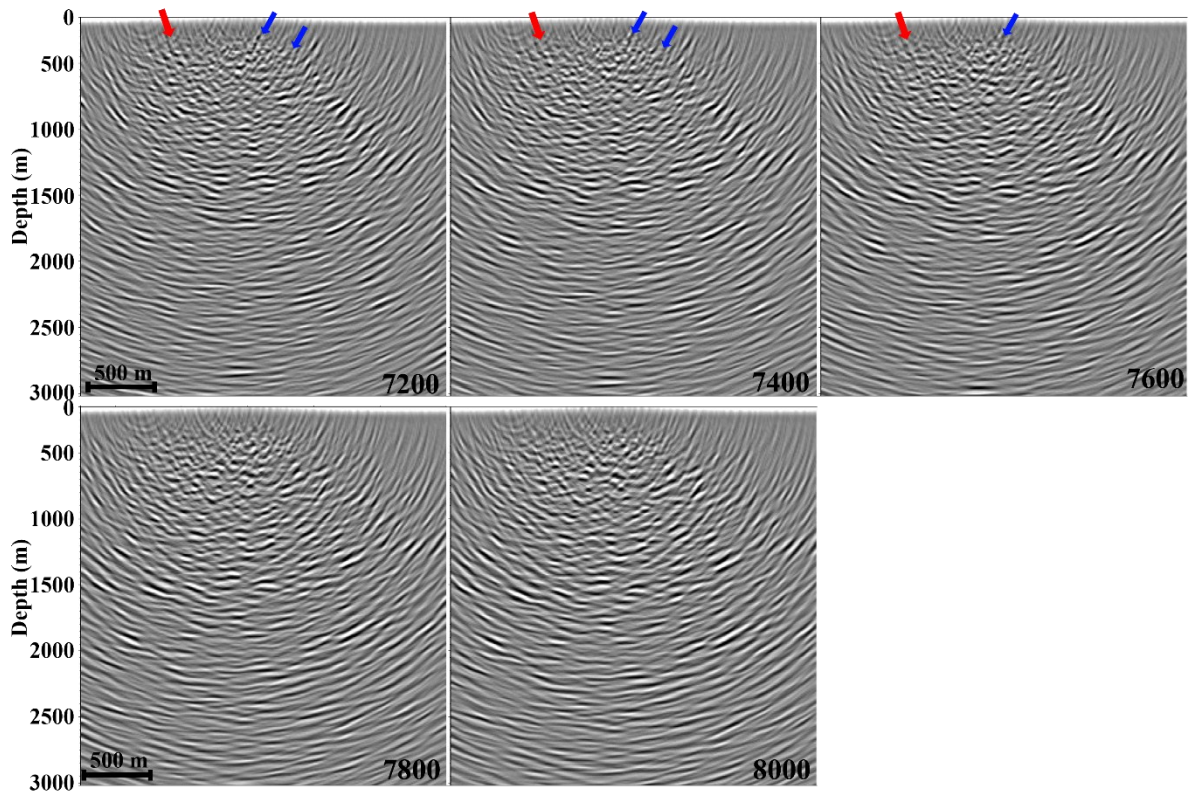


Figure 41: Slices from the 3D KPSDM applied using Line 1 data and various constant velocity models. The velocity (in m/s) used for each panel is shown in the bottom right corner. Arrows depict consistent features that can be interpreted throughout the panels. The depth represents the depth of the velocity model used. The zero reference is 700 m above sea level.

6.2.3. Conceptual velocity models

The emplacement of the BP, particularly its relationship with the IGB, emerges as a significant area of inquiry, as detailed in Subsection 1.2. The main debate revolves around two primary models that attempt to explain this relationship. The first model suggests the BP as an isolated lens of peridotite, whereas the second suggests that the BP is a continuous body that extends into and is physically connected with the IGB.

To explore these two hypotheses, two conceptual velocity models are generated, expressing the distinct interpretations of the BP and the IGB's structures (Figure 42). These models are designed to reflect the potential variations in seismic velocities that these different geological configurations would exhibit, using available geophysical and geological information to define the seismic velocities and approximate subsurface geological structure. A background velocity

gradient is built with the velocity at the near-surface starting at 5000 m/s, followed by 6000 m/s and 6500 m/s subsequently. Since a velocity of 5000 m/s is considered for the near surface, for this conceptual model tests only, the refraction static corrections are recalculated considering a floating datum that follows the 5000 m/s isoline from the 3D tomography. Then, velocities above the floating datum are replaced by a velocity of 5000 m/s to calculate the total refraction static corrections. For the BP, a velocity of 7 km/s is considered representative, as explained in Subsection 5.1. The IGB itself is assigned a velocity of 7.5 km/s, attributed to its composition of similar peridotite material but situated at greater depths, thereby subjected to higher pressures.

The depth estimation for the IGB is obtained from the study conducted by Scarponi et al. (2021). The position of the nodes that define the top of the IGB in a cross section of their 3D density model are used to obtain a more precise representation of the body. Conversely, the depth for the BP, under the scenario where it is considered detached from the IGB, is subjectively defined. Unfortunately, geophysical studies about its depth are non-existent, and the only reference available is a model generated by Quick et al. (1995) where they estimate its depth based on surface geological interpretations. The final shape of the peridotite body is defined as a lens with an irregular shape, approximately 800 m wide (based on the maximum width of the BP in the geological map from Quick et al. (2003)) and 900 m height. Both models are built in 2D and later extrapolated in a regular grid to generate a 3D velocity cube.

Before their application for migration, these conceptual models undergo a smoothing process, using a smoothing window with a Gaussian kernel. In addition, this window increases its size with depth based on the definition of the Fresnel's zone. This method is applied to obtain velocity models that would mimic those derived from a refraction tomography, making them more realistic (Figure 43). Then, the velocity models are cropped to migrate the data using only the area of interest (Figure 43, black-dashed boxes).

The results of the 3D KPSDM using both models can be seen in Figure 44. Upon comparative analysis, discernible differences appear from approximately 1000 m depth downwards. The only difference is that the features after 1000 m are mapped deeper in the attached case. From 1000 m depth upwards, both images are identical.

While the seismic images generated using these velocity models are interpretable, it is concluded that they should not be adopted as definitive models. The primary concern arises from the potential bias introduced by imposing a velocity model with predefined geological

structures. This approach risks skewing the results towards the expected outcomes, thereby undermining the objectivity of the interpretation process. Consequently, any interpretation suggesting the presence of a peridotite lens based on these models could be subject to scrutiny. Reviewers may argue that the interpretation is influenced more by the predefined geological structures set by the velocity model rather than by an unbiased analysis of the seismic data. Therefore, it is crucial to consider alternative models that allow for a more impartial interpretation of the subsurface features.

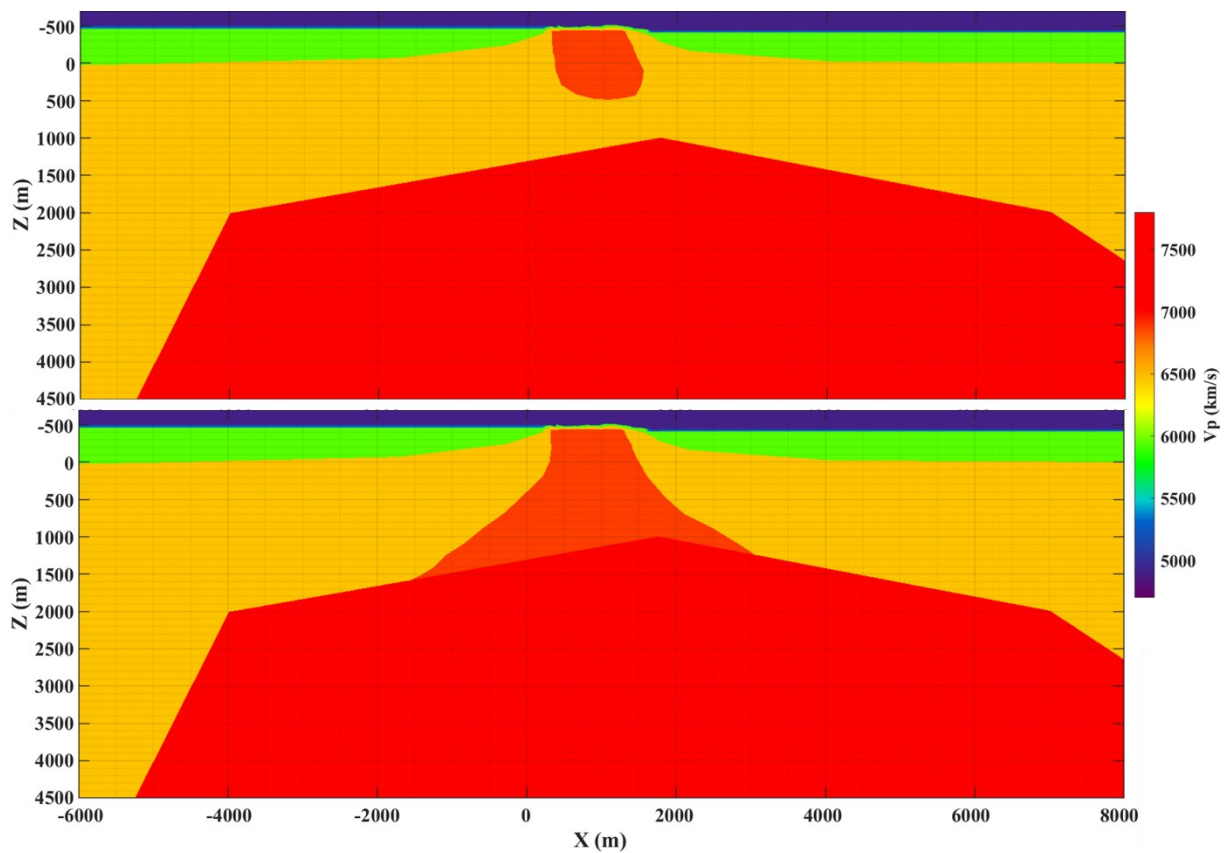


Figure 42: Conceptual models. Top: model considering a lens-like shaped peridotite body. Bottom: model considering an attached peridotite body to the IGB.

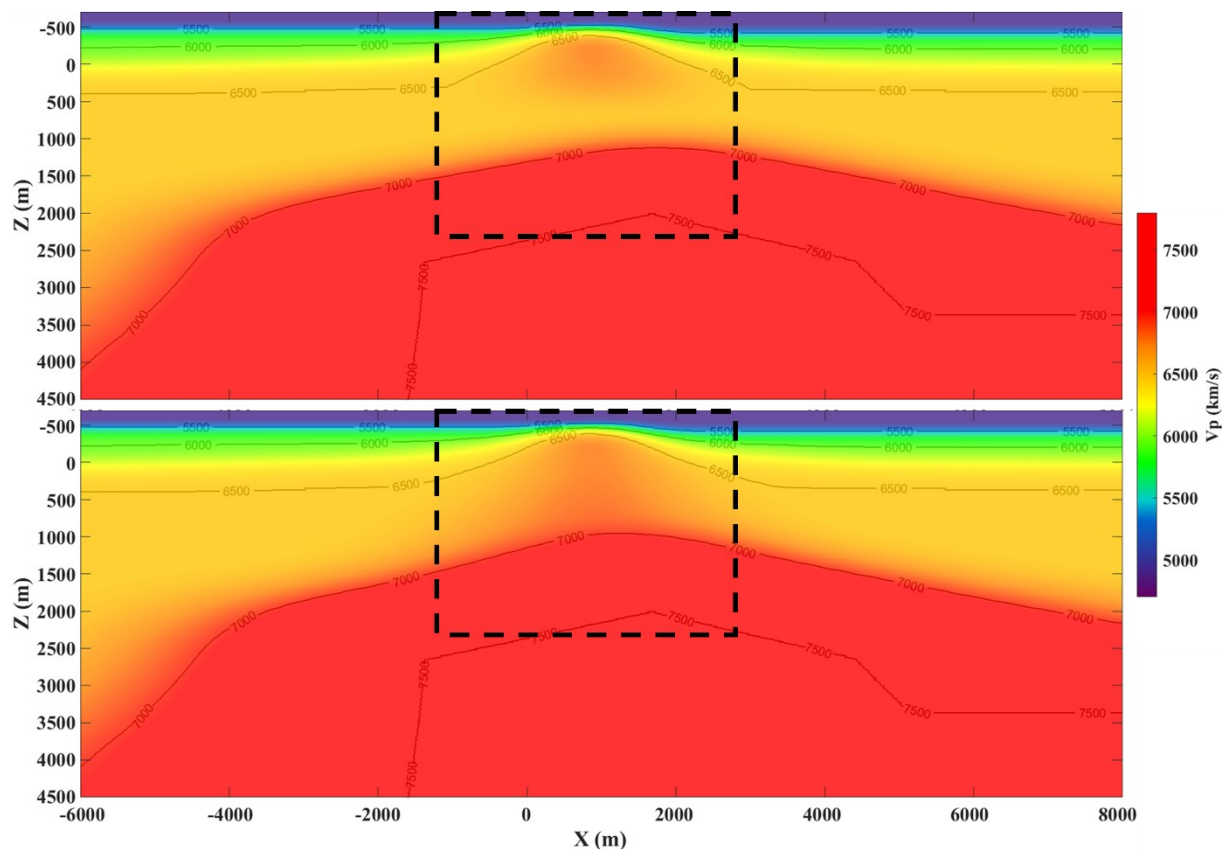


Figure 43: Conceptual models after smoothing window. Top: model considering a lens-like shaped peridotite body. Bottom: model considering an attached peridotite body to the IGB. The black-dashed squares mark the extent of the models that were cropped and used later for the 3D KPSDM. Velocity isolines are plotted as black-thin lines with their respective velocity value.

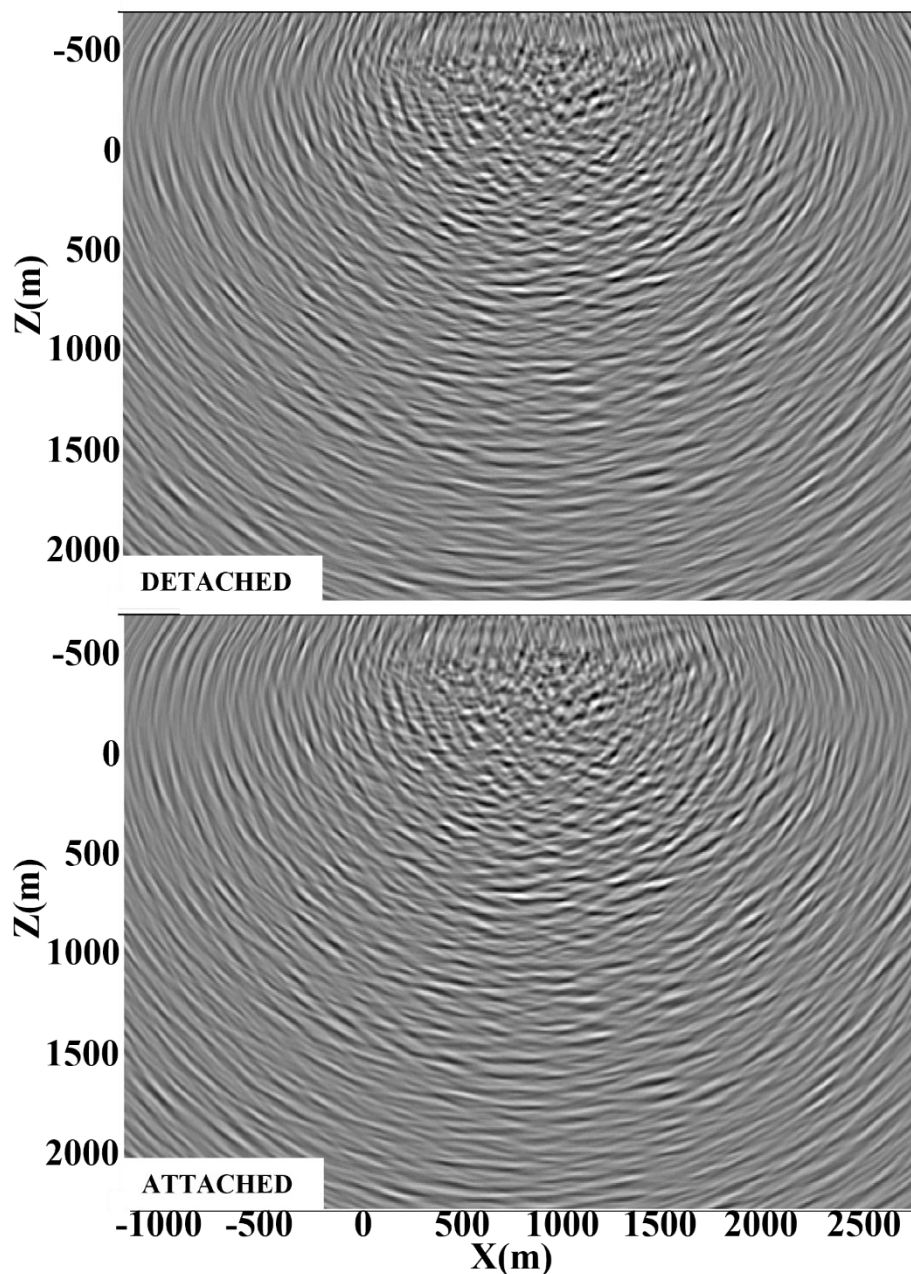


Figure 44: Slices from the 3D KPSDM after migration of Line 1 using the detached (top) and attached (bottom) velocity models shown in Figure 43.

6.2.4. SEIZE velocity model

As explained in Subsection 1.3, Ryberg et al. (2023) obtained a 3D velocity model derived from the data acquired during the SIEZE seismic survey. The authors kindly provided the data of their velocity model for this study, which is then cropped to the area of interest and used as a 3D velocity model for the migration process (Figure 45). This velocity model has a relatively

lower resolution but a depth of ca. 2 km, which is appropriate for this data. Figure 45 shows the results after the application of the 3D KPSDM. The resulting image is rather unfocused and does not allow for a clear interpretation of a possible geological structure. In addition, their results give velocities that are rather low compared to what is obtained by this study (see Section 8 for a discussion on this matter).

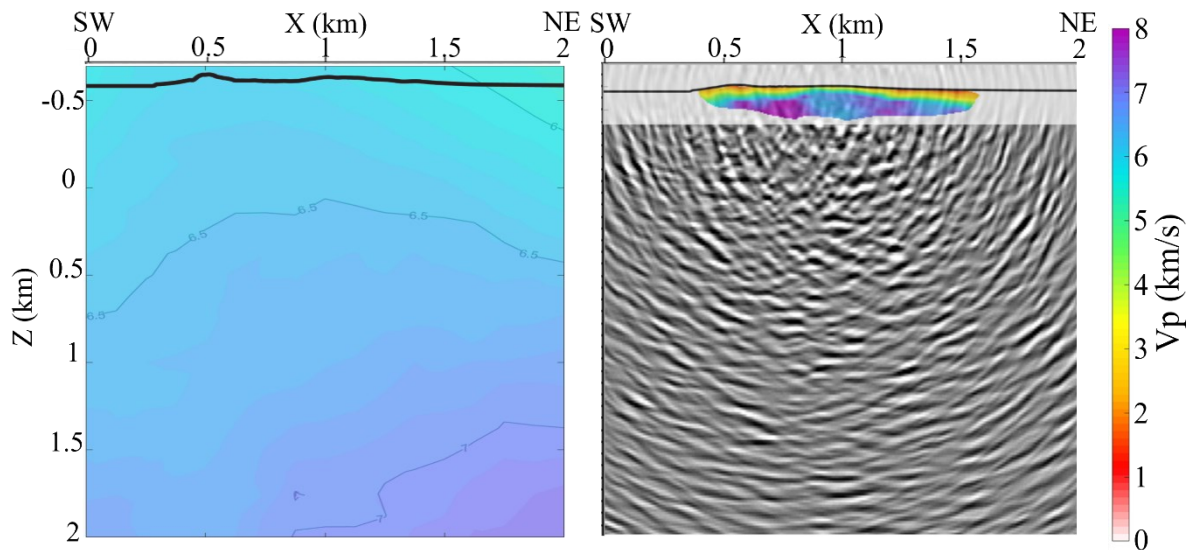


Figure 45: To the left, a slice from the 3D velocity model cropped from Ryberg et al. (2023). The Black-thick line represents the topography. To the right, a slice from the the 3D KPSDM of lines 1, 2 and 3 using the cropped velocity model. Overlaid on the migrated image is Slice C from the three-dimensional inversion (see Figure 27).

6.2.5. Final velocity model

The final velocity model chosen is a constant velocity of 7000 m/s. This constant velocity model is significantly faster than the model of Ryberg et al. (2023) but corresponds with the mean velocity of the peridotite body (Section 5.1). In addition, the constant velocity tests (Subsubsection 6.2.2) show that at 7000 m/s the reflectors within the peridotite body are better focused, particularly highlighting the west boundary of the BP. It is accepted that the imaging of reflectors outside of the peridotite body might be degraded, and that only reflectors dipping towards the center of the profile may be directly imaged, a problem inherent to the survey's geometry. Figure 46 displays a section through the migrated 3D cube roughly along Line 1. To

save computing time, the migration is limited to 2 km below surface and 2 km laterally. To image the reflector at 700 ms (Figure 35), a separate migration is performed in a larger volume. However, only the eight shot points and the receivers where this reflector is visible are used for this migration. The small number of traces used, and their small lateral extent, produce artifacts in the image recognizable as smiles. To reduce these artifacts, an amplitude weighting factor after Tillmanns & Gebrande (1999) is implemented into the KPSDM code that uses the slowness in the data domain to estimate the emergence angle of the wavefront and focus the amplitudes in that direction. Figure 48 shows a subset of the result.

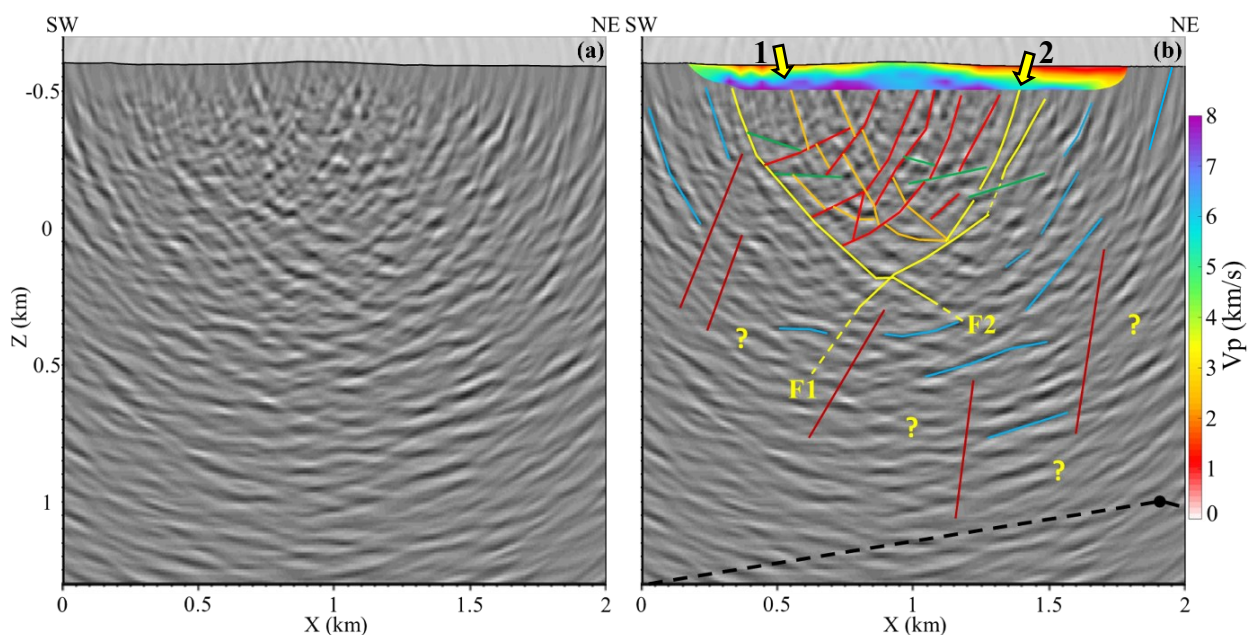


Figure 46: a) Migrated image. b) Annotated migrated image. Image (b) is overlaid with the 2.5D tomography (see Figure 25(b)). The dashed-dotted line and dot mark the approximate position of the top of the IGB proposed by Scarponi et al. (2020) (with ± 1 km uncertainty). Yellow question marks are positioned in areas where further interpretation is not possible. Yellow lines: main faults F1 and F2. Blue lines: reflectors outside the area delimited by faults F1 and F2. Red lines: SW dipping faults. Orange lines: NE dipping faults. Green lines: sub-horizontal faults. Dark red lines: Inferred structures not directly imaged. The two yellow arrows numbered as 1 and 2 mark the position where the P-wave reflected refractions from Figure 36 are imaged. Arrow N^o 1 represents PRR1. Arrow N^o 2 represents PRR2. The position of this migrated cross-section is depicted by the red-dashed line labeled as M in Figure 49.

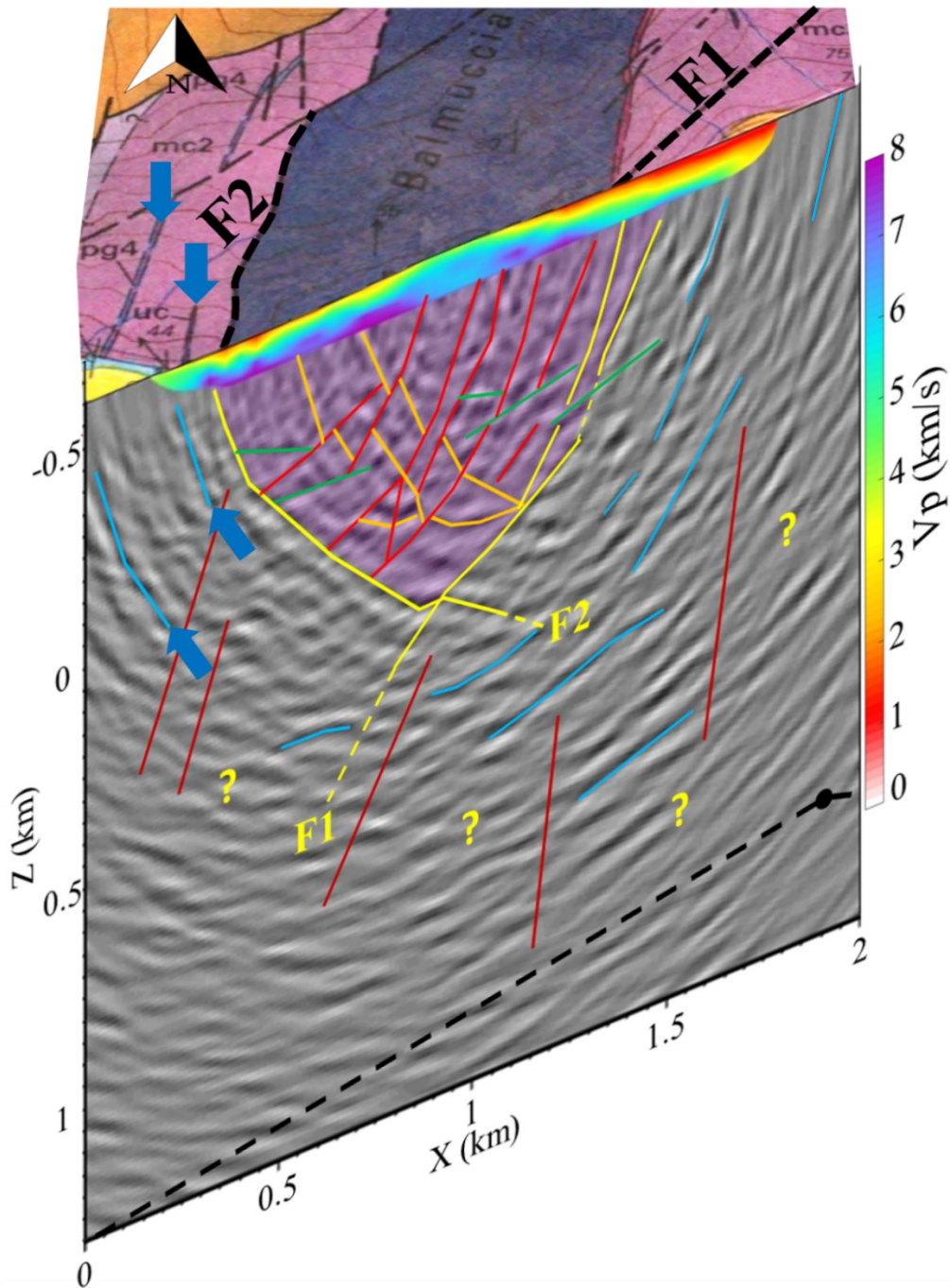


Figure 47: Interpreted perspective image of the migrated results, overlaid with the 2.5D tomography (see Figure 25(b)). The geological map from Quick et al. (2003) is presented as an aid to interpretation. Arrows mark evident correlation between features interpreted in the migrated image and those identified in the geological map. Shaded in violet is the extent of the peridotite body interpreted in this study. The dashed-dotted line and dot mark the approximate (± 1 km) position of the top of the IGB proposed by Scarponi et al. (2020). Yellow question marks are positioned in areas where further interpretation is not possible based on our results. Fault/fracture and reflector colors as in Figure 46.

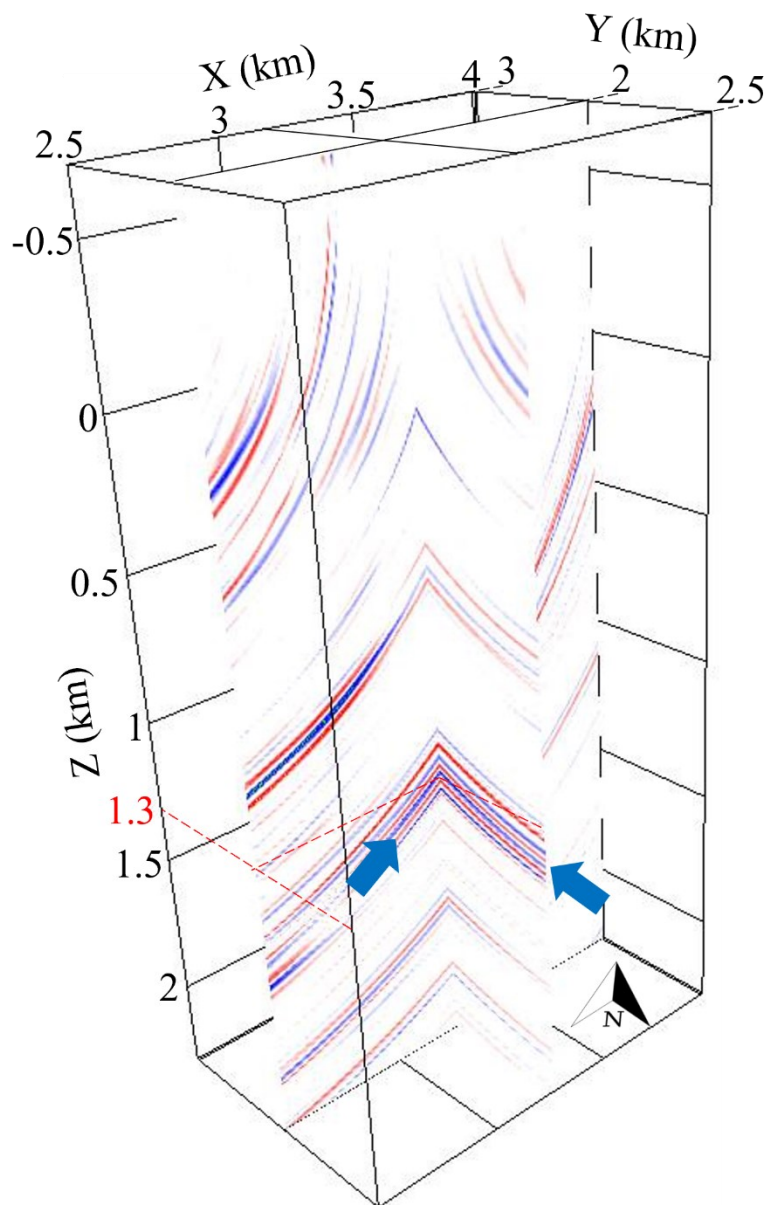


Figure 48: Fence diagram of a small subset from the 3D migrated cube for the reflector depicted in Figure 35 (black arrow). The blue arrows mark the position of the reflector. It is located at $Z= 1.3$ km, Northeast of the survey area. The position of this fence diagram is depicted by the MR red-dashed line in Figure 49.

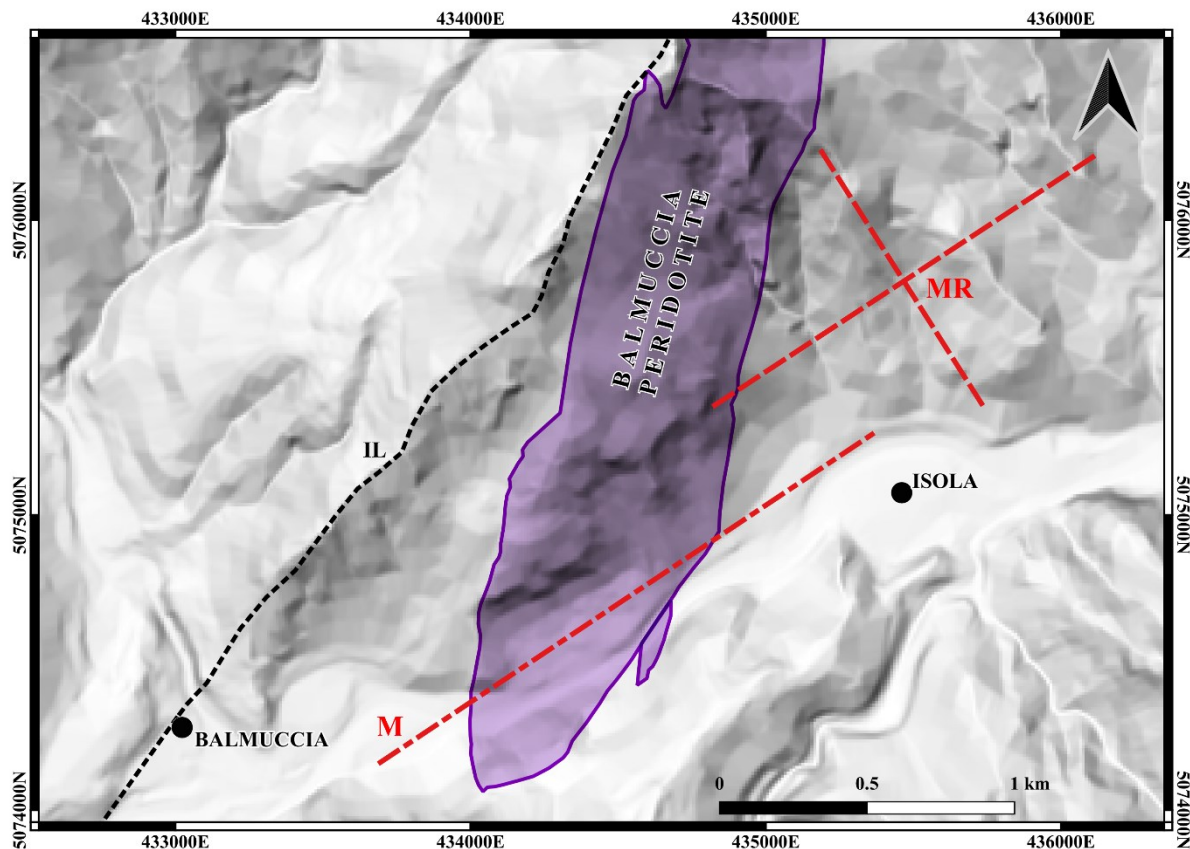


Figure 49: Map showing the position of the slice in Figure 46 as a red-dashed line labeled as *M*. The two red-dashed lines labeled as *MR* represent the position of the slices shown in the fence diagram of Figure 48. *IL*: Insubric Line.

7. Interpretation

7.1. Traveltime tomography

The 2.5D tomography (Figure 25b) shows the limited ray penetration produced by the strong contrast between the weathered layer and the crystalline rocks. This limits the depth of the near-velocity model to a maximum of 0.1 km from surface. In only 0.1 km depth the velocities range from 1 to 8 km/s with a strong horizontal variability of velocity gradients (e.g., 70 km/s km at $X = 1.5$ km and 25 km/s km at $X = 1$ km). There is a clear cone shaped structure with high velocities close to the surface in the middle of the profile, indicating the outcrop of the BP. Then, slower velocities develop towards the NE and the NW which can be associated with sediments. Measurements conducted *in-situ* by Vilhelm et al. (2008) at the outcropping BP show mean velocities from approximately 5 to 6 km/s, with variability dependent on the source offset. Furthermore, their laboratory studies reveal even higher velocities, reaching ca. 8 km/s. They attribute this discrepancy between field and laboratory data to the presence of fractures across the outcrop and the absence of such features in the smaller laboratory samples. Therefore, velocities in the tomographic results from 6 to 8 km/s can be associated with the BP. In addition, velocities below and above 7 km/s are respectively associated with weathered/fractured and relatively undisturbed peridotite. It is evident that at near the surface the BP is not a homogeneous body of 8 km/s but rather a highly fractured body, showing boulder-like shapes where the rock is undisturbed by fractures. Its West and East boundaries, marked as faults in the surface geology (Figure 9, F1 and F2), can be correlated with sharp velocity contrasts (Figure 25b, red lines). In addition, a low velocity area in the middle of the profile ($X = 1$ km) within the BP indicates a highly fractured zone. Another small high-velocity body is visible to the East of fault F1, which could be associated to a sliver of the BP. The presence of a sliver of peridotite to the East of F1 that does not outcrop is possible, since Quick et al. (2003) mapped a smaller outcrop of the BP toward the SE of the Sesia River and East of F1, which confirms the existence of the peridotite body on both sides of the fault. Nevertheless, additional subsurface information is needed to clarify its interpretation, as well as the geological nature of the contact between the peridotite and neighboring units.

A brief interpretation is done to the 3D tomography (Figure 27). The ray coverage for Slice C is like the 2.5D tomography. Therefore, its interpretation is the same as the latter, as it is evident that the same features are visible in both. Slice A exhibits a lack of ray coverage due to

the limited number of receivers and the presence of gaps within Line 3. It displays a thicker low velocity area as Slice B, which can be attributed to quarry activities, back fill and waste dumps. Slices A and B have consistent velocity values with those observed in Slice C, but the contrasts are not as sharp to identify boundaries or possible fractured areas.

7.2. Reflection seismics

The most prominent features observed in the final KPSDM image (Figure 46) correspond to vertical to subvertical structures. A pronounced reflector is evident to the SW starting at approximately $X = 0.3$ km (Figure 46b). This reflector dips towards the NE at an angle of ca. 70° near the surface, decreasing to ca. 45° until it is crosscut by what is interpreted as fault F1. After F1, the reflector continues to the NE dipping at ca. 30° until it is no longer visible. This reflector is interpreted as fault F2 and connects to the SW boundary of the BP mapped at the surface (Quick et al., 2003) and the 2.5D tomography results. In addition, the interpretation is based on following negative amplitude reflections from the near surface to depth, since it is expected that a reflection produced at the Mafic Complex - BP boundary will be characterized by a seismic signal with negative polarity, given that the surrounding Mafic Complex has a lower P-wave velocity than the BP (Khazanehdari et al., 2000). The same approach is used for interpreting fault F1. It starts at approximately $X = 1.4$ km and dips towards the SW, ranging from ca. 65° in the near surface to ca. 30° as depth increases, cutting fault F2 near its end (Figure 46b). Its position correlates with the fault mapped in the surface geology as the NE boundary of the BP (Quick et al., 2003) and the low velocity anomaly in the 2.5D tomography. In addition, by matching its position in the image to the receiver array from Line 1, it is possible to identify that the reflected refraction observed in Figure 36 (PRR2) is imaged as fault F1 (Figure 46, yellow arrow N° 2). Evidently, faults F1 and F2 define a lens-like shape that terminates at ca. $Z = 0.175$ km. It is possible that the BP extends toward the NE, since there is proof of its continuation toward the NE of F1 as described in Subsection 7.1. A small but strong reflector dipping ca. 65° to the SW (Figure 46b, $X = 1.65$ km), and following smaller reflectors, might suggest the existence of a continuing body. However, the image is not clear enough to interpret a continuing sliver of peridotite.

Numerous faults intersect each other within the BP which can be categorized into two primary sets: Southwest-dipping faults and Northeast-dipping faults (Figure 46b, red and

orange lines respectively). Both sets exhibit apparent dip angles of ca. 25° - 75°, except for small sub-horizontal faults with apparent dips of ca. 4° - 12° (Figure 46b, green lines). The high density of SW dipping faults in the X= 0.85 – 1.2 km range could explain the low velocity zone identified at X= 1 km in the 2.5D tomography profile (Figure 25b). As before, the reflected refraction marked as PRR1 in Figure 36 can be matched with one of the imaged Northeast-dipping faults (Figure 46, yellow arrow N° 1).

Beyond the fault-bounded lens-shaped body, several reflections are detected (Figure 46b, blue lines). These cannot be caused only by existing fractures that are favorably oriented for imaging but could be associated with lithological variability and therefore acoustic impedance contrasts. Some of these may be interpreted as intrusions which correlate with those mapped by Quick et al. (2003) as pg4 (paragneiss) and uc (ultramafic cumulus) at the SW side of the BP (Figure 47, blue arrows). Some of the latter reflectors have a sudden termination, which allows to infer possible fractures that are not directly imaged (Figure 46b, dark-red lines). This imaging limitation is inherent to the survey's geometry, which does not allow the imaging of deep-steep or outward dipping reflectors that do not reflect the seismic signal back to the surface. Such steep, deep and outward facing events can only be inferred in the image by their lack of reflectivity and the way they terminate other reflections. As such, there is a high confidence on the lens-shaped body interpretation, which is considered as the minimum interpreted volume for the BP. But the possibility that the BP could extend further laterally and downwards, continuously, with slivers or highly fractured areas should be considered.

Figure 48 depicts the position of the reflector shown in Subsection 6.1 (Figure 35, black arrow). It is imaged as an out-of-plane reflector North of the surveyed area at ca. 1.3 km below sea level.

8. Discussion

The BP exhibits significant heterogeneity, primarily attributed to the abundance of fractures and intrusions, which have been extensively studied and documented by various authors (e.g. Handy & Stünitz, 2002; Souquière & Fabbri, 2010; Ferrand et al., 2018; Ueda et al., 2020). Recently, Menegoni et al. (2024) introduced a novel approach to assess the discontinuities within the BP outcrop using aerial drone-based photogrammetry for structural analysis. Through their interpretation and mapping of these discontinuities across the outcrop, they calculated the respective areal discontinuity intensity. Their findings emphasize that the central area of the BP exhibits elevated levels of heterogeneity. This area correlates with the low velocity anomaly in the middle of the 2.5D tomography profile (Figure 50). This indicates that a higher level of discontinuities (fractures and intrusions) produce a decrease in the rock's seismic velocity. In addition, this correlation allows to confirm that the high discontinuity intensity seen at surface extends to a depth up to ~ 0.1 km.

The interpretation of the seismic images highlights the intricate geological structure of the BP, characterized by a complex network of faults (Figure 47). Remarkably, these findings correlate with the classification proposed by Ueda et al. (2020) for the faults observed across the BP outcrop (Figure 51). They classify these faults into three distinct groups (Groups 1-3) based on mineralogical and microstructural characteristics and establish the chronological sequence of each group according to their formation stage and their crosscutting relationship. Consequently, faults in Group 1 are intersected by those from Group 2, and both Groups 1 and 2 are intersected by Group 3. Adopting to this group classification, it can be concluded that the sets of faults dipping toward the NE can be classified as Group 1 since they are cut by the set of faults dipping to the SW representing Group 2. Furthermore, the small sub-horizontal faults intersect Group 2, placing them within Group 3.

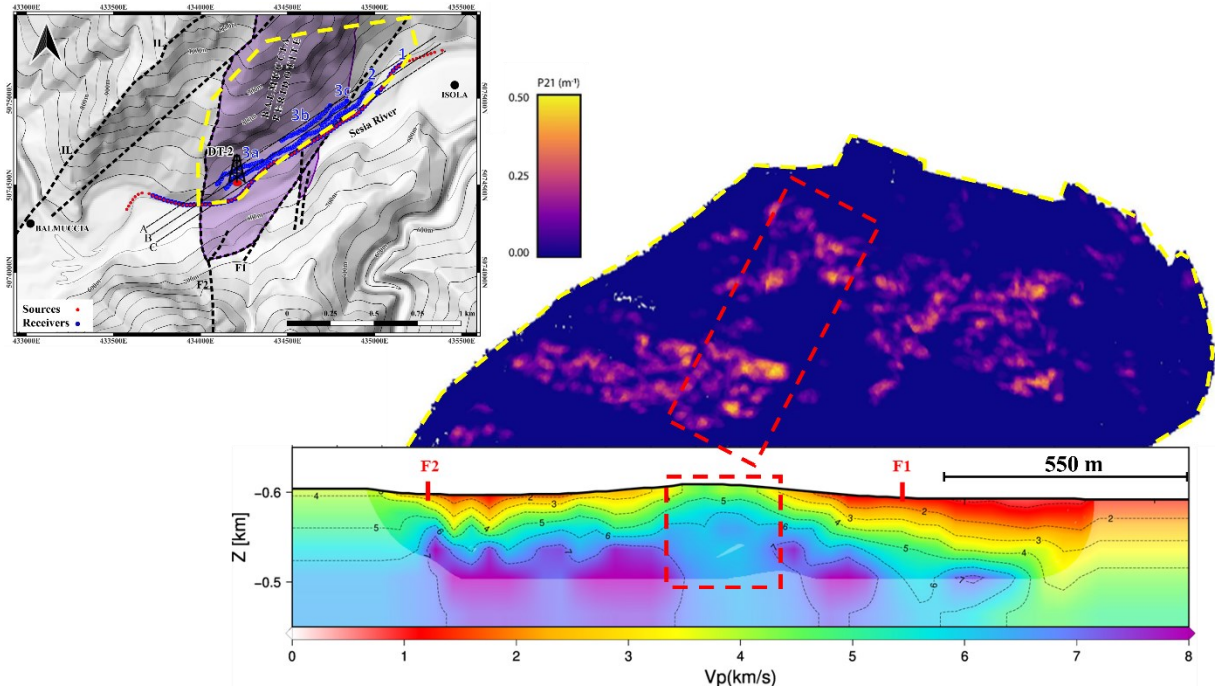


Figure 50: Comparison between the two-dimensional tomographic results and the discontinuity density map by Menegoni et al. (2024). The map at the top right depicts the area analyzed to obtain the discontinuity density map with a yellow polygon. The center image shows a density map of discontinuities, yellow/orange colors representing high density values. This map represents the face of the outcrops analyzed; it is not a map view. The two-dimensional tomography is added as comparison to correlate the high density of discontinuities with the low velocity zone at the middle of the profile. Red squares with dashed-lines show the area that correlates the high values in the density map with the low velocity anomaly in the tomography.

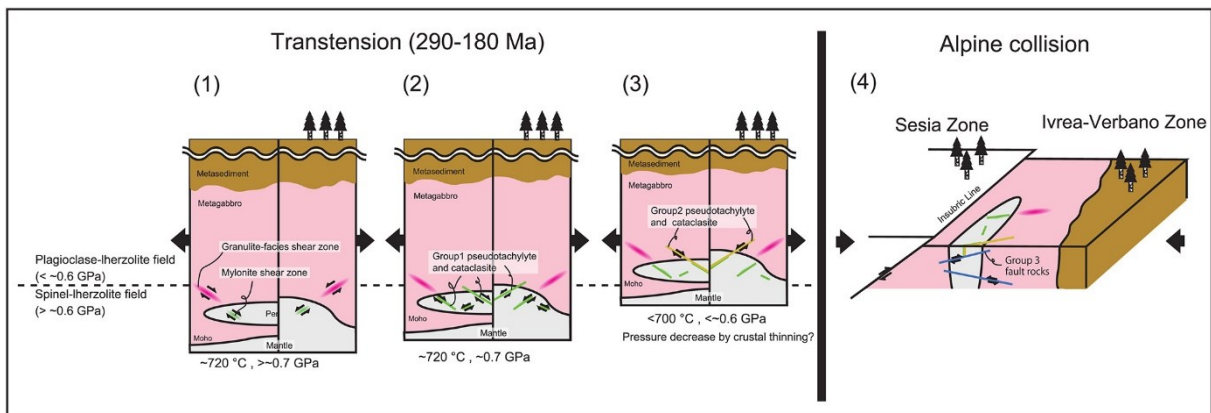


Figure 51: Schematic picture depicting the formation of the different groups of faults. (1) & (2) Formation of Group 1. (3) Formation of Group 2. (4) Formation of Group 3. After Ueda et al. (2020).

The velocities and the interpreted seismic image point towards the BP as a lens-like body, not dissimilar to the body proposed by Quick et al. (1995) (Figure 47). The peridotite body is bounded by faults (faults F1 and F2) that does not broaden at depth but instead cross at ca. 0.175 km b.s.l. or ca. 0.875 km below surface. This is different from the findings of Ryberg et al. (2023), who suggest that the BP represents the contiguous surface expression of the IGB and is not an isolated body. The velocities of 6 – 6.5 km/s for the BP in their model are also lower than in this work's tomographic results, which indicate velocities of 6 – 8 km/s with a mean velocity of 7 km/s for the BP. Moreover, the velocities observed closely align with those obtained from rock sample measurements across the area (e.g. Burke & Fountain, 1990; Khazanehdari et al., 2000; Vilhelm et al., 2008). The explanation for the differences to the model of Ryberg et al. (2023) is that their resolution is too coarse to resolve the small spatial details of the BP. Evidently, both results were obtained using different survey geometries and tomographic approaches, with velocity models obtained at scales that cannot be directly compared. However, both models are valid and should be interpreted simultaneously. Then, the Ryberg model is considered as a valuable regional velocity model, able to explain the general velocity distribution of the IVZ to larger depths. The higher resolution velocity model obtained in this thesis, although very shallow, shows a strong gradient of velocities, reaching up to 8 km/s in only 0.1 km depth. The fact that these high velocities are not seen in the near-surface in Ryberg's velocity model implies that: (1) their resolution is not high enough to resolve small-scale near-surface variations and (2) the BP might not be contiguously attached to the deeper IGB. If the BP is considered as a contiguous broadening body, as in the Ryberg model, but using the velocity estimations from this work, it should be detectable at the resolution of the Ryberg tomography. However, this is not the case.

The reflection seismic image is poorly constrained below the interpreted volume of the BP (Figure 47, yellow question marks), which leaves the door open to alternative interpretations. The BP body could continue in depth and connect to the IGB as a thin and highly heterogeneous body, which could explain the gradient of velocities observed by Ryberg et al. (2023). Longer offset data, that were recorded during the SEIZE survey, could be utilized to clarify the lower section of the image when the SEIZE time-break data becomes available.

9. Conclusions

The tomographic velocity model obtained through inversion of the P-wave first-arrival picks shows the outline of the BP highlighting its East and West boundaries, as mapped by Quick et al. (2003). In addition, the model shows velocities of 6 – 8 km/s which agree with velocity values obtained from rock samples across the area. Furthermore, a velocity of 7 km/s can be considered as a mean velocity for the BP.

The middle of the peridotite body is characterized by a decrease in velocity in the tomographic results. Its correlation with recent studies from Menegoni et al. (2024) show that it could be related to an increase of discontinuities within the body, establishing a compelling link between a higher density of discontinuities and a reduction in the rock's seismic velocity.

A cross-section of the area of interest from the 3D KPSDM illustrates the structure of the BP. This cross-section reveals that the two main faults bounding the BP at the surface cross at depth and define a lens-like shape as proposed by Quick et al. (1995). Based on this interpretation, the BP extends to a depth of ca. 0.175 km b.s.l. (0.875 km below surface) with an apparent width of ca. 1 km, with poorer resolution beyond that shape.

Considering the results obtained from the 2.5D tomography and the interpretation of the seismic image, it is concluded that the BP is a lens of mantle material, not contiguously attached to the IGB, which would discard the theory that the contact between the BP and the Mafic Complex represents a fossil continental crust-mantle transition zone (Shervais, 1979; Rivalenti et al., 1981). Nevertheless, the limitations to clearly image the deeper part between the lens-shape and the IGB leaves room to other interpretations as discussed in Section 8.

Migration of the clearest reflector in the data (Figure 35, black arrow) with a constant velocity model of 7 km/s locates the reflector at a depth of ca. 1.3 km b.s.l. (Figure 48). This depth is in agreement with the depth of the IGB proposed by Scarponi et al. (2020). Thus, the imaged reflector could be considered as the top of the contiguous IGB.

These results will assist in the localization and orientation of borehole DT-2 planned by project DIVE, and aid to the comprehension of the relationship between the geological units of the area including fractures, lithological variability across scales, and ultimately the crust-mantle transition.

Acknowledgements

I want to thank Prof. Bleibinhaus for believing in me and giving me the opportunity to study under his supervision. Not everyone in Europe gives an opportunity to someone from South America to study in Europe. It was 2020, and the pandemic was just starting. It was a very tough situation worldwide. Without this opportunity, I do not know what would have become of me. Thank you very much.

Thank you to Dr. Andrew Greenwood, who organized the whole Hi-SEIZE acquisition campaign. I believe that without him, this project would never have happened. I have learnt many things from Andrew, but there are two phrases from him that will always be in my mind: “You did not do it until you did it at least 3 times” and “it is not seismic imaging, it is seismic imagination”. Thank you as well for those very needed after-office beers and the climbing lessons in Balmuccia.

I want to thank Mrs. Christiane Pretzenbacher for her help since day one. I would not have been able to do all the Austrian paperwork and bureaucracy without her. She took care of me, and I will never forget that. I hope some day I will be able to give her back at least half of what she gave to me.

Thank you to Natalia Banasiak for helping us during the data acquisition in Italy. Those batteries were not light, and without her, it would have been impossible to finish everything on time. But more than that, I thank her for being there when I needed to talk to someone.

Thank you to all the people from the Chair of Applied Geophysics that were there during this four-year journey. Each of you kept me company and made this journey more pleasant.

One of my most important thanks is to Elena: thank you for being there every day, helping me and making me happy. I am lucky to have found you here in this little town in the middle of Austria.

Last but not least, thanks to my parents, to whom I will write in Spanish: Mamá, Papá, gracias por haber estado siempre ahí, a pesar de que un océano nos separe. Gracias por el esfuerzo que hicieron para que esa ciudadanía salga y tenga la oportunidad de venir a Europa. Espero algún día poder devolverles todo lo que me dieron.

References

- Ansorge, J., Mueller, S., Kissling, E., Guerra, I., Morelli, G. & Scaracia, S., 1979. Crustal section across the zone of Ivrea - Verbano from the Valais to the Lago Maggiore. *Bollettino di Geofisica Teorica ed Applicata*, 21, 149–157.
- Bayer, R., Carozzo, M.T., Lanza, R., Miletto, M. & Rey, D., 1989. Gravity modelling along the ECORS-CROP vertical seismic reflection profile through the Western Alps. *Tectonophysics*, 162(3), 203–218. doi:10.1016/0040-1951(89)90244-8.
- Bednar, J. & Watt, T., 1984. Alpha-trimmed means and their relationship to median filters. *IEEE Transactions on Acoustics, Speech, and Signal Processing*, 32(1), 145–153. doi:10.1109/TASSP.1984.1164279.
- Berckhemer, H., 1968. Topographie des “Ivrea-Körpers” abgeleitet aus seismischen und gravimetrischen Daten. *Schweiz. Mineral. Petrogr. Mitt*, 48(1), 235–246.
- Bleibinhaus, F. & Gebrande, H., 2006. Crustal structure of the Eastern Alps along the TRANSALP profile from wide-angle seismic tomography. *Tectonophysics*, 414(1-4), 51–69. doi:10.1016/j.tecto.2005.10.028.
- Boriani, A. & Sacchi, R., 1973. Geology of the junction between the Ivrea-Verbano and Strona-Ceneri Zones. *Mem. 1st. Geol. Mineral. Univ. Padova*, 28, 1–36.
- Boudier, F., Jackson, M. & Nicolas, A., 1984. Structural study of the Balmuccia massif (western Alps): A transition from mantle to lower crust. *Geologie en Mijnbouw*, 63(2), 179–188.
- Burke, M.M. & Fountain, D.M., 1990. Seismic properties of rocks from an exposure of extended continental crust—new laboratory measurements from the Ivrea Zone. *Tectonophysics*, 182(1-2), 119–146. doi:10.1016/0040-1951(90)90346-A.
- Diehl, T., Husen, S., Kissling, E. & Deichmann, N., 2009. High-resolution 3-D P -wave model of the Alpine crust. *Geophysical Journal International*, 179(2), 1133–1147. doi:10.1111/j.1365-246X.2009.04331.x.
- Eaton, D.W., Milkereit, B. & Salisbury, M.H. (2003) *Hardrock Seismic Exploration*. Society of Exploration Geophysicists.
- Ernst, W.G., 1978. Petrochemical Study of Lherzolitic Rocks from the Western Alps. *Journal of Petrology*, 19(3), 341–392. doi:10.1093/petrology/19.3.341.

- Ferrand, T.P., Labrousse, L., Eloy, G., Fabbri, O., Hilairet, N. & Schubnel, A., 2018. Energy Balance From a Mantle Pseudotachylyte, Balmuccia, Italy. *Journal of Geophysical Research: Solid Earth*, 123(5), 3943–3967. doi:10.1002/2017JB014795.
- Fountain, D.M., 1976. The Ivrea—Verbano and Strona-Ceneri Zones, Northern Italy: A cross-section of the continental crust—New evidence from seismic velocities of rock samples. *Tectonophysics*, 33(1-2), 145–165. doi:10.1016/0040-1951(76)90054-8.
- Galson, D. & Mueller, S., 1986. An introduction to the European Geotraverse Project: First results and present plans. *Tectonophysics*, 126(1), 1–30. doi:10.1016/0040-1951(86)90218-0.
- Galson, D.A. & Mueller, S., 1987. The European Geotraverse (EGT) project: A progress report, 16, 253–272. doi:10.1029/GD016p0253.
- Handy, M.R., 1987. The structure, age and kinematics of the Pogallo Fault Zone; Southern Alps, northwestern Italy. *Eclogae Geologicae Helvetiae*, 80(3), 593–632.
- Handy, M.R. & Stünitz, H., 2002. Strain localization by fracturing and reaction weakening — a mechanism for initiating exhumation of subcontinental mantle beneath rifted margins. *Geological Society, London, Special Publications*, 200(1), 387–407. doi:10.1144/gsl.sp.2001.200.01.22.
- Hedin, P., Almqvist, B., Berthet, T., Juhlin, C., Buske, S. & Simon, H. et al., 2016. 3D reflection seismic imaging at the 2.5km deep COSC-1 scientific borehole, central Scandinavian Caledonides. *Tectonophysics*, 689, 40–55. doi:10.1016/j.tecto.2015.12.013.
- Hetényi, G., Molinari, I., Clinton, J., Bokelmann, G., Bondár, I. & Crawford, W.C. et al., 2018. The AlpArray Seismic Network: A Large-Scale European Experiment to Image the Alpine Orogen. *Surveys in geophysics*, 39(5), 1009–1033. doi:10.1007/s10712-018-9472-4.
- Hole, J.A., Thybo, H. & Klemperer, S.L., 1996. Seismic reflections from the near-vertical San Andreas Fault. *Geophysical Research Letters*, 23(3), 237–240. doi:10.1029/96GL00019.
- Hole, J.A. & Zelt, B.C., 1995. 3-D finite-difference reflection travel times. *Geophysical Journal International*, 121(2), 427–434. doi:10.1111/j.1365-246X.1995.tb05723.x.
- Khazanehdari, J., Rutter, E.H. & Brodie, K.H., 2000. High-pressure-high-temperature seismic velocity structure of the midcrustal and lower crustal rocks of the Ivrea-Verbano zone and Serie dei Laghi, NW Italy. *Journal of Geophysical Research*, 105(B6), 13843–13858. doi:10.1029/2000JB900025.
- Kissling, E. (1984) Three-dimensional gravity model of the Northern Ivrea-Verbano zone. In: *Comm. Suisse Geophysique*, pp. 53–61.

- Kissling, E., 1993. Deep structure of the Alps—what do we really know? *Physics of the Earth and Planetary Interiors*, 79(1-2), 87–112. doi:10.1016/0031-9201(93)90144-X.
- Kissling, E., Schmid, S.M., Lippitsch, R., Ansorge, J. & Fügenschuh, B., 2006. Lithosphere structure and tectonic evolution of the Alpine arc: new evidence from high-resolution teleseismic tomography. *Geological Society, London, Memoirs*, 32(1), 129–145. doi:10.1144/GSL.MEM.2006.032.01.08.
- Klemperer, S.L., 1987. Seismic noise-reduction techniques for use with vertical stacking: An empirical comparison. *GEOPHYSICS*, 52(3), 322–334. doi:10.1190/1.1442306.
- Lensch, G.P. (1969) *Die ultramafitite der zone von Ivrea*. Verlag nicht ermittelbar.
- Lu, Y., Stehly, L. & Paul, A., 2018. High-resolution surface wave tomography of the European crust and uppermost mantle from ambient seismic noise. *Geophysical Journal International*, 214(2), 1136–1150. doi:10.1093/gji/ggy188.
- Menegoni, N., Panara, Y., Greenwood, A., Mariani, D., Zanetti, A. & Hetényi, G., 2024. Fracture network characterisation of the Balmuccia peridotite using drone-based photogrammetry, implications for active-seismic site survey for scientific drilling. *Journal of Rock Mechanics and Geotechnical Engineering*. doi:10.1016/j.jrmge.2024.03.012.
- Miller, H., 1976. A Lithospheric Seismic Profile along the Axis of the Alps, 1975. I: First Results. *Pure and Applied Geophysics*, 114, 1109–1130.
- Nicolas, A., Hirn, A., Nicolich, R. & Polino, R., 1990. Lithospheric wedging in the western Alps inferred from the ECORS-CROP traverse. *Geology*, 18(7), 587. doi:10.1130/0091-7613(1990)018<0587:LWITWA>2.3.CO;2.
- Niggli, E., 1946. Über den Zusammenhang zwischen der positiven Schwereanomalie am Südfuß der Westalpen und der Gesteinszone von Ivrea. *Eclogae Geologicae Helvetiae*, 39, 211–220.
- Pfiffner, O.A., Frei, W., Valasek, P., Stäuble, M., Levato, L. & DuBois, L. et al., 1990. Grustal shortening in the Alpine Orogen: Results from deep seismic reflection profiling in the eastern Swiss Alps, Line NFP 20-east. *Tectonics*, 9(6), 1327–1355. doi:10.1029/TC009i006p01327.
- Pistone, M., Müntener, O., Ziberna, L., Hetényi, G. & Zanetti, A., 2017. Report on the ICDP workshop DIVE (Drilling the Ivrea–Verbano zone). *Scientific Drilling*, 23, 47–56. doi:10.5194/sd-23-47-2017.
- Quick, J., Sinigoi, S., Snoke, A., Kalakay, T., Mayer, A. & Peressini, G., 2003. Geologic map of the Southern Ivrea-Verbano Zone, Northwestern Italy. *Geologic Investigation Series*, v.I-2776 (2003).

- Quick, J.E., Sinigoi, S. & Mayer, A., 1995. Emplacement of mantle peridotite in the lower continental crust, Ivrea-Verbano zone, northwest Italy. *Geology*, 23(8), 739. doi:10.1130/0091-7613(1995)023<0739:EOMPIT>2.3.CO;2.
- Quick, J.E., Sinigoi, S., Negrini, L., Demarchi, G. & Mayer, A., 1992. Synmagmatic deformation in the underplated igneous complex of the Ivrea-Verbano zone. *Geology*, 20(7), 613. doi:10.1130/0091-7613(1992)020<0613:SDITUI>2.3.CO;2.
- Rivalenti, G., 1975. The origin of the Ivrea-Verbano basic formation (western Italian Alps): Whole rock geochemistry.
- Rivalenti, G., Garuti, G., Rossi, A., Siena, F. & Sinigoi, S., 1981. Existence of Different Peridotite Types and of a Layered Igneous Complex in the Ivrea Zone of the Western Alps. *Journal of Petrology*, 22(1), 127–153. doi:10.1093/petrology/22.1.127.
- Robinson, E.A. & Treitel, S. (2008) *Digital imaging and deconvolution: The ABCs of seismic exploration and processing*. Society of Exploration Geophysicists.
- Rutter, E.H., Brodie, K.H. & Evans, P.J., 1993. Structural geometry, lower crustal magmatic underplating and lithospheric stretching in the Ivrea-Verbano zone, northern Italy. *Journal of Structural Geology*, 15(3-5), 647–662. doi:10.1016/0191-8141(93)90153-2.
- Ryberg, T., Haberland, C., Wawerzinek, B., Stiller, M., Bauer, K. & Zanetti, A. et al., 2023. 3-D imaging of the Balmuccia peridotite body (Ivrea–Verbano zone, NW-Italy) using controlled source seismic data. *Geophysical Journal International*, 234(3), 1985–1998. doi:10.1093/gji/ggad182.
- Scarponi, M., Hetényi, G., Berthet, T., Baron, L., Manzotti, P. & Petri, B. et al., 2020. New gravity data and 3-D density model constraints on the Ivrea Geophysical Body (Western Alps). *Geophysical Journal International*, 222(3), 1977–1991. doi:10.1093/gji/ggaa263.
- Scarponi, M., Hetényi, G., Plomerová, J., Solarino, S., Baron, L. & Petri, B., 2021. Joint Seismic and Gravity Data Inversion to Image Intra-Crustal Structures: The Ivrea Geophysical Body Along the Val Sesia Profile (Piedmont, Italy). *Frontiers in Earth Science*, 9. doi:10.3389/feart.2021.671412.
- Scarponi, M., Kvapil, J., Plomerová, J., Solarino, S. & Hetényi, G., 2023. New constraints on the shear wave velocity structure of the Ivrea geophysical body from seismic ambient noise tomography (Ivrea-Verbano Zone, Alps). *Geophysical Journal International*, 236(2), 1089–1105. doi:10.1093/gji/ggad470.
- Schmid, S.M., Kissling, E., Diehl, T., van Hinsbergen, D.J.J. & Molli, G., 2017. Ivrea mantle wedge, arc of the Western Alps, and kinematic evolution of the Alps–Apennines orogenic system. *Swiss Journal of Geosciences*, 110(2), 581–612. doi:10.1007/s00015-016-0237-0.

- Schmid, S.M., Zingg, A. & Handy, M., 1987. The kinematics of movements along the Insubric Line and the emplacement of the Ivrea Zone. *Tectonophysics*, 135(1-3), 47–66. doi:10.1016/0040-1951(87)90151-X.
- Shervais, J.W., 1978. Ultramafic and mafic layers in the alpine-type lherzolite massif at Balmuccia, N. W. Italy. *Memorie di Scienze Geologiche*, 33.
- Shervais, J.W., 1979. Thermal Emplacement Model for the Alpine Lherzolite Massif at Balmuccia, Italy. *Journal of Petrology*, 20(4), 795–820. doi:10.1093/petrology/20.4.795.
- Simon, M., Gebrande, H. & Bopp, M., 1996. Pre-stack migration and true-amplitude processing of DEKORP near-normal incidence and wide-angle reflection measurements. *Tectonophysics*, 264(1-4), 381–392. doi:10.1016/S0040-1951(96)00138-2.
- Souquière, F. & Fabbri, O., 2010. Pseudotachylytes in the Balmuccia peridotite (Ivrea Zone) as markers of the exhumation of the southern Alpine continental crust. *Terra Nova*, 22(1), 70–77. doi:10.1111/j.1365-3121.2009.00918.x.
- Spada, M., Bianchi, I., Kissling, E., Agostinetti, N.P. & Wiemer, S., 2013. Combining controlled-source seismology and receiver function information to derive 3-D Moho topography for Italy. *Geophysical Journal International*, 194(2), 1050–1068. doi:10.1093/gji/ggt148.
- Thouvenot, F., Paul, A., Senechal, G., Hirn, A. & Nicolich, R., 1990. ECORS-CROP wide-angle reflection seismics: constraints on deep interfaces beneath the Alps. *Mém. Soc. Géol. France*, 156, 97–106.
- Thurber, C.H., 1983. Earthquake locations and three-dimensional crustal structure in the Coyote Lake Area, central California. *Journal of Geophysical Research*, 88(B10), 8226–8236. doi:10.1029/JB088iB10p08226.
- Tillmanns, M. & Gebrande, H. (1999) Focusing in Prestack Isochrone Migration Using Instantaneous Slowness Information. In: Gajewski, D. & Rabbel, W. (Eds.) *Seismic Exploration of the Deep Continental Crust: Methods and Concepts of DEKORP and Accompanying Projects*. Birkhäuser Basel: Basel, pp. 187–206.
- Ueda, T., Obata, M., Ozawa, K. & Shimizu, I., 2020. The Ductile-to-Brittle Transition Recorded in the Balmuccia Peridotite Body, Italy: Ambient Temperature for the Onset of Seismic Rupture in Mantle Rocks. *Journal of Geophysical Research: Solid Earth*, 125(2), e2019JB017385. doi:10.1029/2019JB017385.
- Valasek, P., St. Mueller, Frei, W. & Holliger, K., 1991. Results of NFP 20 seismic reflection profiling along the Alpine section of the European Geotraverse (EGT). *Geophysical Journal International*, 105(1), 85–102. doi:10.1111/j.1365-246X.1991.tb03446.x.

- Vecchia, O., 1968. La zone Cuneo-Ivrea-Locarno, élément fondamental des Alpes. Géophysique et géologie. Schweizerische Mineralogische Petrographische Mitteilungen, 48, 215–226.
- Vilhelm, J., Rudajev, V., Zivor, R., Lokajicek, T. & Pros, Z., 2008. Comparison of field and laboratory seismic velocity anisotropy measurement (scaling factor). Acta Geodyn Geomater, 5(2), 150.
- Voshage, H., Hofmann, A.W., Mazzucchelli, M., Rivalenti, G., Sinigoi, S. & Raczek, I. et al., 1990. Isotopic evidence from the Ivrea Zone for a hybrid lower crust formed by magmatic underplating. Nature, 347(6295), 731–736. doi:10.1038/347731a0.
- Zingg, A., 1983. The Ivrea and Strona-Ceneri zones (Southern Alps, Ticino and N-Italy)—A review. Schweizerische mineralogische und petrographische Mitteilungen, 63(2-3), 361–392.
- Zingg, A., Handy, M., Hunziker, J. & Schmid, S., 1990. Tectonometamorphic history of the Ivrea Zone and its relationship to the crustal evolution of the Southern Alps. Tectonophysics, 182(1-2), 169–192. doi:10.1016/0040-1951(90)90349-D.

List of figures

Figure 1: Geologic map of the southern Alps color-coded with the main formations that constitute the IVZ and its surroundings (see legend on map). Main faults are depicted as dashed lines. Proposed drill sites by project DIVE are marked with black circles with their respective names. The study area (SA) is marked with a yellow square. Balmuccia Peridotite (BP). Finero Peridotite (FP). Modified from Zingg (1983). 2

Figure 2: Seismic image from the ECORS-CROP study. The red-dashed square highlights how transparent the seismic image is for the first 4 km in the Ivrea Zone. Modified from Nicolas et al. (1990). 5

Figure 3: Proposed geophysical model of the IGB by Berckhemer (1968). The top figure shows the fit between the measured and computed gravity anomalies. The bottom figure depicts the model used for the computed anomalies. 7

Figure 4: Figure from Scarponi et al. (2021) showing their study area (top figure) and the perspective view of the IGB 3D density model (bottom) obtained by Scarponi et al. (2020). The red triangles represent a temporary seismic array (IvreaArray) installed specifically for their study. Refer to Scarponi et al. (2021) for more details on this figure. 8

Figure 5: Figure from Scarponi et al. (2023) showing a vertical cross-section of the 3D Vs model obtained in their study through ANT. White dots represent the Moho depth from Spada et al. (2013), red triangles on top indicate the location of the IvreaArray seismic stations. The Magenta contour represents a cross-section through the 3D IGB density model from Scarponi et al. (2020). Refer to Scarponi et al. (2023) for more details on this figure. 9

Figure 6: Map illustrating the extent of the SEIZE and Hi-SEIZE seismic surveys as red and blue lines respectively. The proposed drill site by project DIVE is marked as a yellow star on top of the Balmuccia Peridotite drawn in violet. The dark-red-dashed line shows the location of the cross-section depicted in Figure 7. IL: Insubric Line. 10

Figure 7: Cross-section through the 3D velocity model of Ryberg et al. (2023) (see Figure 6 for location). The 6 km/s, 6.5 km/s and 7 km/s velocity isolines (black line) are shown for reference. The planned drilling location is marked as a yellow star. The location and extent of the Insubric Line is marked as thick green line at the top of the figure. The dashed-dotted black line shows the top of the IGB proposed by Scarponi et al. (2020). Figure modified from Ryberg et al. (2023). 11

Figure 8: A picture taken during Line 3 set up. A large rockslide impeded the continuous set up of receivers. A significant gap was introduced to the geometry, dividing Line 3 into two

segments (3a and 3b). Segment 3a finishes behind the photographer. Segment 3b starts after the hill that is observed in the distance. 14

Figure 9: Digital elevation model of the study area showing the final location of 357 receivers (blue points) and 96 sources (red points). Both Line 1 and the source line follow a local road connecting the towns of Balmuccia and Isola. Lines 2 and 3 are deployed along access roads of an old, abandoned quarry. Difficult terrain forced the division of Line 3 into 3 sub lines (3a, 3b and 3c). Dashed lines A, B and C represent the three tomography slices for the 3D tomography (Figure 27). The tentative drill site by project DIVE is represented by a small black rig symbol over a red patch. F1: Main fault cutting the BP representing its NE boundary. F2: Main fault representing the SW boundary of the BP. Insubric Line (IL)..... 15

Figure 10: Images of the sensors and acquisition systems used in each receiver line. Each receiver is shown with its parameters. To the right a photograph taken during acquisition of the vibroseis used. The Vibroseis characteristics and the sweep parameters are described at the top of the photograph. 17

Figure 11: Shot gather N°1112 showing the uncorrelated data from the Unite system at Line 1. This gather is one of four gathers obtained at the same VP position. The traffic noise is marked with green arrows. The vibroseis position is marked with a red star. 19

Figure 12: Same uncorrelated shot gather as in Figure 11 after DVS. The vibroseis position is marked with a red star. The strong noise from the traffic is not visible anymore thanks to the DVS process. 21

Figure 13: Same shot gather as in Figure 12 after vibroseis sweep correlation. The vibroseis position is marked with a red star. 22

Figure 14: Comparison between amplitude and phase response of the 4.5 Hz and 10 Hz geophone. The yellow-dotted line represents the filter obtained through Equation 2. 24

Figure 15: Comparison between amplitude and phase response of the accelerometer (after integration) and 10 Hz geophone. The yellow-dotted line represents the filter obtained through Equation 2. 25

Figure 16: Elevation profile (top) and position (bottom) of receivers and sources. Green circles and numbers mark the start and end of the numbering defined for each line. Red circles: shots. Blue circles: receivers. 26

Figure 17: Shot gather N°1170 from Line 2. The black arrow marks the noise produced by the electric generator. Red arrows mark the P and S-wave first arrivals..... 27

Figure 18: Raw shot gather. AGC window of 500 ms applied for better visualization. Colored arrows outline the P- and S-wave first arrivals (red), P and S-wave reflected refractions

(yellow), air wave (blue), a reflection at approximately 700 ms (black) and a strange behavior of the first arrivals (green). Thick purple lines mark the approximated position of the West and East boundaries of the BP. SRR: S-wave Reflected Refraction. PRR: P-wave Reflected Refraction. BPW: Balmuccia Peridotite – West boundary. BPE: Balmuccia Peridotite – East boundary. 28

Figure 19: Comparison of the vertical, radial and transverse components from Line 1. The black arrow shows the position of the reflector for each component. An AGC window of 1000 ms was applied for visualization. 31

Figure 20: Before (left) and after (right) minimum phase conversion. First breaks picked on the minimum phase data are shown in green on both panels for comparison. 33

Figure 21: First arrival times from Line 1 for seven selected shots. Observed traveltimes are plotted as continuous red lines. Blue-dashed lines represent the calculated traveltimes obtained for the final velocity model in the two-dimensional inversion (see Subsection 5.1). 33

Figure 22: Histogram of the differences between forward and reverse traveltimes. The bin size used is 1 ms, equal to the sampling interval. The y axis represents the number of pairs receiver-shot, and the x axis is the time difference between the forward and reverse traveltimes. 34

Figure 23: 2.5D tomographic inversion results for increasingly finer grid spacings from (a) to (d). The horizontal and vertical spacings (in meters) are given in the lower left corner of each model. The vertical spacing refers to the uppermost grid layer and increases with depth by 28% in all models. The corresponding RMS misfit is given in the bottom right corner. Areas without ray coverage are semi-transparently whitened. Z axis exaggerated at 2:1. 36

Figure 24: Velocity test for the 2.5D tomography. The X axis represents the maximum velocity allowed in the inversion. The Y axis is the RMS error obtained for each velocity. The mean data uncertainty is shown as a dashed blue line. Only velocities above that threshold can explain the observed traveltimes in the inversion process. 37

Figure 25: Comparison between velocity models applying a velocity cut-off to the inversion. (a) $V_{max} = 7 \text{ km/s}^1$. (b) $V_{max} = 8 \text{ km/s}$. (c) $V_{max} = 9 \text{ km/s}$. The chosen model (b) shows the geologically mapped positions of faults F1 and F2 (see Figure 9). 38

Figure 26: RMS misfit for increasingly finer grid spacings during the grid refinement process for the three-dimensional inversion. The X axis represents the grid configuration (in meters), and the Y axis is the RMS error obtained for each grid. The mean data uncertainty is shown as a dashed blue line. 39

Figure 27: Slices A, B and C from the three-dimensional inversion (see dashed lines in Figure 9). The 5.5 km/s ¹ isoline considered as the reference datum is marked with dashed lines. Only areas with hypothetical ray coverage are displayed. Y axis exaggerated 6:1.....	40
Figure 28: Seismic data examples from the DEKORP pre-site seismic survey. a) Common shot gather with strong events at approximately 3.8 s. b) CMP gather from the same location showing the lack of coherency of the events identified in a). After Simon et al. (1996).....	42
Figure 29: Shot gathers after spherical divergence correction, trace normalization and air wave muting. The green line follows the P-wave first break picks for each shot gather. Red arrows mark the P and S-wave first arrivals. Top row: shot point N° 986(left) and N° 1034 (right). Bottom row: shot point N° 1106 (left) and N° 1166 (right).....	44
Figure 30: Example of an f-k spectrum analysis for a shot gather acquired with receiver Line 2 after amplitude balancing and air wave mute. Top-left: Shot gather before the application of the f-k filter. Top-right: f-k spectrum with shaded areas representing the f-k filter to be applied. Botom: Shot gather after the application of the designed f-k filter.	46
Figure 31: Example of an f-k spectrum analysis for a shot gather acquired with receiver Line 2 after amplitude balancing, air wave mute and P-wave flattening. Top-left: Shot gather before the application of the f-k filter. Top-right: f-k spectrum with shaded areas representing the f-k filter to be applied. Botom: Shot gather after the application of the designed f-k filter. The red arrows mark the P and S-wave first arrivals.	47
Figure 32: Example of the median filter applied to a shot gather to reduce the P-wave first arrivals.....	49
Figure 33: Example of the median filter applied to a shot gather to reduce the S-wave first arrivals. Panel (a) is the output from the P-wave first arrival filtering depicted in Figure 33e.	49
Figure 34: Band-pass filter test. The top-left panel shows the shot gather N°1032 (see Figure 16 for location) after filtering of the S-wave first arrivals with no band pass filter applied. Blue arrows mark the unwanted low-frequency signal. The remaining panels show the results after applying different band-pass filters. The corner frequencies for every band-pass filter are shown at the top-right corner of each panel.	50
Figure 35: Shot gather after direct P- and S-wave removal and band-pass filter. Red arrows mark the removed direct P- and S-wave arrivals. P and S-wave reflected refractions are marked as yellow arrows. The blue arrow marks the removed air wave. The black arrow shows the reflector at ca. 700 ms. SRR: S-wave Reflected Refraction. PRR: P-wave Reflected Refraction.	51

Figure 36: Example of reflected refractions in shot gather N° 1182 after processing. Two P-wave reflected refractors are marked with yellow arrows. PRR1: P-wave Reflected Refraction 1. PRR2: P-wave Reflected Refraction 2. Offset in meters.	52
Figure 37: Slice C from the 3D tomography from Figure 27 without ray coverage (top) and calculated total refraction static correction times (bottom).	53
Figure 38: Semblance velocity analysis applied to a CMP gather from Line 1. The left panel shows the semblance values for the CMP gather shown to the right. Semblance values are less than 0.1 and cannot be correlated to any event in the CMP gather.	54
Figure 39: Constant velocity panels for three velocities. Left: 6 km/s; center: 7 km/s; right: 8 km/s.	56
Figure 40: Slices from the 3D KPSDM applied using Line 1 data and various constant velocity models. The velocity (m/s) used for each panel is shown in the bottom right corner. Arrows depict consistent features that can be interpreted throughout the panels. The depth represents the depth of the velocity model used. The zero reference is at 700 m above sea level.	57
Figure 41: Slices from the 3D KPSDM applied using Line 1 data and various constant velocity models. The velocity (m/s) used for each panel is shown in the bottom right corner. Arrows depict consistent features that can be interpreted throughout the panels. The depth represents the depth of the velocity model used. The zero reference is at 700 m above sea level.	58
Figure 42: Conceptual models. Top: model considering a lens-like shaped peridotite body. Bottom: model considering an attached peridotite body to the IGB.	60
Figure 43: Conceptual models after smoothing window. Top: model considering a lens-like shaped peridotite body. Bottom: model considering an attached peridotite body to the IGB. The black-dashed squares mark the extent of the models that were cropped and used later for the 3D KPSDM.	61
Figure 44: Slices from the 3D KPSDM after migration of Line 1 using the detached (top) and attached (bottom) velocity models shown in Figure 43.	62
Figure 45: To the left, a slice from the 3D velocity model cropped from Ryberg et al. (2023). The Black-thick line represents the topography. To the right, the 3D KPSDM of lines 1, 2 and 3 using the cropped velocity model. Overlaid on the migrated image is Slice C from the three-dimensional inversion (see Figure 27).	63
Figure 46: a) Migrated image. b) Annotated migrated image. Image (b) is overlaid with the 2.5D tomography (see Figure 25(b)). The dashed-dotted line and dot mark the approximate	

position of the top of the IGB proposed by Scarponi et al. (2020) (with ± 1 km uncertainty). Yellow question marks are positioned in areas where further interpretation is not possible. Yellow lines: main faults F1 and F2. Blue lines: reflectors outside the area delimited by faults F1 and F2. Red lines: SW dipping faults. Orange lines: NE dipping faults. Green lines: sub-horizontal faults. Dark red lines: Inferred structures not directly imaged. The two yellow arrows numbered as 1 and 2 mark the position where the P-wave reflected refractions from Figure 36 were imaged. Arrow N° 1 represents PRR1. Arrow N° 2 represents PRR2. The position of this migrated cross-section is depicted by the red-dashed line labeled as M in Figure 49. 64

Figure 47: Interpreted perspective image of the migrated results, overlaid with the 2.5D tomography (see Figure 25(b)). The geological map from Quick et al. (2003) is presented as an aid to interpretation. Arrows mark evident correlation between features interpreted in the migrated image and those identified in the geological map. Shaded in violet is the extent of the peridotite body interpreted in this study. The dashed-dotted line and dot mark the approximate (± 1 km) position of the top of the IGB proposed by Scarponi et al. (2020). Yellow question marks are positioned in areas where further interpretation is not possible based on our results. Fault/fracture and reflector colors as in Figure 46. 65

Figure 48: Fence diagram of a small subset from the 3D migrated cube for the reflector depicted in Figure 35 (black arrow). The blue arrows mark the position of the reflector. It is located at Z= 1.3 km, Northeast of the survey area. The position of this fence diagram is depicted by the MR red-dashed line in Figure 49. 66

Figure 49: Map showing the position of the slice in Figure 46 as a red-dashed line labeled as M. The two red-dashed lines labeled as MR represent the position of the slices shown in the fence diagram of Figure 48. 67

Figure 50: Comparison between the two-dimensional tomographic results and the discontinuity density map by Menegoni et al. (2024). The map at the top right depicts the area analyzed to obtain the discontinuity density map with a yellow polygon. The center image shows a density map of discontinuities, yellow/orange colors representing high density values. This map represents the face of the outcrops analyzed; it is not a map view. The two-dimensional tomography is added as comparison to correlate the high density of discontinuities with the low velocity zone at the middle of the profile. Red squares with dashed-lines show the area that correlates the high values in the density map with the low velocity anomaly in the tomography. 72

Figure 51: Schematic picture depicting the formation of the different groups of faults. (1) & (2) Formation of Group 1. (3) Formation of Group 2. (4) Formation of Group 3. After Ueda et al. (2020). 72